FEDERAL UNIVERSITY OF MINAS GERAIS
Institute of Exact Science
Graduate Program in Physics

Raphaela de Oliveira Gonçalves

THE FUNDAMENTAL PROPERTIES OF PHYLLOSILICATES AND ITS HYDRATION AT THE NANOSCALE BY WATER CONFINEMENT

Belo Horizonte
2023

Raphaela de Oliveira Gonçalves

THE FUNDAMENTAL PROPERTIES OF PHYLLOSILICATES AND ITS HYDRATION AT THE NANOSCALE BY WATER CONFINEMENT

Thesis presented to the Graduate Program in Physics at the Institute of Exact Sciences of the Federal University of Minas Gerais as a partial requirement for obtaining the title of Doctor of Science.

Supervisor: Klaus Wilhelm Heinrich Krambrock
Co-supervisor: Angelo Malachias de Souza
Co-supervisor (sandwich): Ingrid David Barcelos

Belo Horizonte
2023

Dados Internacionais de Catalogação na Publicação (CIP)

G635f Gonçalves, Raphaela de Oliveira.
The fundamental properties of phyllosilicates and its hydration at the nanoscale by water confinement / Raphaela de Oliveira Gonçalves. – 2023.
114 f. : il.

Orientador: Klaus Wilhelm Heinrich Krambrock.
Coorientador: Ângelo Malachias de Souza.
Tese (doutorado) – Universidade Federal de Minas Gerais, Departamento de Física.
Bibliografia: f. 94-110.

1. Filossilicatos. 2. Água. 3. Nanomateriais. 4. Microscopia de varredura por sonda. I. Título. II. Krambrock, Klaus Wilhelm Heinrich. III. Souza, Ângelo Malachias de. IV. Universidade Federal de Minas Gerais, Departamento de Física.

CDU – 537.533.35 (043)

Ficha catalográfica elaborada por Romário Martins Ribeiro – CRB6 3595
Biblioteca Professor Manoel Lopes de Siqueira – Departamento de Física - UFMG

UNIVERSIDADE FEDERAL DE MINAS GERAIS
INSTITUTO DE CIÊNCIAS EXATAS
PROGRAMA DE PÓS-GRADUAÇÃO EM FÍSICA

ATA DE DEFESA DE TESE

ATA DA SESSÃO DE ARGUIÇÃO DA 422ª TESE DO PROGRAMA DE PÓS-GRADUAÇÃO EM FÍSICA, DEFENDIDA POR RAPHAELA DE OLIVEIRA GONÇALVES orientada pelo professor Klaus Wilhelm Heinrich Krambrock e coorientada pelo professor Ângelo Malachias de Souza, para obtenção do grau de **DOUTORA EM CIÊNCIAS, área de concentração física**. Às 14:00 horas de vinte e três de outubro de dois mil e vinte e três, reuniu-se a Comissão Examinadora, composta pelos professores **Klaus Wilhelm Heinrich Krambrock** (Orientador - Departamento de Física/UFMG), **Ângelo Malachias de Souza** (Coorientador - Departamento de Física/UFMG), **Hélio Chacham** (Departamento de Física/UFMG), **Ingrid David Barcelos** (Laboratório Nacional de Luz Síncrotron), **Bernardo Ruegger Almeida Neves** (Departamento de Física/UFMG), **Douglas Soares Galvão** (Instituto de Física Gleb Wataghin/UNICAMP) e **Marcelo Barbosa de Andrade** (Departamento de Física/UFOP) para dar cumprimento ao Artigo 37 do Regimento Geral da UFMG, submetendo a Mestre **RAPHAELA DE OLIVEIRA GONÇALVES** à arguição de seu trabalho de Tese de Doutorado, que recebeu o título de **"The fundamental properties of phyllosilicates and its hydration at the nanoscale by water confinement"**. A candidata fez uma exposição oral de seu trabalho durante aproximadamente 50 minutos. Após esta, os membros da comissão prosseguiram com a sua arguição, e apresentaram seus pareceres individuais sobre o trabalho, concluindo pela aprovação da candidata.

Belo Horizonte, 23 de outubro de 2023.

Prof. Klaus Wilhelm Heinrich Krambrock
Orientador da estudante
Departamento de Física/UFMG

Prof. Douglas Soares Galvão
Instituto de Física Gleb Wataghin/UNICAMP

Prof. Ângelo Malachias de Souza
Coorientador da estudante
Departamento de Física/UFMG

Prof. Marcelo Barbosa de Andrade
Departamento de Física/UFOP

Dra. Ingrid David Barcelos
Laboratório Nacional de Luz Síncrotron

Prof. Bernardo Ruegger Almeida Neves
Departamento de Física/UFMG

Prof. Hélio Chacham
Departamento de Física/UFMG

Candidata: Raphaela de Oliveira Gonçalves

Documento assinado eletronicamente por **Bernardo Ruegger Almeida Neves**, **Chefe de departamento**, em 24/10/2023, às 11:08, conforme horário oficial de Brasília, com fundamento no art. 5º do Decreto nº 10.543, de 13 de novembro de 2020.

Documento assinado eletronicamente por **Helio Chacham**, **Membro**, em 24/10/2023, às 14:53, conforme horário oficial de Brasília, com fundamento no art. 5º do Decreto nº 10.543, de 13 de novembro de 2020.

Documento assinado eletronicamente por **Marcelo Barbosa de Andrade**, **Usuário Externo**, em 24/10/2023, às 15:16, conforme horário oficial de Brasília, com fundamento no art. 5º do Decreto nº 10.543, de 13 de novembro de 2020.

Documento assinado eletronicamente por **Klaus Wilhelm Heinrich Krambrock**, **Professor do Magistério Superior**, em 24/10/2023, às 19:00, conforme horário oficial de Brasília, com fundamento no art. 5º do Decreto nº 10.543, de 13 de novembro de 2020.

Documento assinado eletronicamente por **Angelo Malachias de Souza**, **Membro de comissão**, em 24/10/2023, às 21:32, conforme horário oficial de Brasília, com fundamento no art. 5º do Decreto nº 10.543, de 13 de novembro de 2020.

Documento assinado eletronicamente por **Raphaela de Oliveira Gonçalves**, **Usuário Externo**, em 25/10/2023, às 08:40, conforme horário oficial de Brasília, com fundamento no art. 5º do Decreto nº 10.543, de 13 de novembro de 2020.

Documento assinado eletronicamente por **INGRID DAVID BARCELOS**, **Usuário Externo**, em 25/10/2023, às 19:13, conforme horário oficial de Brasília, com fundamento no art. 5º do Decreto nº 10.543, de 13 de novembro de 2020.

Documento assinado eletronicamente por **Douglas Soares Galvao**, **Usuário Externo**, em 06/11/2023, às 09:22, conforme horário oficial de Brasília, com fundamento no art. 5º do Decreto nº 10.543, de 13 de novembro de 2020.

A autenticidade deste documento pode ser conferida no site https://sei.ufmg.br/sei/controlador_externo.php?acao=documento_conferir&id_orgao_acesso_externo=0, informando o código verificador **2741149** e o código CRC **4432B5F1**.

To my father, who incited me to observe nature.
And Klaus, who taught me how to do it scientifically.

Acknowledgements

I thank art for giving meaning to my existence.

I thank my parents Dona Mirian and Seu Antônio for absolutely everything. I have no words to express my gratitude. It was yours countless efforts throughout my life that made this thesis a reality. I also thank my sister Nathália and Sérgio for believing in me. And thanks to all my family for their support.

My friends. From the oldest to the newest, from the long-lasting friendships to the casual ones. I am deeply grateful to all my friends for sharing their lives with me. If you have friends, you have everything. I love you. And thanks also to love for sublimely reinventing itself as my sweet friend after tough years.

I am also grateful to all my teachers over these many years of study. Your dedication made the difference in my life. I am glad that many have also become my friends. I especially thank Klaus, Angelo and Ingrid for their confidence in my work and for always encouraging me to push my limits. I am proud to have been guided by you and I hope to be able to unify every detail that I admire from each of you in my life as a scientist. I also thank Alisson, Raul and Chacham for having participated very closely in my Ph.D. Our discussions certainly contributed immensely to this thesis. I would like to thank Ingrid and Alisson, as well as Ana and her family, my friends, and my family for all their support in my installation in the city of Campinas during my sandwich Ph.D.

I thank all my collaborators for the hard work and scientific efforts that have improved me as a researcher and successfully resulted in the articles produced as a direct contribution of this thesis. This research was only possible thanks to the scientific facilities provided by the Federal University of Minas Gerais (UFMG), Federal University of Ouro Preto (UFOP), Federal University of Lavras (UFLA), Mackenzie Presbyterian University, Brazilian Center for Research in Energy and Materials (CNPEM), Advanced Light Source (ALS) and also Neaspec. In particular, I would like to acknowledge the Center of Microscopy and the assistance of Marcio Flores, LabCri and the assistance of Alexandre Moreira, Roberto Paniago for the Mössbauer spectroscopy analysis, Roberto Moreira for the assistance in micro-FTIR measurements, and the LCPNano facilities at UFMG. I thank Alisson Cadore for the measurements performed at Mackgraphe (Mackenzie). I would like to thank the facilities of the Laboratory of Microscopic Samples (LAM) - LNLS/CNPEM, Verônica Teixeira for the assistance at the CARNAUBA beamline in SIRIUS - LNLS/CNPEM, and Raul Freitas for the assistance at the IMBUIA beamline in SIRIUS - LNLS/CNPEM. At LNNano/CNPEM, I would like to thank the assistance of Carolina Torres for the Raman spectroscopy measurements, and Carlos Costa and Cleyton

Biffe for their assistance in the KPFM measurements. I also would like to thank Raul Freitas and Adrian Cernescu for their assistance at Neaspec. I thank the assistance of Hans Bechtel and Stephanie Corde at ALS. Finally, I thank Professor Marco Fonseca from UFOP for supplying the clinochlore and phlogopite crystals that were studied in this thesis. In addition, I would like to thank UFMG and the Physics Department at ICEx for being my home. I also thank CNPEM and Sirius for having welcomed me in the best possible way during my sandwich period. It is a pleasure to share my daily life with my co-workers and carry the name of both institutions.

I thank the direct financial support from the National Council for Scientific and Technological Development (CNPq) that who paid my Ph.D. scholarship. I also thank the additional financial support from the Coordination for the Improvement of Higher Education Personnel (CAPES), the Research Support Foundation of the State of Minas Gerais (FAPEMIG), the Research Support Foundation of the State of São Paulo (FAPESP) and the Brazilian Nanocarbon Institute of Science and Technology (INCT/Nanocarbono).

As my final message, trust science as the only way.

Science is art.

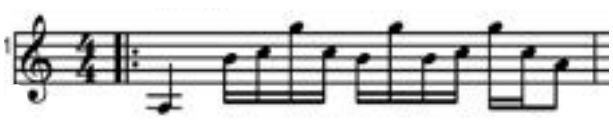

Flatlands as recorded by The Aristocrats and written by Bryan Beller.
a song about two feelings at once on an infinitely flat road.

Resumo

A água é a matriz da vida e seu confinamento em nanocavidades é um tema central desde a geofísica até a nanotribologia. Os minerais filossilicatos de estrutura em camadas atuam como nanocavidades naturais para a água devido à sua capacidade de se hidratarem ao confinar as moléculas de água no espaço interlamelar. Abundantes na Terra, a ocorrência de minerais filossilicatos em outros planetas é uma assinatura da presença de água. No entanto, a hidratação de filossilicatos na nanoescala não é um processo totalmente compreendido e varia entre os espécimes geológicos. Por outro lado, os minerais filossilicatos são isolantes de largo *bandgap* e baixo-custo associado que têm sido recentemente explorados na fabricação de nanodispositivos. Por serem de origem natural, é comum a presença de impurezas. Dessa forma, é crucial entender como as impurezas e a hidratação através do nanoconfinamento de água alteram as propriedades fundamentais dos filossilicatos em sua forma de poucas camadas visando aplicações bi-dimensionais (2D).

Explorando o clinocloro do grupo das cloritas e a flogopita do grupo das micas trioctaédricas, esta tese visa expandir o conhecimento das propriedades fundamentais e hidratação dos filossilicatos na forma de poucas camadas. Primeiramente, realizou-se uma caracterização experimental robusta da estrutura, morfologia e de defeitos e impurezas das amostras. Com isso, foi possível fornecer uma descrição completa da estrutura 2D do clinocloro e flogopita e suas propriedades fundamentais a partir da forma bulk. Para elucidar como variações na estrutura atômica desses espécimes pouco explorados de filossilicatos favorecem o geoconfinamento da água e suas propriedades, uma ampla análise do nanoconfinamento de água em ambos filossilicatos foi conduzida. Através de técnicas avançadas de varredura por nanossonda, foi possível obter as propriedades vibracionais dos filossilicatos na sua forma de poucas camadas e determinar que a água nanoconfinada altera as propriedades mecânicas e dielétricas dos minerais. Os resultados obtidos sugerem que a água confinada pode se condensar formando gelo à temperatura ambiente, sendo estável à variação de umidade relativa, mas instável ao aumento de temperatura. Como resultado único, demonstrou-se um método controlado de nanomanipulação mecânica da água interlamelar.

Notavelmente, esta tese abre portas para a multifuncionalização dos minerais filossilicatos em sua forma de poucas camadas visando aplicações nas fronteiras da nanotecnologia - desde catálise, microfluídica e conformação de biomoléculas até sensoriamento e fabricação de nanodispositivos optoeletrônicos.

Palavras-chave: filossilicatos, nanoconfinamento de água, microscopia de campo próximo, microscopia de varredura por sonda.

Abstract

Water is the matrix of life and its confinement in nanocavities is a central topic from geophysics to nanotribology. Phyllosilicate layered minerals are natural nanocavities for water due to their capacity to hydrate by confining water molecules in the interlamellar space. Abundant on Earth, the occurrence of phyllosilicate minerals on other planets is a signature of water presence. However, the hydration of phyllosilicates at nanoscale is not a fully understood process and depends on the geological specimens. On the other hand, phyllosilicate minerals are insulators with a large bandgap and associated low-cost that have been recently explored in the fabrication of nanodevices. Because they are of natural origin, the presence of impurities is common. Thus, it is crucial to understand how impurities and hydration by the nanoconfinement of water change the fundamental properties of phyllosilicates in their few-layer form for two-dimensional (2D) applications.

Exploring clinochlore from the chlorite group and phlogopite from the trioctahedral mica group, this thesis aims to expand the understanding of the fundamental properties and hydration of phyllosilicates in their few-layer form. First, a robust experimental characterization of the structure, morphology and defects and impurities of the samples was carried out. With this, it was possible to provide a complete description of the 2D structure of clinochlore and phlogopite and their fundamental properties from their bulk form. To elucidate how variations in the atomic structure of these barely explored specimens of phyllosilicates favor the geo-confinement of water and its properties, a deep analysis of the nanoconfinement of water in both phyllosilicates was conducted. Using advanced nanoprobe techniques, it was possible to obtain the vibrational properties of phyllosilicates in their few-layer form and to determine that nanoconfined water changes the mechanical and dielectric properties of the minerals. The results obtained suggest that the confined water can condense forming *ice-like* arrangements at room temperature, being stable to relative humidity variation, but unstable to temperature increase. As a unique result, a controlled method for mechanical nanomanipulation of interlamellar water was demonstrated.

Notably, this thesis opens doors to the multifunctionalization of phyllosilicate minerals in their few-layer form aiming applications at the frontiers of nanotechnology - from catalysis, microfluidics, and patterning of biomolecules to sensing, and fabrication of optoelectronic nanodevices.

Keywords: phyllosilicates, nanoconfinement of water, near-field microscopy, scanning probe microscopy.

List of Figures

Contents

1 Introduction

The development of novel applications based on nanotechnology depends on the interesting properties that materials present when they are reduced down to the atomic scale and combined. From agro-environment [10] to fabrication of nanodevices [11], passing through the delivery of drugs [12], several fields benefit from the advances in the synthesis of new nanomaterials and in the understanding of their properties. Nowadays, one of the frontiers of nanotechnology is the study of complex materials and the functionalization of well-established nanomaterials such as graphene [13] and gold nanoparticles [14]. Within this scope, we can highlight the fabrication of nanodevices by engineering complex structures based on lamellar materials (LMs) as a promising route to expand these frontiers.

In the broadest sense, there are several devices based on nanomaterials that can be designed depending on the application. With regard to information processing, developing electronic nanodevices with high performance and stability at competitive costs is fundamental to make nanoelectronics scalable. The fabrication of electronic nanodevices built from LMs embedded in van der Waals heterostructures (vdWHs) are complex structures that require good transistors as building blocks for processing and storing information [15]. The basic operation of transistors can be understood by the operation of a field effect transistor (FET), which consists of controlling the current that flows along a conductive channel when a voltage is applied between its terminals (source and drain) [15]. However, the performance of FETs strongly depends not only on the carrier mobility of the conductive channel, but mainly on the general properties of the insulating material used to electrically insulate the device, as well as on the channel-insulator interface quality. Graphene, first obtained from the exfoliation of graphite minerals [16], has been proved to be an immediate natural source of high quality two-dimensional (2D) material. With extremely high charge carrier mobility [17], graphene can be used as channel layer in the manufacture of electronic nanodevices. In addition to graphene, hexagonal boron nitride (hBN) [18] and transition metal dichalcogenides (TMDs) [19] are the most investigated 2D materials so far. The hBN is an insulator with bandgap energy of 5.9 eV that has been widely applied as high-purity substrate and suitable material for encapsulation in the fabrication of nanodevices [20]. The TMDs, with the general formula MX_2 where M indicates the transition metal and X the chalcogen, are a family of 2D semiconductors with bandgap energy within the visible region of the electromagnetic spectrum. Their bandgap energy is modulated according to the number of layers, undergoing a transition from an indirect bandgap in their multilayer form to a direct bandgap in their single layer form, which is interesting for optoelectronic applications [21].

Even though the search for LMs was triggered by obtaining graphene from the

exfoliation of a highly abundant natural mineral (graphite), it has mostly focused on synthetic materials over the years [22]. Synthetic materials can be produced in controlled environments, avoiding contamination by impurities, but some processes are complex and, consequently, expensive. Similarly, the engineering of complex materials based on LMs through synthetic routes can be beneficial in controlling specific properties that these materials will present. However, some routes can be non-trivial and may have a high-cost associated, which is the current challenge in using hBN as a 2D insulator. For this reason, a large-scale production of these materials can be difficult and the benefits arising from the related nanotechnologies will be distanced from society.

An alternative to reduce costs associated with the study of complex materials is to search for heterogeneous and hierarchical lamellar materials of geological origin with technologically interesting properties that can be found in abundance in the planetary crust. Fig. 1 depicts the abundance of O and Si in the Earth's crust mainly in the form of silicate mineral compounds. Within the group of silicate minerals, phyllosilicates are the most abundant minerals with lamellar structure. The challenge in using naturally occurring LMs for nanotechnology applications is related to the existence of impurities and defects in their crystalline structures, such as point defects (vacancies, substitutional or interstitial impurities) or extended defects (grain boundaries, stacking faults). The presence of defects and impurities strongly affects the optoelectronic responses of a material, making it mandatory an in-depth investigation to identify their eventual influence on a given property of the material. This will allow its proper manipulation through defect engineering and tailoring of the material for the various intended nanotechnological applications.

In the scope of nanodevices built from complex structures formed by LMs, recent research has been carried out on phyllosilicate minerals, which are wide band gap insulators that can be exfoliated down to monolayers (MLs) [22]. As a direct contribution of this thesis, the article entitled *"Phyllosilicates as earth-abundant layered materials for electronics and optoelectronics: Prospects and challenges in their ultrathin limit"* [23] was produced to provide insights into the application of few-layer (FL) phyllosilicates in the fabrication of nanodevices. Phyllosilicates come from metamorphic geological environments with hydrothermal alterations [24], presenting a lamellar structure based on Si-O tetrahedral layers intercalated by octahedral layers of bi and trivalent ions such as Mg or Al with O/OH at the vertices. Some specimens of phyllosilicates can be pillared by ions, such as micas, or further octahedral layers, such as chlorites. Phyllosilicate minerals are adaptive materials with the unique ability to absorb water [25]. A hydrated phyllosilicate is a complex system of geological origin and natural abundance that can be explored at the frontiers of nanotechnology [26, 27].

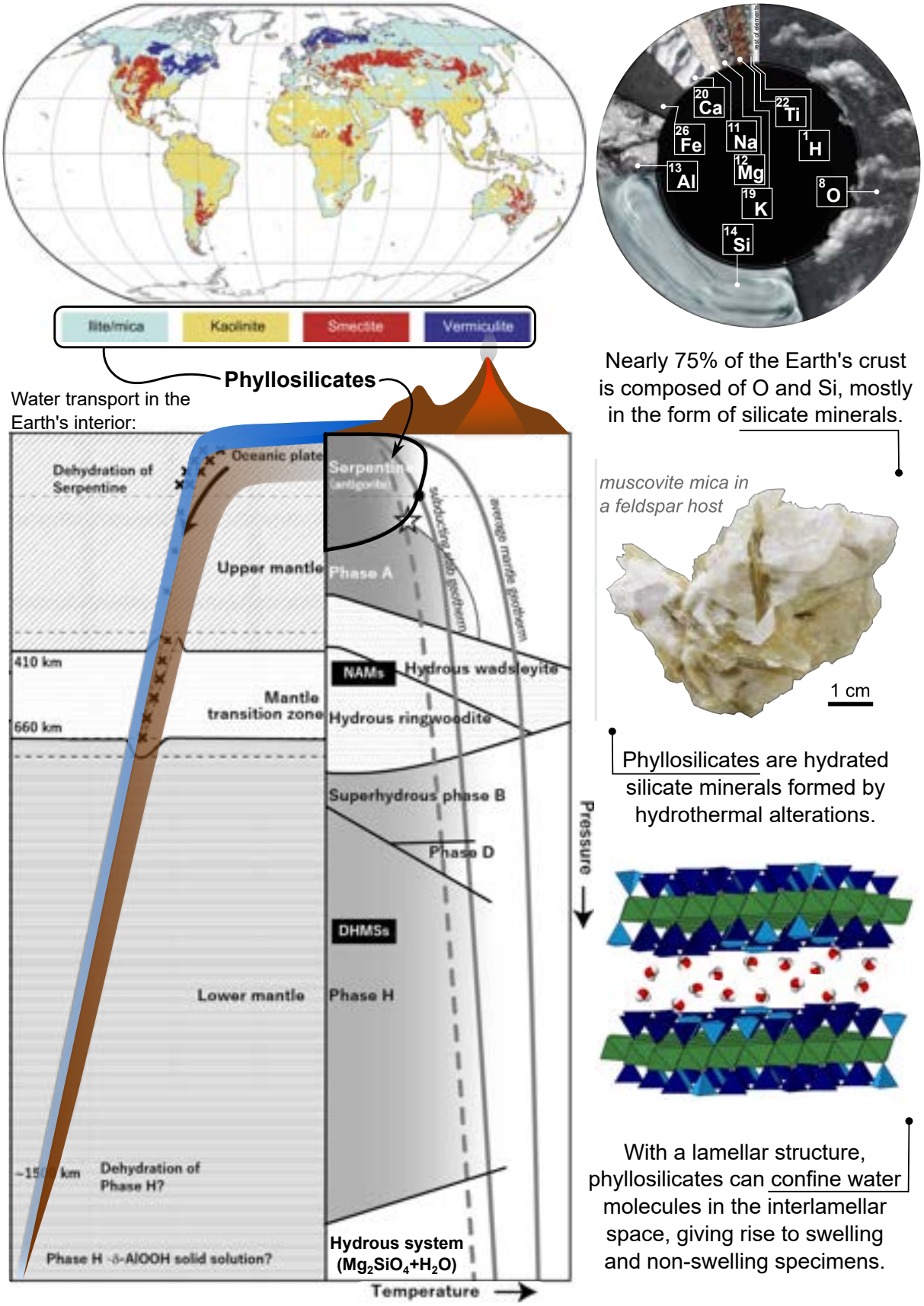

Figure 1 – Abundance of phyllosilicate minerals in the Earth's crust and their role in the water transport in the planetary interior.

At the top, a world-map of the most abundant phyllosilicate clay minerals in the Earth's crust adapted from the reference [28] is shown side by side with an info-graphic of the most abundant elements in the Earth's crust according to the WorldAtlas ©. Phyllosilicates are hydrated minerals that are fundamental in several geological processes, such as the water transport with the cycling of nutrients in the Earth's interior as shown on the left-side by the stability diagram of hydrous mineral phases (adapted from reference [29]). The cross symbols indicate the seismicity observed in the subducting oceanic plate. Below the point indicated by the star symbol, phyllosilicate hydrous minerals can transport water into the deeper part of the Earth's interior through its ability to confine water molecules in the interlamellar space of its layered structure (right side).

There are few studies exploring these minerals in their FL form in vdWH applications [30–34], but most of them dealing only with muscovite [31] and talc [32–34] specimens, barely exploring other minerals of this family, such as chlorites [35] and trioctahedral micas [30], and other applications related to their capillary capacity, such as microfluidic devices and sensors. Theoretical studies suggest that the electrostatic charge distribution due to the presence of substitutional ions in the structure of phyllosilicates modulates how water confines between its layers [36, 37]. Water confined in nanoscale media can form ordered layers commensurate with the molecular size with change in its elastic properties [38] and viscosity [39–41], presenting exquisite properties such as a low dielectric constant [42] and *ice-like* structures at ambient conditions [43–45]. Despite the lack of understanding of the physicochemical properties of water at the nanoscale, the nanoconfinement of water is a central topic in several fields.

In geophysics, hydrous minerals act as natural nanocavities for water transport on Earth that contributes to biochemical processes with cycling of nutrients and elements [46, 47], as illustrated in Fig. 1. Furthermore, geodynamical models require low yield strength materials to generate plate boundaries and phyllosilicate minerals correspond about a third of the fault rock volume [48]. These minerals can control variations of soil pH to favor the existence of microorganisms and other forms of life [24, 49] and their occurrence on other planets, such as Mars, is an indicator of water presence [50]. In phyllosilicates, the water molecules are oriented to form a strong hydrogen bond to the adjacent tetrahedral silicon oxide surface [51]. It is important to note that both the type of intercalated ion and the silicate structure can determine how water intercalates the material [52]. For example, phyllosilicate minerals with high negative surface charge due to atomic substitutions present hydration states of a few layers of water [52], varying the interlamellar spacing commensurately with the water layers. The ability to intercalate water in the lamellar stacking makes phyllosilicates a nano-porous material that can be building blocks in future nanotechnologies.

This thesis aims at understanding the role of impurities in determining the fundamental properties of two barely explored phyllosilicates and to elucidate how variations in

their atomic structures favor the geo-confinement of water during the mineral formation. Here, we provided a fully description of the 2D structure of clinochlore from the chlorite group and phlogopite from the trioctahedral mica group and their fundamental properties starting from their bulk form. We point out iron as the main impurity responsible for changing the fundamental properties of these minerals. We also performed a deep analysis of the nanoconfinement of water in phyllosilicates. The results demonstrated that interlamellar water changes the mechanical and dielectric properties of phyllosilicates with the possible formation of *ice-like* arrangements. A controlled way to change the phyllosilicate surface potential by nanomanipulation of interlamellar water is presented. Understanding the fundamental properties and hydration of phyllosilicates will allow the delineation of its capillary and surface properties for several nanotechnology applications. With this, we hope to demonstrate that clinochlore and phlogopite are promising abundant LMs with associated low-cost for applications not only in the fabrication of nanodevices, but also in catalysis, sensing, and patterning of bio-molecules in 2D systems. Furthermore, the information on the stability of nanoconfined water in phyllosilicate minerals provided by this thesis may help to explain fundamental geological processes.

This work, presented as a partial requirement for obtaining the title of Doctor of Science at the Federal University of Minas Gerais, is divided into six sections. The section 1 - Introduction presents the motivation of the work. Section 2 - Phyllosilicates presents the phyllosilicate minerals and the state-of-the-art concerning its applications in 2D technologies. The focus of this work will be on two barely investigated specimens of phyllosilicates, clinochlore and phlogopite. Then, the section 3 - Methods will describe the methodology developed to carry out the work, including sample preparation and a brief description of the applied experimental techniques. The results and discussions are presented in two sections. The section 4 - Sample Characterization is dedicated to structural, morphological, point defects and impurities characterization of clinochlore and phlogopite, as well as vibrational analysis. The section 5 - Nanoconfinement of Water in Phyllosilicates is dedicated to experiments investigating clinochlore and phlogopite hydration properties. Finally, the work is concluded in section 6- Conclusions with highlights of the main results of this thesis. A list of published articles produced as a direct contribution of this thesis is annexed at the end.

2 Phyllosilicates

Phyllosilicate minerals are wide-band gap insulators, stable in different environments, and abundant in nature. They are a broad family that includes clays, micas and chlorites [22]. They present a layered structure that enables their exfoliation down to MLs [22,53,54]. The variety of geological specimens of phyllosilicates arises from structural differences due to weathering and hydrothermal alterations [24]. Phyllosilicates on Earth can be igneous, metamorphic or sedimentary, originating from hydrothermal alterations, such that the whole family presents hydration by water or hydroxyl groups [55].

The basis of phyllosilicate atomic structure is the silicon oxide tetrahedral layer (T) that forms a hexagonal lattice with basal O shared by Si atoms in a ratio of 2 Si to 5 O [56]. The genealogy of phyllosilicate mineral structures is depicted in the diagram of Fig. 2. The layered general structure of phyllosilicate minerals is formed by stacking tetrahedral layers intercalated by octahedral layers (Oc). One unshared O per Si atom in the T layer points toward the Oc layer to form the octahedrons with OH groups at the remaining vertices. The Oc layers can be dioctahedral (*gibbsite-like*), with two octahedral sites to allocate trivalent ions, or trioctahedral (*brucite-like*), with three sites to allocate bivalent ions in a more compact arrangement [56]. A phyllosilicate ML can be formed by the combination of a T layer with an Oc layer in a T-Oc (1:1) or T-Oc-T (2:1) arrangement. Kaolinite and antigorite are standard specimens of 1:1 arrangement with dioctahedral and trioctahedral layers, respectively [57]. Phyllosilicates with 1:1 arrangement are more susceptible to polyhedral rotations and lattice distortions, which can form a *wave-like* crystalline structure, such as serpentines [57, 58]. Phyllosilicates with 2:1 arrangement present a compact structure with pyrophyllite and talc as standard specimens with di and trioctahedral layers, respectively [2, 26, 53]. Structural differences between phyllosilicate specimens occur due to the different atomic substitutions in both T and Oc layers [37]. To maintain the charge balance of the structure, these atomic substitutions favor the formation of a cationic interlayer or even a hydroxide interlayer [56]. Micas are phyllosilicates pillared by cations in the interlayer space, while chlorites are phyllosilicates with the further formation of an octahedral hydroxide layer intercalating the T-Oc-T stacking.

Early theoretical studies investigating the surface electrostatic potential of phyllosilicates consider each atom as a point charge [36, 37]. In this model, the talc structure corresponds to a charge-neutral layer of a trioctahedral 2:1 phyllosilicate from which we can derive a potential that decays rapidly with distance from the mineral surface. An atomic substitution is considered a defect from which a second potential of long-range interaction can be derived [37].

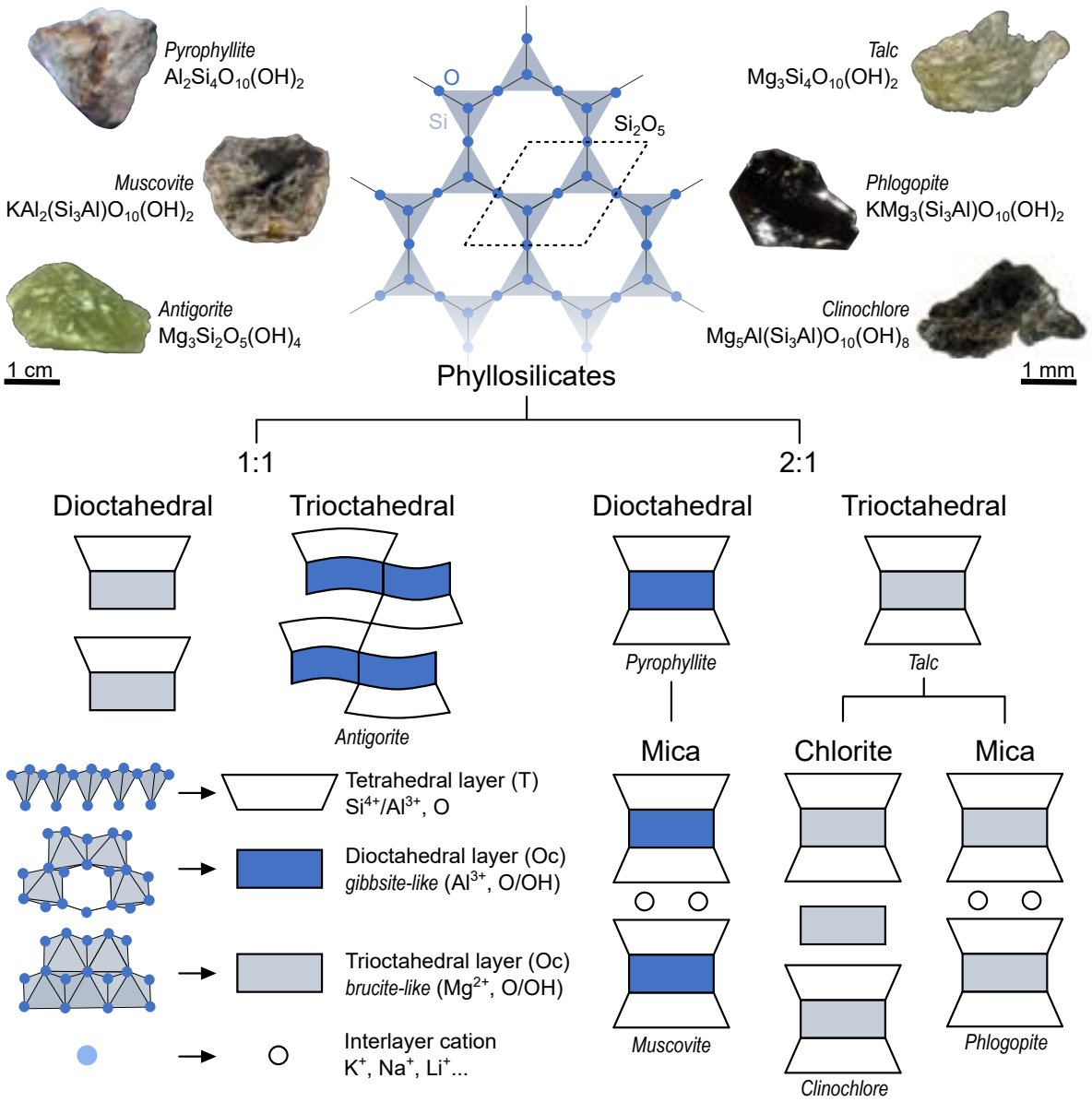

Figure 2 – Genealogical diagram of phyllosilicate mineral structures. The diagram starts by showing photographs of different specimens of phyllosilicates with a lamellar structure formed by a hexagonal lattice of Si-tetrahedrons with O at the vertices. Sequentially, phyllosilicate minerals can be divided into two classes according to the type of alternate stacking of tetrahedral and octahedral layers. The octahedral layers can accommodate metallic ions in two or three sites. Typically, the dioctahedral layer is formed by trivalent ions, such as Al^{3+}, in the central position of octahedrons with O/OH at the vertices, while the trioctahedral layer is formed by bivalent ions as central atoms, such as Mg^{2+}. The variety of specimens occurs by ionic substitutions in the atomic structure of standard specimens. Mica subgroup is a direct alteration of pyrophyllite-talc structure. In micas, interlayer cations emerge to balance the charge of the structure that is altered by ionic substitutions, such as one Al_{Si} substitution in the octahedral layer. Chlorite subgroup is the most complex structure of phyllosilicate minerals in which the 2:1 layer is intercalated by a hydroxide layer, typically a *brucite-like* layer. Figure adapted from reference [1]. The pyrophyllite image was taken from reference [2].

A Si^{4+} substitution by Al^{3+} in the T layer changes the electronegativity of the

substitutional site and localize the negative charge on the basal O of the T layer at the mineral surface, leading to stronger H-bonds of adsorbed H_2O molecules [37]. On the other hand, atomic substitutions in the Oc layer tend to localize the charge not on O atoms but on the Al^{3+} site, since Mg atomic orbitals have little tendency to interact with O orbitals to form chemical bonds [37]. Consequently, these theoretical studies suggest that the atomic substitutions modulate how water will intercalate the lamellar structure of phyllosilicates.

The hydration of phyllosilicate specimens implies an increase of unit cell volume for hydrated minerals commensurate with the number of water layers in the interlamellar space [52]. In this sense, phyllosilicates can be further divided by their capacity to swell or absorb water. The swelling properties of phyllosilicate minerals are related to the charge of its structure [59]. Neutral and high-charge structures lead to non-swelling specimens, while low-charge structures favor larger interlayer/interlamellar spaces. In micas, the interlayer cation controls the mineral hydration. The swelling potential of mica specimens is limited by the electrostatic interaction between interlayer cations and the tetrahedral sheets. The ionic substitution that occurs in the octahedral sheets, away from the interlayer space, result in larger expansion capacity due to low electrostatic interaction with the charge-balancing cations [59]. For this reason, one can have swelling and non-swelling members depending on the ionic substitutions that lead to a charged T-Oc-T layer.

Moreover, substitutional impurities that result in atomic-scale crystalline disorder are an intrinsic part of phyllosilicates. It is expected that impurities and defects can strongly affect the fundamental properties of any material, including phyllosilicates. Within this material class, we can identify iron impurities as the main point defect naturally present in those minerals [60]. As an abundant element in the geological formation environment of phyllosilicates [55], Fe can be present as a substitutional impurity in different sites, coordination, and valence states simultaneously. A less expressive amount of other substitutional impurities, such as Mn, Ti and Cr, has already been reported in the literature [30, 35, 61]. However, it has been shown that Fe plays a crucial role in determining the macroscopic properties of phyllosilicates, such as magnetism [3, 62], and bandgap energy reduction [30, 35, 63].

Iron impurities can be present as substitutional ions in the Fe^{3+} and Fe^{2+} oxidation states in four or six-coordination, the latter being the most common. Four-coordinated Fe ions can only occur for the Fe^{3+} oxidation state in those specimens that present a structural Al^{3+} substitution at one of the four four-coordinated Si^{4+} sites, such as micas [64]. The contribution of Fe^{2+} ions in phyllosilicates, however, is observed only in octahedral sites [64]. Fe^{3+} ($3d^5$) ions have a high-spin configuration with an effective electronic spin $S = 5/2$ and have been extensively investigated for several minerals [65, 66]. Six-coordinated Fe^{3+} ions are expected to occupy distorted octahedral sites by a strong rhombic crystalline

field [30, 35, 65, 66]. Six-coordinated Fe ions can occur for both Fe^{3+} and Fe^{2+} ions in an octahedral environment formed by four O and two OH ions. There are two possible configurations for the six-coordination Fe in phyllosilicates. In the *cis*-configuration, the two OH ions are adjacent, while in the *trans*-configuration the OH ions are on opposite vertices of the octahedron, divided by a plane formed by the four O atoms. The most probable sites for incorporation of iron as substitutional impurity in trioctahedral phyllosilicates are illustrated in Fig. 3. The nomenclature adopted in the literature for the octahedral sites is the letter M to indicate the six-coordination followed by the number 1, to indicate that it refers to a trioctahedral layer, or 2, to indicate that it refers to a dioctahedral layer in phyllosilicates. Next, the letters A and B indicate the less and more abundant sites with *trans* and *cis*-configuration, respectively.

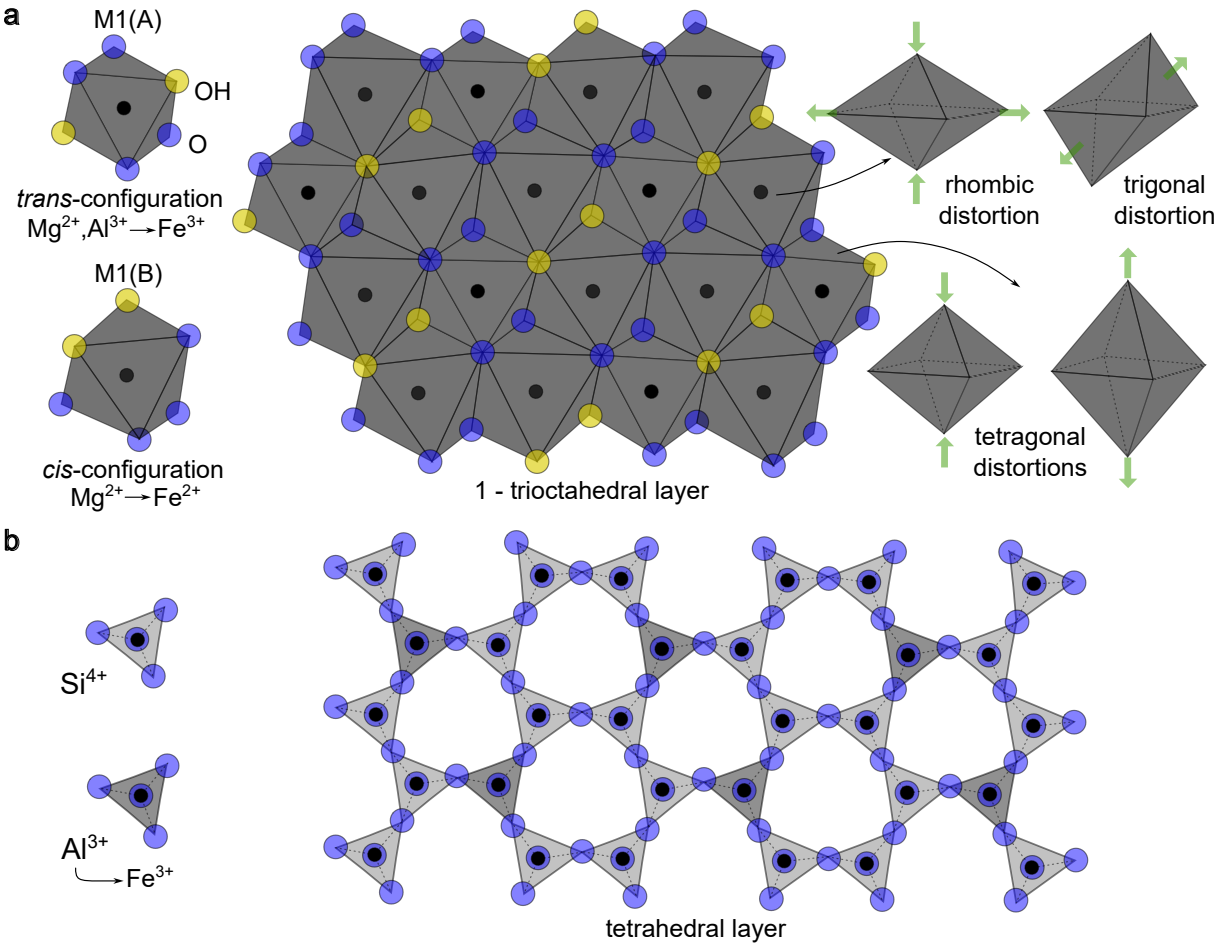

Figure 3 – Iron as the main substitutional impurity in phyllosilicate minerals. (a) The trioctahedral layers have two non-equivalent sites, M1(A) and M1(B), with an abundance of 1:2. Fe^{3+} ions are expected to occupy mainly M1(A) sites with tetragonal distortion, while Fe^{2+} ions are expected to occupy M1(B) sites with rhombic distortion produced by the strong crystalline field. However, mixed contributions can arise, for example from charge transfer processes between iron ions. (b) Phyllosilicates with Al_{Si} substitutions can also preferentially incorporate Fe^{3+} ions into the Al_{Si} site in the tetrahedral layer.

In T-Oc-T trioctahedral phyllosilicates, the Oc layer has three possible sites, two of which are equivalent. The non-equivalent sites are called M1(A) and M1(B). The M1(B)

site is the most abundant, in a 2:1 ratio with the M1(A) site. Furthermore, the M1(A) site is smaller than the M1(B) sites, exhibiting M1(A)-O atomic distances about 10% smaller than the M1(B)-O distances. Thus, ions with smaller ionic radius tend to occupy the M1(A) sites. This is the case of the structural occurrence of Al^{3+} in the Oc layer in some trioctahedral phyllosilicate specimens, such as chlorites, in which one of the three Mg^{2+} ions is replaced by one Al^{3+} in the M1(A) site [67, 68]. In trioctahedral phyllosilicates, the Oc layer is formed by a bivalent ion, such as Mg^{2+} ions, favoring the incorporation of Fe^{2+} impurities to maintain the charge balance of the structure. However, a mixed contribution of six-coordinated Fe^{3+} and Fe^{2+} impurities is possible in phyllosilicates due to the different arrangements of each octahedral site. In this sense, Fe^{2+} substitutional impurities are expected to occupy mostly M1(B) sites, while Fe^{3+} impurities occupy M1(A) sites. Mössbauer spectroscopy and optical absorption experiments [67,68] report the mutual presence of bi and trivalent six-coordinated Fe ions in trioctahedral phyllosilicates, resulting in a much greater incorporation of bivalent than trivalent iron ions due to the abundance of each site.

The magnetism that arises in phyllosilicates due to Fe impurities is highly dependent on the Fe concentration and the Fe^{3+}/Fe^{2+} ratio [3, 62]. The Oc layer is the main functional unit for magnetic ordering in naturally occurring Fe-rich phyllosilicates, such as minnesotaite, annite and biotite, which persists in the FL form [62]. Typically, phyllosilicates are paramagnetic at room temperature (see Fig. 4a) and can exhibit ferro or antiferromagnetic character below 40 K depending on the Fe^{2+} content [62, 69]. Reducing the total Fe content or increasing the Fe^{3+}/Fe^{2+} ratio results in a stronger disorder that eventually destroys the magnetic ordering. It has already been reported in the literature that the critical temperature of phyllosilicates increases with increasing Fe^{2+} fraction, but a small amount of Fe^{3+} ions can also contribute to increasing ferromagnetic interactions in phyllosilicates when it is surrounded by Fe^{2+} ions due to exchange interactions. This trend establishes a possible route to tune the critical temperature of phyllosilicates and increase it significantly for magnetic applications.

Regarding investigations in the FL form of phyllosilicates, most of the literature is concentrated on muscovite mica and talc, barely exploring other minerals of this family, such as chlorites and trioctahedral micas [22]. Talc, with the chemical formula $Mg_3Si_4O_{10}(OH)_2$, is formed by intercalating Oc layers of bivalent Mg central ion with T layers of Si as central atom, with O and/or OH at the vertices. With exfoliation down to a ML already reported in literature [53], talc has a direct bandgap energy of 5.2 eV and a higher dielectric constant than other materials such as hBN [53, 70]. Being the main representative specimen of phyllosilicates in 2D applications, talc has been used as a substrate and encapsulating material in the manufacture of nanodevices based on graphene [32, 71]. Muscovite, with the chemical formula $KAl_2(AlSi_3)O_{10}(OH)_2$, is formed by intercalating Oc layers of a central trivalent Al ion with T layers of Si as the central atom in which 25% of Al-substitutions

occur, with O and OH at the vertices. The replacement of Si^{4+} by Al^{3+} ions in the T layers results in a negative charge imbalance in the mineral structure that is compensated by the formation of a cationic interlayer of K^{+}. With exfoliation down to a ML also reported in the literature [31, 72], muscovite has a direct bandgap energy of 5.1 eV in its bulk form and a higher Young's modulus in its ML form compared to its bulk form [73]. Mica is widely used in 2D applications as an insulator in the manufacture of nanodevices based on graphene [31] and can be useful for designing memory devices [4] as shown in Fig. 4b.

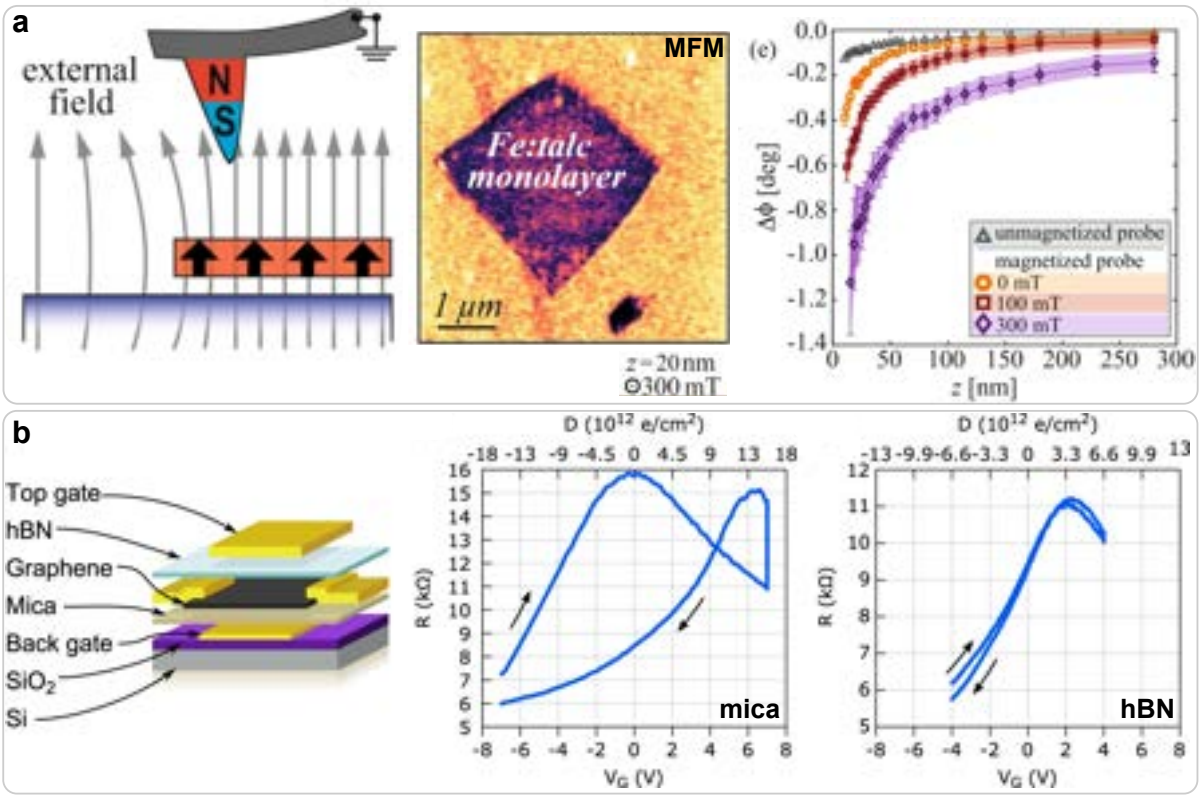

Figure 4 – Application of phyllosilicate minerals exploring their magnetic and insulating properties. (a) Room temperature paramagnetism of phyllosilicate minerals arises from Fe impurities and was probed for natural talc using magnetic force microscopy under application of external magnetic field [3]. (b) A strong hysteresis was found in a double-gated mica-graphene-hBN van der Waals heterostructure when mica was used as substrate/gate dielectric, which may be useful for designing memory devices [4].

It is important to keep in mind that phyllosilicates are hydrated minerals when applying them in 2D technologies. In particular for muscovite, its hydrophilic nature in combination with the hydrophobicity of graphene opened the possibility to study the electronic properties of water confined at the mica/graphene interface as shown in Fig. 5a [5, 74, 75]. However, few investigations have been carried out so far to understand how the hydration of phyllosilicates changes the overall properties of this 2D system and the mineral interactions with other LMs. Recently, a theoretical-experimental work investigating atomic-scale local hydration structures in clinochlore surface (from chlorite group) shows different ion adsorption behaviors on oppositely charged surfaces as shown in

Fig. 5b [6]. Regarding the water film formation on the surface of a cleaved mineral, another theoretical-experimental work shows that water films grow anisotropically driven by defects that capture water vapor at higher relative humidity (RH) environments (RH $>$ 30%) [76]. The literature also reports the construction of *ice-like* water layers at mica surface by AFM at room temperature [77] as depicted in Fig. 5c. Atomic substitutions in phyllosilicates also determine the arrangement of interlayer cations of pillared phyllosilicates such as micas [78]. In micas, the interlamellar water is expected to intercalate the cation interlayer and mediate the ionic diffusion in the highly confined space between the T-Oc-T stacking [79, 80].

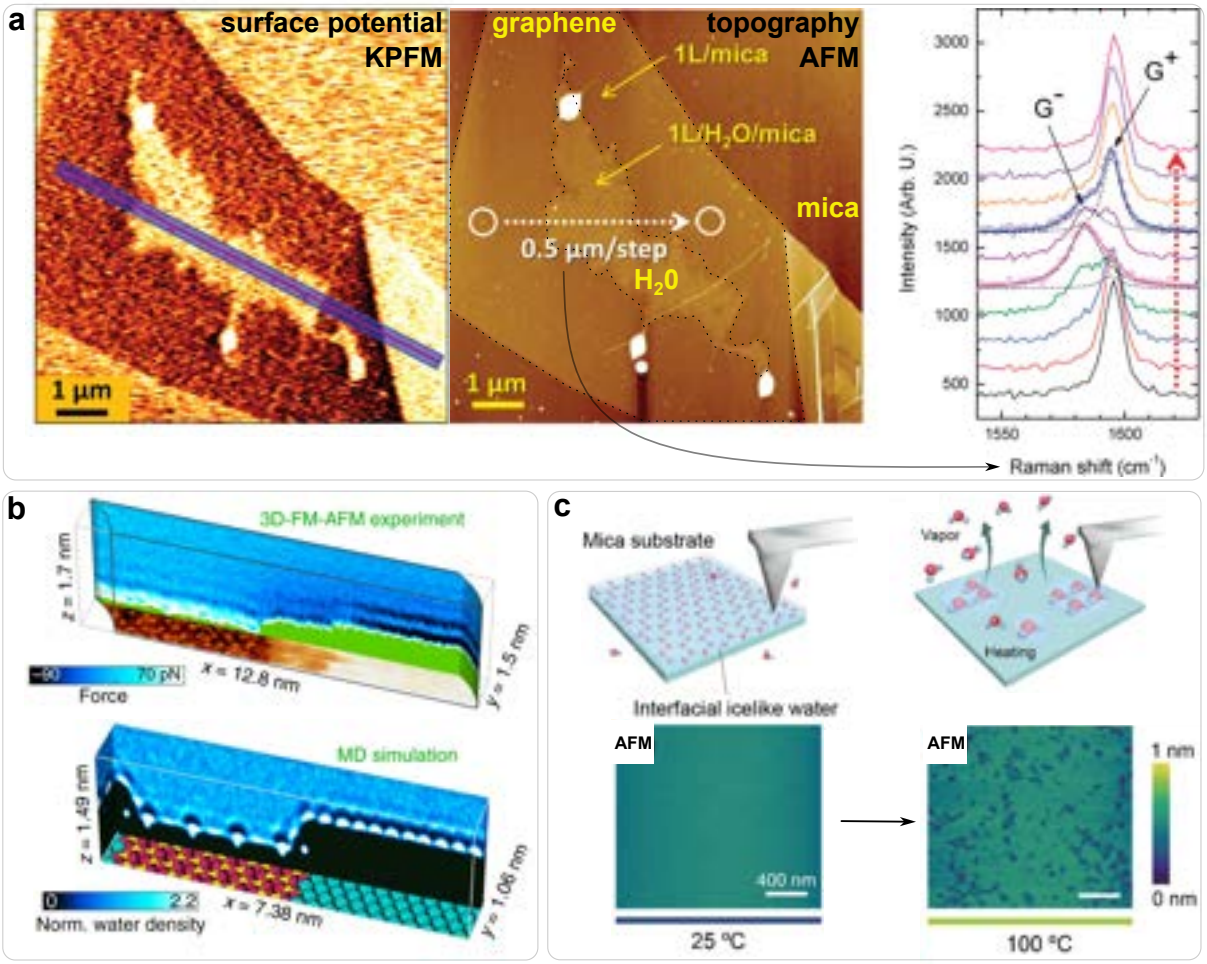

Figure 5 – Investigations on water adsorption on the surface of phyllosilicate minerals. (a) Molecular films of water in the interfacial region of graphene/mica heterostructures can change the electronic properties of the system. Using Raman spectroscopy to monitor variations in the graphene G band, it was observed that mica substrates induce strong p-type doping in graphene, while water films can effectively block this interfacial charge transfer [5]. (b) Ultra-low noise frequency-modulation atomic force microscopy was used to visualize the atomic-scale three-dimensional hydration structures on the surface of clinochlore in accordance with molecular dynamics simulations [6]. (c) Experimental construction of epitaxial *ice-like* water layer on mica hydrophilic surface at room temperature by using environment-controlled atomic force microscopy and the subsequent vaporization of the film by heating the substrate.

The present thesis, in particular, will focus on the characterization of two barely explored phyllosilicate minerals: clinochlore, from chlorite group, and phlogopite, from mica group. Both minerals were extracted from Minas Gerais/Brazil and sent to us as courtesy of Professor Marco A. Fonsenca from the Federal University of Ouro Preto (UFOP). The interest in studying the chlorite group lies in the complexity of its structure with several atomic alterations compared to talc, while phlogopite presents an atomic structure more similar to talc, but pillared by ions. The specifics of the crystalline structure of both minerals will be described in the subsections that follow.

2.1 Clinochlore

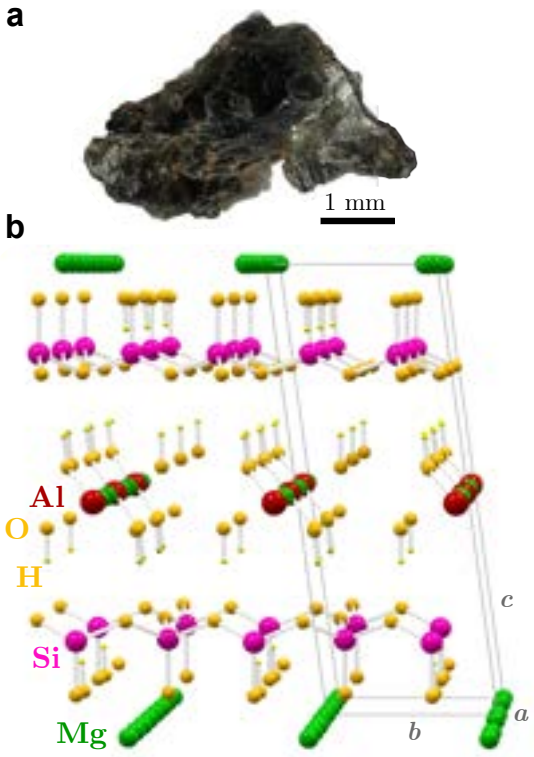

Figure 6 – The lamellar structure of clinochlore. (a) Photo of the clinochlore sample in its bulk form as extracted from nature. (b) Clinochlore lamellar structure composed of Si tetrahedral layers (pink spheres) with 25% of Al_{Si} substitution stacked along the c axis that are intercalated by Mg-octahedral layers (green spheres) and mixed octahedral layers of Mg and Al (red spheres). At the vertices, O and OH are represented by large and small yellow spheres, respectively. The gray lines delineate the clinochlore unit cell.

Clinochlore (Fig. 6a), with the chemical formula $Mg_5Al(AlSi_3)O_{10}(OH)_8$, emerges as one of the most naturally abundant phyllosilicates within the chlorite group. This mineral presents a large bandgap energy (over 3.6 eV [35]) and the most complex structure of the 2:1 phyllosilicates. The lamellar structure of clinochlore shown in Fig. 6b consists in a T silicon oxide layer, in which an Al atom occupies one of the four Si sites, intercalated with two types of Oc layers [81]. One of the two Oc layers consists of Mg^{2+} ions as central atoms and the other layer (*brucite-like* layer) is formed by both Al^{3+} and Mg^{2+} ions as central atoms of the octahedron with O and OH groups at the vertices. The charge balance of the structure is preserved by the presence of some trivalent cation impurities such as Cr and Fe [22] in octahedral sites. Such geometrical disposal provides the excess of positive charge needed to balance the negative charge due to Al substitution at Si sites and unshared O atoms in the formation of the T layer.

Different types of chlorite stacking occur in nature. The most abundant chlorite stacking is monoclinic with two distinct

Oc layes, and the other one is a triclinic T-Oc-T stacking with only one Oc layer [67]. Clinochlore is typically a monoclinic system, but its symmetry reduction from monoclinic to triclinic may occur by shifts between the layers along the stacking axis c [68]. The polymorphism of the group may result in geological specimens with combined characteristics of monoclinic and triclinic systems [68].

Iron is one of the most commonly identified impurity in the structure of phyllosilicates, as mentioned in section 2. In clinochlore, it was observed that Fe impurities occupy only octahedral sites [67,68]. In the *brucite-like* layer of clinochlore, there are three possible octahedral sites for occupation. Two of these sites are equivalent, such that the non-equivalent sites are called M1(A) and M1(B) with 1:2 abundance. The same distribution of sites occurs in the mixed Oc layer of clinochlore, which in its pristine form has a central Al^{3+} ion in the M1(A) octahedron and central Mg^{2+} ions in the M1(B) octahedrons with O and OH at the vertices in a *trans* and *cis*-configuration, respectively [67, 68]. Mössbauer spectroscopy experiments and optical absorption [67, 68] report the presence of bi and trivalent iron impurities in clinochlore, such that Fe^{2+} ions are considered the impurities occupying B-type sites and Fe^{3+} ions are the occupants of A-type sites, resulting in a higher incorporation of bivalent iron ions than the trivalent ones due to the abundance of the B-type site.

In addition to characterization studies, there are also several studies that technologically explore the optical, mechanical and electrical properties of clinochlore, mostly in its bulk form [81–83]. Its application has already been considered in several fields, such as prebiotic synthesis and polymerization of biomolecules [84], catalyst in chemical recycling of plastic waste [85] and decontamination of water resources [86]. However, its potential application in the fabrication of optoelectronic nanodevices still lacks investigation.

2.2 Phlogopite

Phlogopite is a mineral from the trioctahedral mica group with a lamellar structure formed by a C2/m monoclinic T-Oc-T stacking [56]. Two Si T layers with 25% of Al_{Si} substitution are intercalated by one trioctahedral layer of Mg^{2+} ions along the c axis in its pristine form [87]. The Si T layers are weakly bound together by the presence of K^+ cations between them. The K^+ cations are responsible to maintain the structure electrically neutral with respect to the negatively charged T layer due to Al_{Si} substitutions. The lamellar structure of phlogopite mica (Fig. 7) is a direct alteration of talc, such that its chemical formula is given by $KMg_3(AlSi_3)O_{10}(OH)_2$. Phlogopite is thermally stable and mainly used as an insulating material due to its high dielectric constant about 5-7, being also stable under gamma irradiation [88, 89].

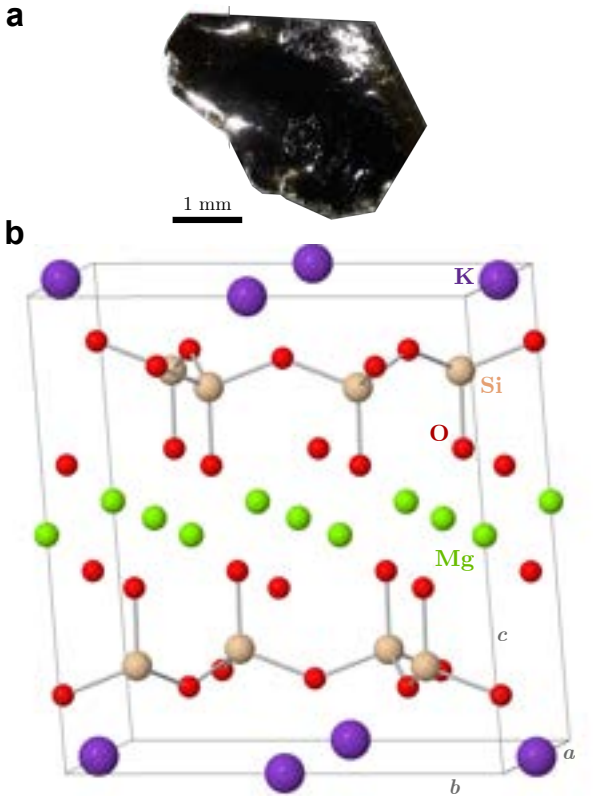

Figure 7 – The lamellar structure of phlogopite. (a) Photo of the phlogopite sample in its bulk form as extracted from nature. (b) Phlogopite lamellar structure composed of Si tetrahedral layers (pink spheres) with 25% of Al_{Si} substitution stacked along the c axis that are intercalated by Mg-octahedral layers (green spheres). At the vertices, O and OH are represented by the red spheres, respectively. The gray lines delineate the phlogopite unit cell.

Although several characterizations of micas have already been reported, little is discussed about the structural differences between dioctahedral micas, such as muscovite, and trioctahedral micas, such as phlogopite [90]. Phlogopite is a mica that allows less relaxation of lattice parameters compared to dioctahedral micas. This is due to its more compact crystalline structure with three octahedral sites instead of two, which favors less rotation of silicon tetrahedrons. The rotation of the tetrahedrons can also occur due to the breakage of the K^+ interlayer during exfoliation. Distortions in the mica lattice occur to compensate for the absence of K^+ cations that were responsible for providing the charge balance of the structure. Moreover, phlogopite micas are less susceptible to the breakage of this cationic layer [90].

As in clinochlore and other phyllosilicates, the incorporation of iron in the phlogopite crystal lattice is quite common. Starting from a pristine structure of phlogopite and allowing the successive isovalent incorporation of substitutional iron ions in the Mg^{2+} octahedral sites, the theoretical value calculated by hybrid functionals of its bandgap energy reduces from 7.86 eV to 3.50 eV [91]. Phlogopite has its effective value of bandgap energy reduced due to orbital hybridization. The interaction of O with Mg atoms is covalent in nature, but quite weak, while a very strong covalent bond is established between O and Fe atoms, favoring a strong hybridization of the 2p orbitals of O and 3d orbitals of Fe for the Fe_{Mg} substitutions. Furthermore, these substitutions lead to a slight expansion of the unit cell volume [91]. The incorporation of Fe^{3+} into phlogopite is observed to occur at four orthorhombic sites [92]. Three of the possible sites are octahedral, one M1(A) site and two M1(B) sites, characterized by four O and two OH ions in *trans* and *cis*-configurations, just like in clinochlore. However, in phlogopite an additional minor incorporation of Fe^{3+} is also observed in Al_{Si} tetrahedral sites [64]. The contribution of Fe^{2+} in phlogopite is observed

only in the octahedral sites [64].

Although the mica group has been extensively explored regarding its properties in FL form for several technologically interesting applications, most of the studies have been conducted only on muscovite dioctahedral micas, barely exploring other mica specimens, such as phlogopite. Its basic properties in FL form and its application in vdWHs together with other LMs lack of investigation [22].

3 Methods

The methodology of this work can be divided firstly into the characterization of the samples, whose results are presented in the section 4, and later in the investigation of nanoconfined water, whose results are presented in the section 5.

3.1 Methods for sample characterization

For the characterization of the samples, several experimental techniques were used with dedicated sample preparations. For the structural and morphological characterization, X-ray diffraction (XRD), energy and wavelength dispersion spectroscopy (EDS and WDS) were performed in bulk samples, along with optical microscopy (OM) and atomic force microscopy (AFM) for morphological characterization of the samples in their exfoliated form. The XRD experiments were acquired by Alexandre Moreira at LabCri - UFMG in a commercial Panalytical-Empyrean diffractometer using a Cu-K_α radiation source (λ = 1.5418 Å) in the Bragg–Brentano geometry ($\theta : 2\theta$). For acquiring the diffractogram, powders of clinochlore and phlogopite were prepared by milling part of the large crystals using a mortar. The qualitative elementary analysis by EDS were carried out in a Hitachi TM4000 Plus scanning electron microscope (SEM) previously calibrated with a copper standard sample at LCPNano - UFMG. Prior to analysis, the surfaces of the large crystals were mechanically exfoliated by the scotch-tape method. For the quantitative WDS analysis, the samples were prepared on resin support, polished and metalized with carbon at the Microscopy Center of UFMG. The data was acquired remotely with the technical support of Márcio Flores at different points in the samples using a previously calibrated JEOL 8900 electron microprobe. For the morphological characterization of the samples in their FL form, OM and AFM images of selected clinochlore and phlogopite flakes exfoliated onto (300 nm) SiO_2/Si substrates were acquired by Alisson Cadore at Mackgraphe - Mackenzie.

For the point defects and impurities characterization, electron paramagnetic resonance (EPR) measurements, Mössbauer spectroscopy and optical absorption in ultraviolet/visible/near-infrared (UV/Vis/NIR) spectral region were performed in bulk samples. X-ray fluorescence (XRF) and X-ray absorption near edge structure (XANES) measurements using synchrotron radiation were performed in clinochlore and phlogopite in their FL form. For the EPR measurements, a custom build commercial Magnettech MiniScope MS 400 X-band spectrometer coupled to water-cooled electromagnets capable of producing magnetic fields up to 800 mT was used. The EPR angular dependence at room temperature of a bulk clinochlore sample coupled to a goniometer was performed with c axis perpendicular to the rotating axis, in which the c axis was parallel to the applied

magnetic field for a specific orientation. The parameters used to acquire the spectra were 9.441(1) GHz for clinochlore and 9.440(1) for phlogopite, with approximately 30 mW of microwave power, 100 kHz and 0.5 mT of field modulation. The EPR signals are labeled by their effective g-factors defined by the resonance condition $h\nu = g\beta B$, where h is Planck's constant, ν is the microwave frequency, β is the Bohr magneton and B is the modulus of the applied magnetic field. The Mössbauer spectra of clinochlore and phlogopite powders prepared by milling in a mortar from the large crystals were measured by Roberto Paniago at UFMG in constant acceleration mode (triangular velocity) and using a ^{57}Co source in an Rh matrix at room temperature. The spectra were adjusted using the *software* Normos [93]. The optical absorption spectra were obtained in transmission and reflectance mode on a Shimadzu 3600 Plus UV/Vis/NIR spectrometer for bulk samples fixed to the sample holder by Alisson Cadore at Mackgraphe - Mackenzie. XRF fluorescence maps were acquired using a synchrotron beam size of 500 x 200 nm^2 in panoramic areas of 500 x 500 μm^2 with 5 μm/pixel for clinochlore under 9750 eV of excitation energy. For phlogopite, the XRF maps were acquired in areas of 250 x 250 μm^2 and 5 x 5 μm^2 with 5 μm/pixel and 50 nm/pixel, respectively, under 7200 eV of excitation energy. The hyperspectral maps were produced by normalization by the strongest signal pixel through Python codes for each impurity found in the samples. X-ray absorption near edge structure (XANES) measurements were performed around the Fe K-edge energy in fluorescence mode and room temperature also with nanometric beam size (down to 500 nm x 200 nm). For qualitative comparison, standard references in which Fe can be found in different oxidizing states were also measured (metallic Fe – Fe0, wüstite FeO – Fe^{2+}, hematite Fe_2O_3 – Fe^{3+} and magnetite Fe_3O_4 – mixed $Fe^{2+,3+}$). The XRF and XANES measurements were performed at CARNAUBA beamline in SIRIUS - LNLS/CNPEM with the technical and scientific support of Verônica C. Teixeira.

For the vibrational characterization, we performed Raman spectroscopy from bulk to FL samples and synchrotron infrared nanospectroscopy (SINS) in FL samples. All FL samples were prepared at the Laboratory of Microscopic Samples (LAM) in SIRIUS - LNLS/CNPEM using the standard scotch tape exfoliation method to release and transfer FL clinochlore and phlogopite flakes atop of (300 nm) SiO_2/Si and (100 nm) Au/Si substrates. The produced flakes were also pre-characterized by OM using a Nikon Eclipse LV100ND optical microscope. The Raman spectroscopy was performed using a HORIBA XploRA PLUS confocal Raman microscope with the technical support of Carolina Torres at LNNano/CNPEM. The clinochlore samples were excited with a 473 nm laser and the phlogopite samples with a 638 nm laser. The bulk samples were measured with a x50 magnification objective and the exfoliated ones with a x100 objective. Each spectrum corresponds to 20 accumulations with 10 s of integration. The SINS technique combines a scattering scanning near-field optical microscopy (s-SNOM) with an IR synchrotron radiation source. The SINS experiments were performed remotely at Beamline 2.4 in ALS

using a commercial s-SNOM instrument (Neaspec GmbH) with the technical support of Hans Bechtel and Stephanie Corder. All SINS spectra $S_n(\omega) = |S_n|exp(i\phi_n)$, where $|S_n|$ and ϕ_n were the SINS amplitude and phase, presented here were demodulated at the 2nd tip harmonic (n=2). The spectra were normalized by a reference spectrum acquired from a clean gold surface region of the substrate.

3.2 Methods for analysis of nanoconfined water

The investigation of water nanoconfinement in FL clinochlore and phlogopite, in particular in clinochlore, was carried out using Kelvin Probe Force Microscopy (KPFM) and IR s-SNOM techniques. A complementary analysis in bulk clinochlore was performed using standard Fourier-transform infrared spectroscopy (micro-FTIR).

All FL samples were prepared at LAM in SIRIUS - LNLS/CNPEM using the standard scotch tape exfoliation method to release and transfer FL flakes of clinochlore and phlogopite onto (300 nm) SiO_2/Si substrates. To study the stability of nanoconfined water, thermal treatments were also carried out at LAM in an ambient atmosphere using a Fisatom hot plate capable of reaching 360°C, as well as hydration processes using micropipettes for immersion of samples in droplets of distilled water and also a 5 mL beaker.

The KPFM experiments were performed at LNNano/CNPEM with the technical assistance of Carlos Costa and Cleyton Biffe using a ParkSystems NX-10 microscope equipped with an optical microscope with x10 magnification in a controlled atmosphere of N_2 that can reach 0.5% of relative humidity. Tips with a metallic coating of Pt-Ir (Nanosensors PPP-EFM-W, 45-115 kHz and 0.5-9.5 N/m) were used. The KPFM measurements were performed in tapping mode with 30 nm of free oscillation amplitude and 60% of setpoint, 5 V of amplitude and 17 kHz of frequency of the modulation electrical signal. The tip-sample system was grounded through a 1 MΩ resistor using silver ink to the electrical contacts. In order to perform a mechanical nanomanipulation of the interlamellar water, AFM scans in contact mode with different applied forces (1μ and 1.5 μN) were performed.

The IR s-SNOM measurements were performed partially at IMBUIA beamline at SIRIUS - LNLS/CNPEM and also at Neaspeac with the assistance of Raul Freitas and Adrian Cernescu using a commercial s-SNOM instrument (Neaspec GmbH). PtIr-coated AFM tips (typically 275 kHz) with an apex radius of about 25 nm were used with free oscillation amplitude of about 50-80 nm. The phase contrast nanoimaging was performed using a quantum cascade laser (QCL) and pseudoheterodyne detection system with demodulation at the 3rd tip harmonic.

For micro-FTIR measurements, a Nicolet Nexus 470 Fourier-transform spectrometer

equipped with a Centaurus microscope with x10 magnification was used at UFMG with the assistance of Roberto Moreira. The clinochlore spectrum were acquired under nitrogen purge using a non-polarized globar thermal light source of SiC, a KBr:Ge beamsplitter, a ZnSe sample holder and a MCT detector cooled with liquid N_2 by averaging 32 scans with 4 cm^{-1} of spectral resolution. For qualitative comparison, the IR absorption spectrum of liquid water was also acquired. The clinochlore sample was prepared by mechanical exfoliation with a thickness of 100 μm and a surface area of 3 x 3 mm^2.

Since KPFM and IR s-SNOM techniques were the main experimental tools used to investigate the nanoconfinement of water in this thesis, a detailed description of the working principle of each technique will be provided in the next subsections.

3.2.1 KPFM working principle

KPFM is an AFM-based technique. For this reason, we will start by discussing the fundamental aspects of AFM. The AFM-based techniques share the same principle of imaging a surface by sensing the interaction forces of a sharp nanoprobe that scans the sample. It is one of the most versatile tools of nanoscience, having a variety of operation modes with high spatial resolution that allows the observation (and even manipulation) of matter at the nanoscale.

The simplest potential capable of modeling interactions at the atomic/molecular level where van der Waals forces predominate is the Lennard-Jones potential: $U^{LJ}(z) = 4\epsilon[(\sigma/z)^{12} - (\sigma/z)^6]$, where ϵ denotes the depth of the attractive well, and σ the interparticle distance where the potential changes sign [94]. This model accurately describes a pair potential that balances an attractive dipole-dipole interaction term that is more significant for large z distances with another repulsive interaction term that prevails at shorter distances due to overlap of the atomic/molecular electron clouds. Thus, the AFM tip-sample interaction depending on the distance z between them can be described in a general way by the Lennard-Jones potential. However, the Lennard-Jones potential is not always sufficient to describe the tip-sample interaction. Under ambient conditions, for example, capillary condensation of water occurs in the form of a meniscus between the tip and the sample surface. In cases like this, when elastic interactions, adhesion and capillary forces between the tip and the sample must be considered, modifications in the Lennard-Jones potential are necessary for an adequate description of the system. Nevertheless, ideal measurement conditions, such as low relative humidity, can be achieved by performing AFM in a controlled environment in which the Lennard-Jones potential is sufficient to describe the tip-sample interaction. Based on this potential, three basic modes of operation for AFM measurements can be defined depending on the interaction regime as depicted in Fig. 8. In contact mode, the scan is made with the tip in physical contact with the sample surface and the forces felt are mostly repulsive. The scan in contact mode is done

statically, following the topography of the sample by keeping the interaction force constant. In non-contact mode the working distance is on the order of a few nanometers and the main interactions are attractive van der Waals forces. In this mode, scanning can be done dynamically with the tip being forced to oscillate freely above the sample in one of its vibrational modes. The intermittent contact (or tapping) mode is a compromise between contact and non-contact mode where the scan is dynamically performed but the tip touches periodically the sample surface. In this mode, there is a balance between spatial resolution and tip wear.

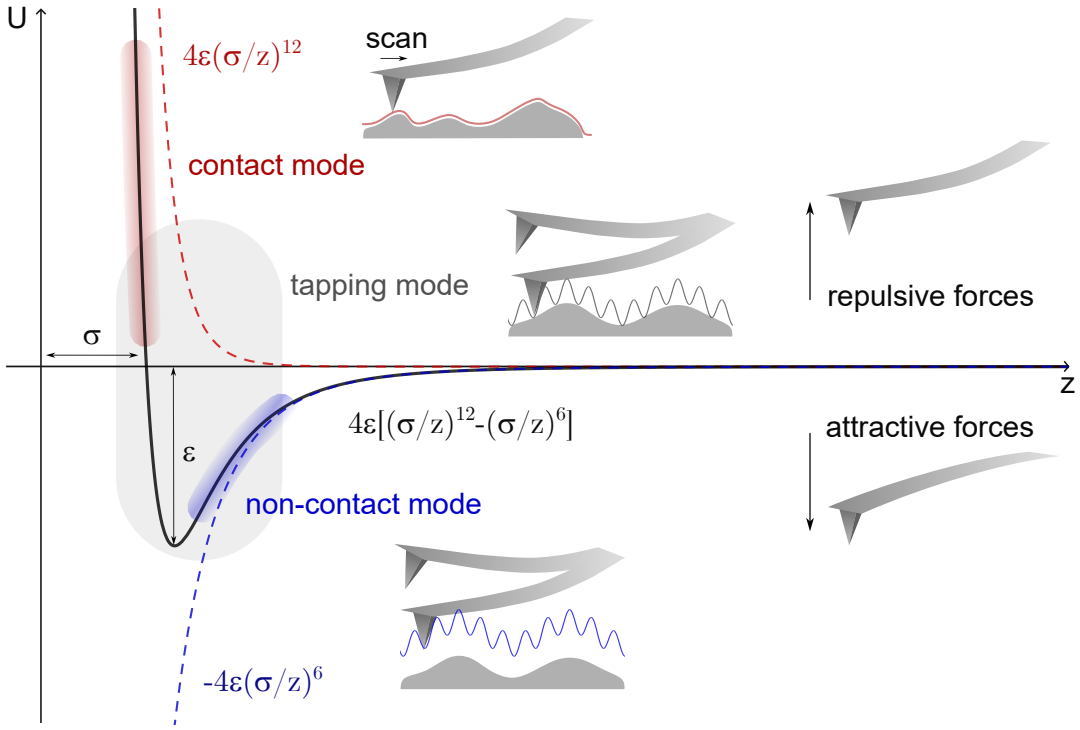

Figure 8 – AFM operation modes based on the Lennard-Jones potential. The simplest potential that describe the tip-sample interaction in an AFM measurement is the Lennard-Jones potential (black curve): $U^{LJ}(z) = 4\epsilon[(\sigma/z)^{12} - (\sigma/z)^6]$, where ϵ denotes the depth of the attractive well, and σ the interparticle distance where the potential changes sign. The red dashed curve is the repulsive term of the potential at which the AFM in contact mode is performed. The blue dashed curve is the attractive term of the potential at which AFM in non-contact mode is performed. The gray region corresponds to the interaction regime typically involved in AFM in tapping mode, which is performed dynamically.

The AFM tip is at the end of a cantilever with spring constant k that deflects a vertical distance x from its equilibrium position depending on the tip-sample interaction forces. This deflection can be described by Hooke's law: $F = -kx$ [95]. In this way, the dynamic modes of the AFM, in which the cantilever is set to oscillate freely, can be adequately modeled by a one-dimensional simple harmonic oscillator [95]. Weak disturbances to the oscillatory motion will result in a shift of the resonance curve without changing its shape. Thus, when the tip approaches the sample, there is a perturbation in the system that results in a shift $\Delta\omega$ of the resonant frequency $\omega = \sqrt{k/m}$ proportional

to the interaction, where m is the cantilever effective mass. The topographic profile of a sample surface by AFM in intermittent contact mode is obtained by correcting the vertical position of the tip to maintain the cantilever oscillation amplitude constant, minimizing further displacements of the resonant frequency according to the tip-sample interaction during the scan.

However, the acquisition of topography images by AFM in conventional modes of operation is susceptible to electrostatically induced artifacts [95]. Electrostatic forces generated by contact potential differences, localized charges, or externally applied potentials can contribute to the overall perceived tip-sample interaction in addition to the typical van der Waals forces. This results in artifacts in the acquired data that lead to false topography information. One way to minimize the electrostatically induced topographical errors is through the simultaneous acquisition of the surface potential and topography of the sample in a single scan, such that the electrostatic interactions between the tip and the sample are always minimized during the scanning by the application of a correction electric potential [95, 96]. This technique is known as single-scan Kelvin Probe Force Microscopy, abbreviated here as KPFM.

The surface potential of a conducting crystal corresponds to the work function $\Delta\Phi$ of the material. The work function of a material is associated with the energy difference between a free electron in vacuum and the most weakly bound electron in the solid [95]. When two conducting materials with different work functions (for example, a metal-coated tip and a gold film) are placed in contact, there is a diffusion of charges from the material with a lower work function to the material with a higher work function until the Fermi levels of the materials align. When the system reaches equilibrium, the material with the lower work function will present a relative more positive potential and the material with the higher work function will present a relative more negative potential [95]. Thus, there is a contact potential difference (CPD) between the tip and the sample that is proportional to the difference in work function between the materials. In a KPFM measurement, the electrostatic interactions are always minimized by applying a continuous electric potential of correction V_{DC} of the same magnitude as the CPD. The magnitude of the potential that needs to be applied to correct the CPD corresponds to the surface potential of the sample relative to the tip. Thus, the KPFM surface potential contrast is not absolutely quantitative but a relative measurement, unless the work function of the tip is well calibrated. In general, the tip and sample need to share the same ground in a KPFM measurement, being in electrical contact. It is also ideal for the tip to have a metallic coating to increase sensitivity to electrostatic forces.

If the sample is a wide bandgap insulator, which is the case for phyllosilicate minerals, the best description of a KPFM measurement however is to consider a capacitor. The tip and the back-electrode (the grounded substrate) are the plates of the capacitor in

which the sample is the dielectric, described by its dielectric constant [97, 98]. When two plates of a capacitor composed of different materials are electrically wired, charge diffusion occurs so that opposite charges accumulate on the capacitor plates. This accumulation of charges will result in a CPD analogous to the one described above. We can assume that the geometry of the capacitor plates (the tip and back-electrode) does not change along the sample. Thus, the surface potential probed by the KPFM measurement, which corresponds to the CPD, will depend only on the variations in the capacitance of the system, which in turn correspond to local differences in dielectric permittivity along the sample.

To access the dielectric information of the sample, we can probe the capacitive response of the system by applying a bias potential V_{DC} between the tip and the sample that is electrically modulated by an additional sinusoidal signal V_{AC} of frequency ω', analogously to AFM dynamic modes [95]. This sinusoidal electrical modulation allows the system to be also modeled as a one-dimensional simple harmonic oscillator. Thus, a change in the modulation frequency will be associated with local electrical perturbations induced by differences in the dielectric permittivity of the sample. To minimize this perturbation, we apply the continuous bias potential V_{DC} that cancels the local CPD, from which we can extract the relative surface potential of the sample [95]. The electric potential energy U_{el} stored in the tip/sample/back-electrode capacitor under a potential difference V is [95]

$$U_{el} = \frac{1}{2}CV^2, \tag{3.1}$$

so that the electric force $\vec{F_{el}}$ per unit charge e between the capacitor plates is given by

$$\vec{F_{el}} = -\nabla U_{el}. \tag{3.2}$$

However, a single-scan KPFM is a double-modulation technique in which the cantilever deflection is monitored. This deflection is proportional to the total force probed by the tip, which carries both topographic and electrical information through mechanical and electrical modulations, respectively. Since the tip is touching the sample surface sinusoidally through a mechanical modulation near its resonant frequency in tapping mode, the local capacitance C of the system will be dependent on the tip-sample distance z. We can restrict the analysis to the vertical direction only, so that

$$-\frac{dU_{el}}{dz} = -\frac{1}{2}\frac{dC}{dz}V^2. \tag{3.3}$$

Regarding the electrical modulation, the potential difference V across the capacitor corresponds to the superposition of the continuous bias electrical potential V_{DC} with the sinusoidal modulation $V_{AC}\sin(\omega' t)$, discounting the CPD [95]. Thus, we have $V = [V_{DC} + V_{AC}\sin(\omega' t)] - CPD$. Inserting this expression in Eq. 3.3, we will obtain that [95]

$$F_{el} = F_{dc} + F_{\omega'} + F_{2\omega'}, \tag{3.4}$$

where

$$F_{dc} = -\frac{1}{2}\frac{dC}{dz}\left[(V_{DC} - \Delta\Phi)^2 + \frac{1}{2}{V_{AC}}^2\right] \tag{3.5}$$

$$F_{\omega'} = -\frac{dC}{dz}(V_{DC} - \Delta\Phi)V_{AC}\sin(\omega' t) \tag{3.6}$$

$$F_{2\omega'} = \frac{1}{4}\frac{dC}{dz}{V_{AC}}^2\cos(2\omega' t), \tag{3.7}$$

where F_{dc} is the continuous component of the electric force, $F_{\omega'}$ the first harmonic component and $F_{2\omega'}$ the second harmonic component.

The first harmonic component $F_{\omega'}$ of the electrical force is the component of interest in KPFM measurements. By simultaneously minimizing $\Delta\omega$ and $\Delta\omega'$, both the topography and surface potential images can be obtained in a single-scan KPFM. This condition is reached when the applied bias potential nullifies the CPD, so $V_{DC} = CPD$. By demodulating the cantilever deflection signal at frequency ω', we can access the first harmonic component of the electrical force. Once this is done, we can monitor the condition when $V_{DC} = CPD$ to image the surface potential of the sample. In some experimental setups, the continuous and second harmonic components can be used as an extra correction feedback to increase the KPFM sensitivity [95].

The instrumentation required to perform a single-scan KPFM measurement is depicted in Fig. 9. The measurement is performed in tapping mode, so the cantilever is mechanically excited in a frequency ω in the order of 60-80 kHz by a piezoelectric actuator. The oscillator A is responsible to generate the reference signal for the piezoelectric actuator and for lock-in amplifier A, which is responsible for correcting $\Delta\omega$. The oscillator B generates the sinusoidal electrical signal V_{AC} at a typical frequency $\omega' = 17$ kHz that will be applied between the tip and the grounded substrate. This electrical sinusoidal signal will also be used as a reference for lock-in amplifier B, which is responsible for correcting $\Delta\omega'$. Lock-in amplifier corrections are made by comparing the reference signals with the cantilever deflection signal monitored by a photodetector. A laser is directed at the back of the cantilever and its motion-dependent reflection is directed to the photodetector. Thus, the signal resulting from the tip deflection, which is proportional to the tip-sample interaction, is mechanically and electrically modulated. This signal passes through frequency filters to separate the mechanical and electrical components before entering the lock-in amplifiers. In a homodyne detection, the output signal of the lock-in amplifier corresponds to a second harmonic component that is filtered and a continuous component. This continuous component is proportional to the phase difference between the reference signal and the input signal, carrying information about the tip-sample interaction. The output signals of the lock-in amplifier A and B are used in the feedback control loops to correct both the tip-to-sample distance z and the applied electrical bias potential V_{DC} in order to minimize the tip-sample interaction. Therefore, it is the correction signals produced by the lock-in amplifiers that will result in the topography and surface potential

images of the analyzed area during a single-scan KPFM. It is worth mentioning that the spatial resolution and potential sensitivity of KPFM measurements can be improved using sideband demodulations [99]. In the frequency spectrum of the cantilever deflection, sidebands appear at $\omega \pm \omega'$ caused by the oscillating force gradient with the application of V_{AC}. In this configuration, a heterodyne detection is implemented and the benefit is related to the fact that the electrostatic force gradient is mainly affected by the apex of the AFM tip, reducing the contribution of the cantilever [99]. Furthermore, it is also important that the KPFM measurements are carried out in extremely low humidity environments to avoid electrostatic interactions of ions and molecules adsorbed on the surface of the material. This guarantees the correct topography and surface potential imaging of the sample [95].

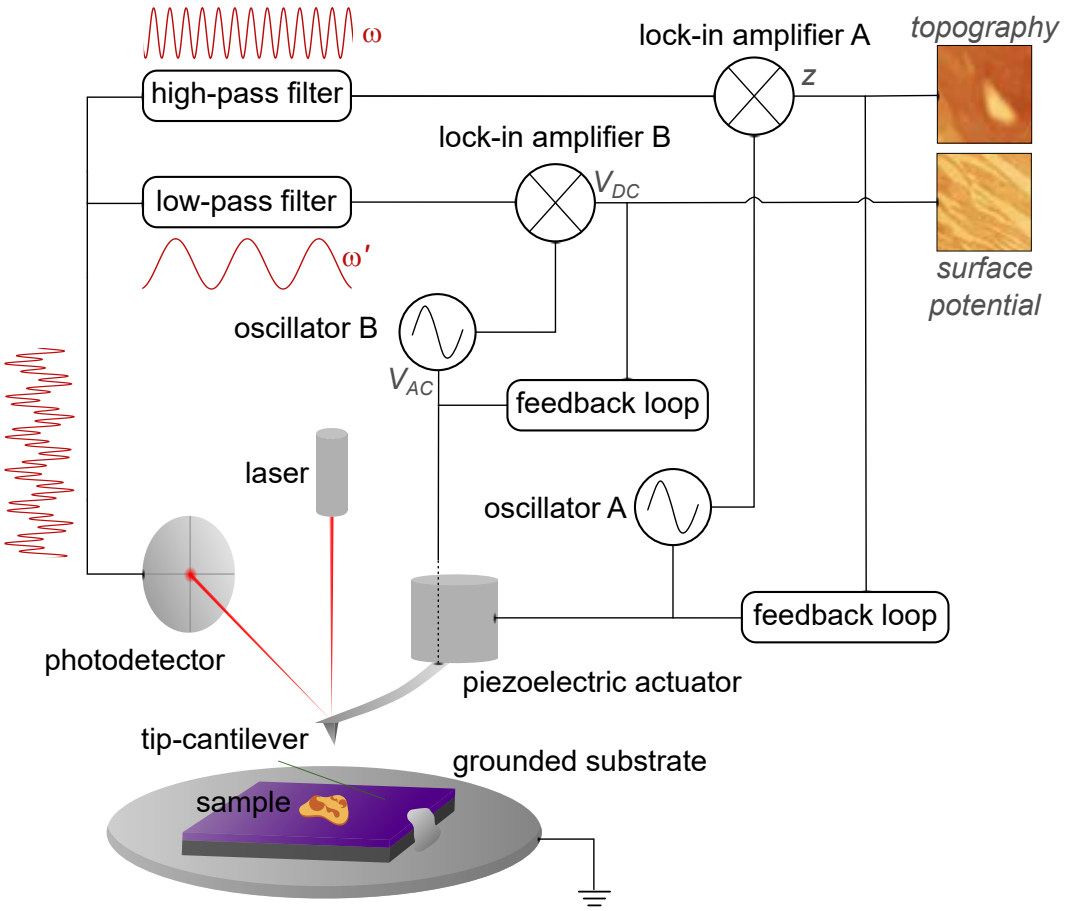

Figure 9 – Experimental diagram of the single-scan KPFM technique. The technique operates in double-modulation configuration in which the cantilever is mechanically and electrically modulated by the oscillators A and B, respectively. A photodetector monitors the cantilever deflection, which is filtered and demodulated by two lock-in amplifiers. The lock-in amplifiers A and B are responsible to minimize the mechanical and electrical frequency shift according to the tip-sample interaction, respectively, in a feedback control loop. Thus, the single-scan KPFM allows to image the topography and surface potential of a sample simultaneously.

3.2.2 s-SNOM working principle

The work entitled *"Review on infrared nanospectroscopy of natural 2D phyllosilicates"* [1] was produced as a direct contribution of this thesis. It provides an overview of the use of IR s-SNOM and SINS in the study of nano-optics and local chemistry of phyllosilicates in their FL form. In this section, we will focus on presenting the working principle of the IR s-SNOM that allowed us to confirm the presence of water in clinochlore at the nanoscale through chemical contrast nanoimaging. Like KPFM, IR s-SNOM is also an AFM-based technique but combines FTIR to perform imaging and spectroscopy. The general aspects of the AFM technique were described in the previous section. Thus, the description of the IR s-SNOM technique will begin with the presentation of general aspects of standard micro-FTIR spectroscopy.

The IR spectroscopy is a well-established technique that allows non-destructive chemical identification of a variety of samples [100]. This is possible because the technique accesses vibrational transitions of molecules and materials through electrical dipole interactions with light, which normally requires photons with energies in the IR spectral range [100]. When light hits a material, it can be transmitted, absorbed or scattered and reflected. Regarding light-matter interaction at macroscale, a material can be described by its complex refractive index N that depends of the radiation wavelength λ. The complex refractive index is defined as $N(\lambda) = n(\lambda) + i\kappa(\lambda)$, where n and κ are the real and imaginary part of the index that are related to light scattering and absorption, respectively [100]. N, n and κ are quantities that can be extracted from the complex dielectric permittivity function of the material $\epsilon(\lambda) = N(\lambda)^2$. The real part of dielectric permittivity function $Re[\epsilon] = n^2 - \kappa^2$ is related to the reflectivity of the material, and the imaginary part $Im[\epsilon] = 2n\kappa$ is related to its absorption properties [100].

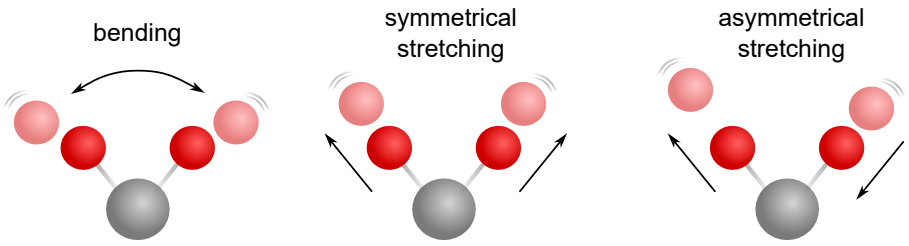

Figure 10 – Illustration of molecular vibrational modes. For a non-linear molecule composed of $N = 3$ atoms (red-type and gray-type) like water H_2O, there are $3N - 6$ vibrational modes: bending, symmetrical, and asymmetrical stretching.

The absorption of IR radiation by the material can be understood at the molecular level by considering a sample as a collection of point masses (atoms) held together by weightless springs (bonds). This spring–mass system has its vibrational normal modes that correspond to different discrete energy levels. An IR photon will be absorbed by the material if its energy matches the energy difference of two vibrational energy levels of the spring–mass system that describes the material. A vibrational mode will be active

in IR only if the dipole moment of the material, modulated by this specific vibrational mode, changes with the oscillation (at the same frequency) of a non-orthogonal electric vector of IR radiation [100]. An illustration of molecular vibrational normal modes such as bending and stretching can be seen in Fig. 10. In this sense, the IR absorption frequencies of materials and molecules are their fingerprints for chemical identification.

The IR absorption of a material can be obtained simply by passing an IR radiation beam through it and comparing the intensity of the radiation before and just after the sample. However, many vibrational modes can be active in the IR spectral region, including contributions from the ambient atmosphere. This makes the analysis of IR absorption spectra quite complex in practice. Thus, it is interesting to use a more robust instrumentation in order to properly obtain the absorption spectrum of the sample under analysis. The most commonly used technique to obtain IR absorption spectra of materials in the far-field regime is micro-FTIR.

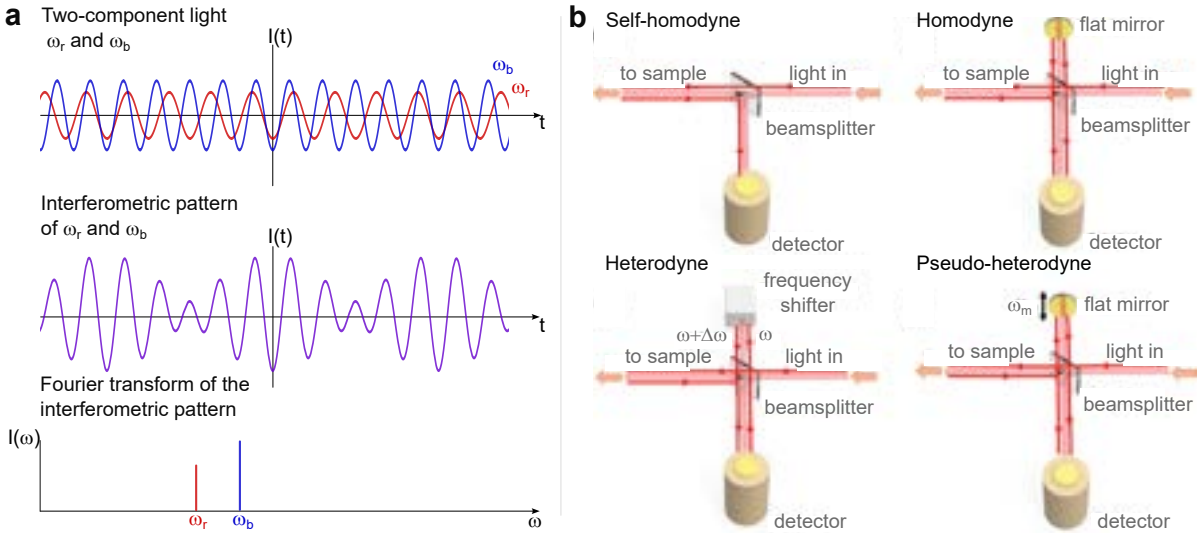

Figure 11 – Fourier transform method and detection modes. (a) An interferogram pattern is generated when light of frequency ω_r interferes with light of frequency ω_b, in which an intensity maximum is perceived when both components are in phase and constructively interfere. The Fourier transform of this interferogram therefore gives two discrete components in the frequency/momentum space that correspond to ω_r and ω_b. (b) The most common FTIR detection modes are based on a Michelson interferometer. In self-homodyne mode, light from an IR source interacts with the sample and interferes with itself in the detector. In homodyne mode, this light is divided into two components and interferometry is performed between a component that passes through the sample and the other that does not. In heterodyne mode, the reference arm is frequency modulated, gaining a $\Delta\omega$ shift. Finally, in pseudo-heterodyne mode, this modulation is done by introducing a phase/path difference in the system by the oscillatory movement of a mirror. Adapted from [7].

In micro-FTIR, the detection is done interferometrically and the spectrum is obtained via Fourier transform of the interferogram [101]. That is, using a Michelson-like interferometric scheme, a reference IR beam is split in two by a beamsplitter. Half of

the beam interacts with the sample, while the other half does not. Both beams interfere again generating an interferogram that depends on the optical path difference, which in turn carries information about the absorption properties of the sample [101]. For a monochromatic IR source, the Fourier transform is trivially a discrete component in frequency space. On the other hand, broadband continuous IR sources, such as thermal sources or synchrotrons, produce a very narrow interferogram, whose Fourier transform results in a wide spectrum due to the convolution of several frequencies [101]. This Fourier transform concept is depicted in Fig. 11a. To obtain an IR absorption response only from the sample, the measured spectrum must be normalized to a background reference spectrum. This reference spectrum is a convolution of system characteristics such as the radiation profile of the IR source, atmospheric absorption and detector efficiency [101]. In addition, there are different detection modes that can be implemented in order to perform interferometry, as depicted in Fig. 11b. The difference between them consists in the type of processing that is applied in the reference arm of the interferometer. The reference component can therefore be disregarded (self-homodyne), just reflected by a mirror (homodyne) or modulated either by frequency (heterodyne) or by introducing a phase shift (pseudo-heterodyne).

However, micro-FTIR is a diffraction-limited technique. This means that we cannot unambiguously distinguish two point sources separated by a distance smaller than $d = \lambda/2\text{NA}$, where λ is the wavelength of the radiation and NA is the numerical aperture of the optical system that is related to the angles it can receive/emit light. As IR radiation extends from the red edge of the visible spectrum near 14000 cm^{-1} wavenumber to the microwave edge at 10 cm^{-1}, which comprises micrometer wavelengths, the spatial resolution of the technique is on the order of micrometers. In practice, the micro-FTIR beam size using a conventional thermal IR source can reach a lower resolution limit of tens of micrometers and be further reduced to 3-5 μm using a synchrotron radiation source [102]. The use of synchrotron IR radiation not only improves the spatial resolution of the technique but also allows the investigation of very low concentrations of chemical species due to minimal signal loss [103]. However, working with 2D systems, like FL phyllosilicates, implies dealing with samples of micrometer size and nanometer thickness. Thus, we need to use advanced nanoprobe techniques to overcome the diffraction limit if we want to resolve nanometer-sized structures with different IR absorption properties. This can be done by combining the high spatial resolution of AFM technique with the high chemical specificity of FTIR when exploring the near-field regime of the light-matter interaction using IR s-SNOM.

Regarding the AFM aspects of s-SNOM, the measurement is performed in tapping mode with metal-coated tips similar to those used in KPFM. The tapping mode operation is very suitable for the s-SNOM technique since the tip oscillation gives rise to a modulation in the scattered optical signal that will be crucial to separate the near-field contribution

from the far-field [101]. The metallic coating of the tip is required in order to increase its plasmonic response when IR radiation is focused on the tip region. This phenomenon is caused by the concentration of charges near the apex of the tip due to the electrostatic lightning rod effect. When the IR radiation is focused on the tip, a collective resonant oscillation of the electrons with the radiation field occurs. This effect is known as localized surface plasmon resonance and causes a strong localization of the optical fields at the apex of the tip [104]. This effect is depicted in Fig. 12a by a numerical simulation of the field enhancement around a metal cone with a sharp apex to represent the tip that is illuminated with IR light. The tip acts like an antenna that concentrates the illuminating electric field to a nanoscale spot. The tip-sample interaction under illumination can be modeled as a coupled dipole using a charge-image approach [104, 105]. The electric field from the incident IR radiation polarizes the tip with an electric dipole moment and we can assume that it is oriented along the tip-axis. Since the tip localizes the electrical fields around it, the field strength perceived by the sample decays exponentially with increasing the tip-sample distance. Thus, only when the tip is very close to the sample it polarizes the sample creating a mirror dipole that interacts back with the tip dipole. This feedback polarization represents the near-field interaction between the tip and the sample. Although the near-field interaction is evanescent, it modifies the light scattered by the tip that reaches the detector, allowing us to extract the near-field information contained in the scattered light in a s-SNOM experiment [100, 101, 105].

The near-field interaction can be described by the complex scattering coefficient $\sigma_{nf} = s_{nf}e^{i\phi_{nf}}$, where s_{nf} is the amplitude and ϕ_{nf} is the phase. The scattered field E_s relates with the incident field E_i according to $E_s = \sigma_{nf}E_i$ [101]. The backscattered light is collected by a parabolic mirror that is also used to focus the incident light at the tip region. Then, the scattered light interferes with the reference in an interferometric scheme similar to those depicted in Fig. 11b. The resulting interferogram can be recorded by an IR detector such as the liquid nitrogen-cooled mercury cadmium telluride (MCT) detector commonly also used in conventional micro-FTIR experiments. Typically, a broadband source and a homodyne interferometric scheme are used to perform nano-FTIR spectroscopy using s-SNOM technique. However, to perform chemical contrast nanoimaging, the tip is illuminated at a specific frequency by tunable lasers, such as quantum cascade lasers, and a pseudo-heterodyne interferometric scheme is used [8], as depicted in Fig. 12c. When the interferometry is performed in pseudo-heterodyne mode, an extra modulation is added to the optical signal by the periodic displacement of a mirror [8]. The mirror displacement introduces a path difference d between the two interferometric arms, such that the intensity at the detector will change accordingly. Thus, when the two components E_a and E_b of the incident light (divided by the beamspliter) interfere, the intensity at the detector is then given by $I_D(d) \propto |E_D E_D^*|$ where $E_D = E_a + E_b$ [8,101]. The electric field of each component of IR radiation with frequency ω after the beamspliter can be generically described by

$E_a = |E_a|e^{i\omega t}$ and $E_b = |E_b|e^{i\omega t+\phi(d)}$, in which the phase difference $\phi(d) = 4\pi\omega d$ is introduced by the path difference d [101]. Thus, the intensity at the detector will change accordingly to $I_D(d) \propto |E_a|^2 + |E_b|^2 + 2|E_a||E_b|\cos(4\pi\omega d)$. By a linear movement of the reference mirror, the signal intensity at the detector will change sinusoidally [8, 101].

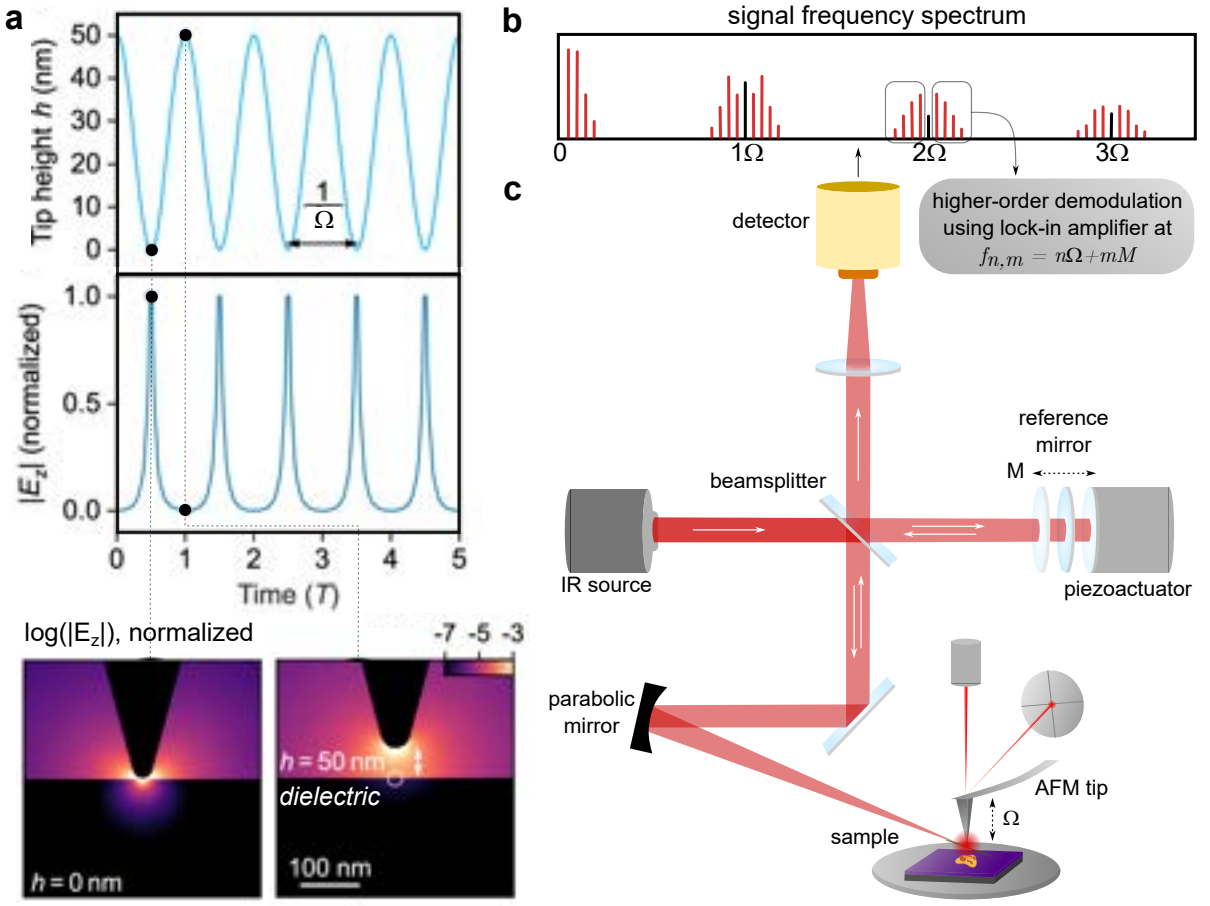

Figure 12 – Near-field interaction and s-SNOM instrumentation for nanoimaging. (a) The metal-coated tip apex oscillating at frequency Ω (top) is illuminated with IR radiation (frequency $\omega = 30$ THz; wavelength $\lambda = 10\mu$m) and the modulus of the out-of-plane electric field component $|E_z|$ (middle) is calculated by finite element methods for the tip-sample distance h at $h = 0$ nm (left-side, bottom) and $h = 50$ nm (right-side, bottom). For a tip-sample distance of about 50 nm, the near-field interaction disappears. This highly non-linear character of the near-field interactions, which varies with tip oscillation, gives rise to a (b) complex frequency spectrum of the detected signal when a (c) pseudo-heterodyne interferometric scheme is used, in which a modulation of phase is introduced through the movement of a reference mirror, giving rise to the sidebands that allow the demodulation of the near-field signal free of the background contribution. Adapted from neaspec by attocube ©, [8], and [9].

Since IR s-SNOM operates in tapping mode, the tip is vertically vibrating at frequency Ω above the sample. The tip oscillation produces a strong modulation of the scattered near-field due to its non-linear character, while the background far-field is only weakly modulated [101]. Using a pseudo-heterodyne interferometric scheme, the optical signal is also phase-modulated by the mirror displacement with frequency M using a

piezoactuator coupled to the mirror. The combined effect of tip-oscillation and phase-modulation of the reference arm produces a rich frequency structure in the detected signal [8, 101], with spectral components appearing at frequencies $f_{n,m} = n\Omega + mM$ as shown in Fig. 12b. Using a lock-in amplifier, we can demodulate the signal at sidebands of higher harmonics of the tip-oscillation to suppress the far-field contribution [8, 101, 106]. The suppression is based of the fact that higher harmonics are sensitive to faster signal changes that are only related to near-field interactions due to their highly non-linear character [105]. The possibility of measuring the amplitude and phase of pure near-field scattering contrast by lock-in demodulation allows to measure the complex scattering coefficient σ_{nf}. Once the complex scattering coefficient is defined as the ratio of the scattered to the incident field strength, it depends on the effective polarizability of the system [105]. Thus, the relative strength of the s-SNOM signal can be directly compared to the effective polarizability obtained from the dipole model, allowing to extract the local complex dielectric function $\epsilon(\lambda)$ of the sample by measuring σ_{nf} [105]. This allows obtaining nanoscale resolved optical images of a sample from which we can determine the local chemical composition with resolution limited only by the tip radius of about 20 nm using the IR s-SNOM technique.

4 Sample characterization

The characteristics of natural minerals are directly related to their formation geological environments. Distinct geological origins can result in structural and chemical variations that can change the fundamental properties of the materials. Thus, a mandatory step prior to discussions concerning the physical and chemical properties of natural crystals is a global characterization of the samples in bulk and FL forms. In the next sections, structural and morphological characterizations will be presented, as well as a careful analysis of impurities and vibrational properties of clinochlore and phlogopite phyllosilicate minerals. The results presented in this section are part of two published articles produced as a direct contribution of this thesis, one of the works entitled *"High throughput investigation of an emergent and naturally abundant 2D material: Clinochlore"* [35] referring to the characterization of clinochlore and the other entitled *"Exploring the structural and optoelectronic properties of natural insulating phlogopite in van der Waals heterostructures"* [30] on the characterization of phlogopite.

4.1 Structural and morphological characterization

4.1.1 Clinochlore

Initially, it is necessary to correctly determine the crystalline structure with its possible phases and composition of the samples. Starting with the chlorite specimen, structural and elementary analysis by XRD, EDS and WDS were carried out to confirm the arrangement and composition of our clinochlore sample extracted from Minas Gerais/Brazil geological environment. This is crucial to understand the structural and chemical variations that can occur in relation to a pristine mineral (crystallographically perfect and without impurities) due to the fact that the sample is of natural/geological origin. Subsequently, the clinochlore sample was mechanically exfoliated onto (300 nm) SiO_2/Si substrates and a morphological analysis of clinochlore in its FL form was performed using OM and AFM techniques.

To confirm the crystalline structure of our clinochlore sample, we performed powder XRD measurements in a milled clinochlore combined with a phase matching through refinement using the MAUD package [107] (Fig. 13a). The most simplified combination of two phyllosilicate minerals that could provide the best fitting to the experimental data with match of peak intensities and positions was retrieved for a volumetric combination of 91(1)% clinochlore [108] and 9(1)% vermiculite [109]. The amount of vermiculite alteration may be due to natural weathering or hydrothermal processes [22]. The parameters retrieved for the

clinochlore phase are $a = 5.3488(6)$ Å, $b = 9.5284(5)$ Å, $c = 14.4241(5)$ Å, $\alpha = 90.93(1)°$, $\beta = 97.72(1)°$ and $\gamma = 88.09(1)°$, leading to a composition and site occupancy compatible with the parameters reported on literature [108]. The vermiculite parameters were held according to the literature [109]. In this sense, our clinochlore sample is strictly a triclinic structure (P-1 space group), but with high monoclinic correspondence. This suggests that the lamellar structure of our clinochlore sample is formed by a T-Oc-T stacking intercalated by *brucite-like* layers as expected, but with some stacking faults that reduces the crystal symmetry. The phase matching was performed also considering a 25% of Cr occupation in the octahedral Al sites.

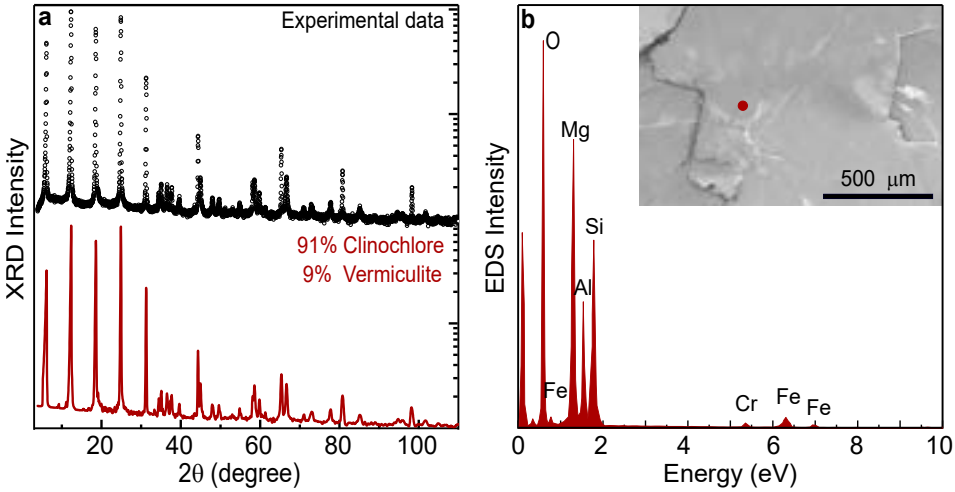

Figure 13 – Structural and qualitative elementary analysis of clinochlore. (a) XRD measurements and phase matching for the clinochlore powder show that the experimental data (black dots) are well fitted with two phases by refinement using the MAUD package (red line) with 91(1)% contribution of clinochlore and 9(1)% of vermiculite. (b) Representative EDS spectrum of bulk clinochlore acquired at the red dot in the SEM image.

WDS	(wt%)
SiO_2	31.4(3)
MgO	31.0(2)
Al_2O_3	16.8(3)
FeO	6.8(4)
Cr_2O_3	0.6(1)
H_2O/OH	13.4(5)

Table 1 – Quantitative elementary analysis of clinochlore by WDS.

To further study the composition of our crystal, we performed EDS and WDS analysis. Fig. 13b shows a representative EDS spectrum for clinochlore. An EDS elementary qualitative analysis, using data from ten distinct points of the bulk clinochlore sample, confirms the XRD model through identification of the constituent elements (O, Mg, Si and Al) with the presence of Cr. EDS measurements also reveal a significant existence of Fe impurities, which are commonly reported to occur in phyllosilicate minerals as substitutional ions at octahedral sites [110]. Quantitative analysis by WDS is given in

Table 1, which provides a remaining contribution of about 13 wt% attributed to the presence of water/hydroxyl ions in the clinochlore mineral. The WDS analysis also confirms that the content of Fe impurities is very relevant, corresponding to about 7 wt%, while Cr impurities are present in a less expressive amount in our clinochlore sample.

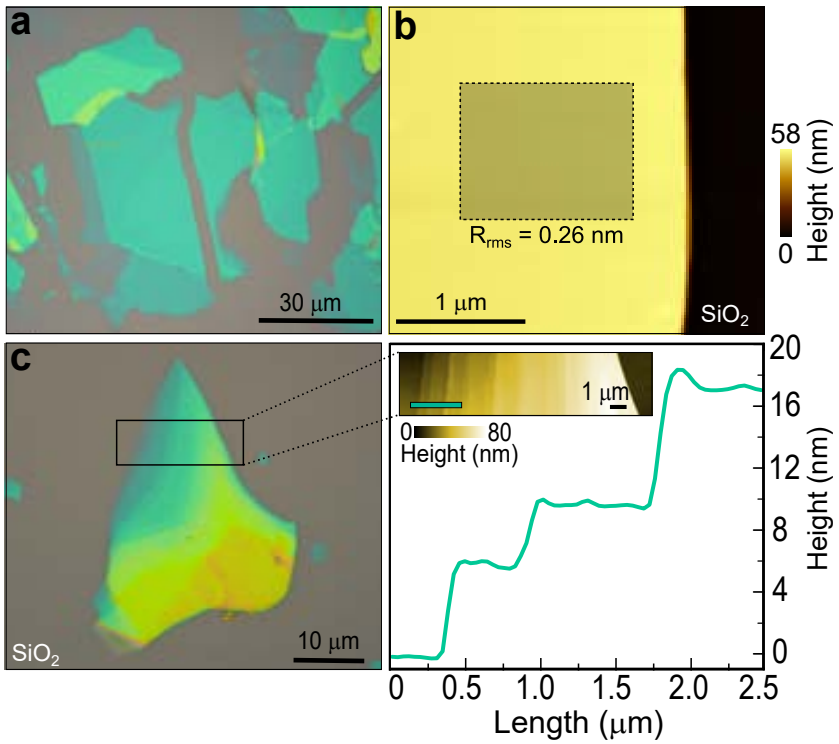

Figure 14 – Morphological characterization of mechanically exfoliated clinochlore. (a) Optical microscopy image of several clinochlore flakes exfoliated on a (300 nm) SiO_2/Si substrate. The different colors of the flakes correspond to different thicknesses. (b) AFM topography image of a clinochlore flake with approximately 58 nm of thickness and average roughness (R_{rms}) calculated in the area delimited by the shaded square. From an isolated clinochlore flake (left side (c)), an AFM topography image of the highlighted region was acquired (insert in right side (c) graph) and the corresponding profile along the green line in the AFM image was taken (right side (c) graph).

After a comprehensive structural-chemical characterization of the bulk material, we must investigate nanometer-thin 2D clinochlore flakes produced by mechanical exfoliation, since the material has weak van der Waals forces between layers. For that, a standard scotch tape technique was carried out to obtain several clinochlore flakes onto (300 nm) SiO_2/Si substrates. The result is depicted in the OM image of Fig. 14a. The apparent color of the flakes depends on their thickness [111] that varies from a few nanometers up to hundreds of nanometers. The lateral flake size depends directly on the exfoliation process (scotch tape repetition) and it may vary from sample to sample. In order to obtain phyllosilicate flakes with controlled distribution of shape and size, other exfoliation methods such as liquid phase exfoliation can be applied [112, 113]. We then performed morphological surface analysis by AFM in a representative clinochlore flake. Similar to other LMs, for instance hBN [18], clinochlore shows atomically flat surfaces over large

areas. Fig. 14b shows an AFM topography image of a clinochlore flake with approximately 58 nm of thickness with average roughness $R_{rms} = 0.26$ nm obtained by statistical analysis using Gwyddion software [114]. This result indicates that our sample has a suitable surface topography for application as a substrate or encapsulating media for other LMs in vdWHs that are crucial to the fabrication of nanodevices, such as field effect transistors [115–117].

Fig. 14c shows another OM image of an isolated clinochlore flake. A high-resolution AFM topography image was acquired from the highlighted area in the OM image, from which the corresponding profile from the substrate to the *stair-like* clinochlore flake was extracted. The green line in the high-resolution AFM topography image indicates the profile extension. We can observe a step height of 6 nm between the substrate and the first adjacent terrace, corresponding to approximately 4 layers of clinochlore, while the next step has a height of 3 nm, corresponding to approximately 2 layers. The results clearly distinguish few nanometer-thick layers within the clinochlore flake, suggesting that an isolated 1L-clinochlore could be eventually produced and identified by AFM.

4.1.2 Phlogopite

As well as for clinochlore, we start by discussing the structural characterization of our natural phlogopite crystal also extracted from Minas Gerais/Brazil geological environment. Fig. 15a plots the powder XRD measurement of a milled phlogopite sample to confirm its structural and chemical composition. The sharp and intense peaks clearly show the crystalline nature of the sample. Given the natural/geological origin of the sample, different phases of phyllosilicates were searched to provide possible fits with the presence of major and minor phases. The most simplified combination of two phyllosilicate minerals that could provide the best phase matching to the experimental data using the MAUD package [107] was retrieved for a volumetric combination of 98(1)% phlogopite [118] and 2(1)% biotite [119]. The parameters retrieved for the dominant phlogopite phase are $a = 5.338$ Å, $b = 9.229$ Å, $c = 10.284$ Å, $\alpha = 90°$, $\beta = 99.99°$, and $\gamma = 90°$. The retrieved lattice parameters correspond to a monoclinic structure (C2/m space group) with composition and occupation consistent with those reported in the literature [120, 121]. In phlogopite specimens, the lattice parameters may vary with the increasing contents of cations with different ionic radius [122].

Next, a qualitative elementary analysis of the chemical composition of the bulk phlogopite sample was made at ten different points by EDS. We could observe the presence of the constituent elements of phlogopite (O, K, Mg, Al and Si) and Fe impurities in all analyzed points. A representative EDS spectrum for one of the analyzed points can be seen in Fig. 15b. Quantitative analysis was performed by WDS, resulting in a contribution in weight summarized in Table 2. The predominant impurity in our phlogopite sample is also iron and we can observe a considerable amount of water/hydroxyl of approximately

6%, but inferior compared to clinochlore.

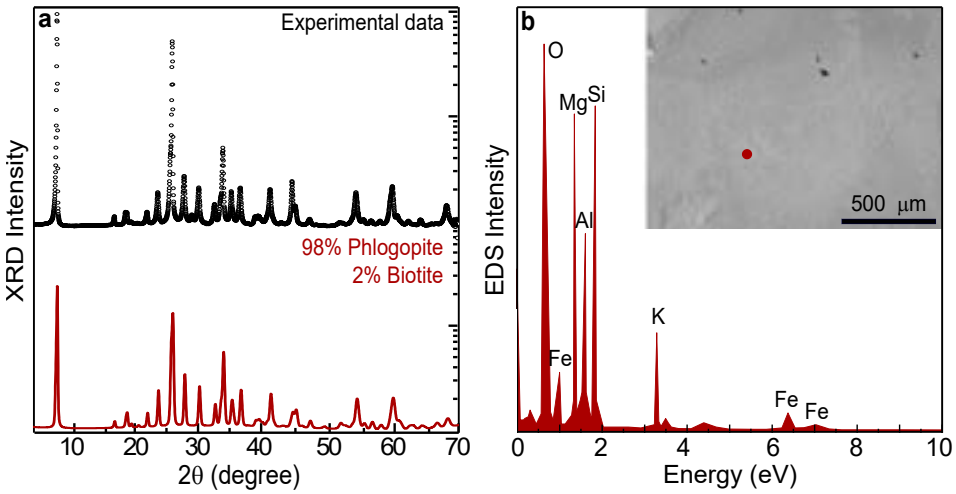

Figure 15 – Structural and qualitative elementary analysis of phlogopite. (a) XRD measurements and phase matching for the phlogopite powder show that the experimental data (black dots) are well fitted with two phases by refinement using the MAUD package (red line) with 98(1)% contribution of phlogopite and 2(1)% of biotite. (b) Representative EDS spectrum of bulk phlogopite acquired at the red dot in the SEM image.

WDS	(wt%)
SiO_2	41.9(8)
MgO	24.7(6)
Al_2O_3	15.6(3)
K_2O	6.9(1)
FeO	5.0(1)
H_2O/OH	5.9(8)

Table 2 – Quantitative elementary analysis of phlogopite by WDS.

In the following, we use the fact that phlogopite has weak van der Waals forces between the layers and strong in-plane bonds to apply the mechanical exfoliation technique for obtaining ultrathin flakes. Fig. 16a shows the OM image of several phlogopite flakes obtained by direct exfoliation of a bulk sample onto a (300 nm) SiO_2/Si substrate. It is possible to identify flake sizes varying from hundreds of nanometers up to hundreds of microns. We selected a representative *stair-like* phlogopite flake (Fig. 16b) to acquire an AFM topography image (Fig. 16c). Analyzing the phlogopite topography, we identify that, as for hBN [18], phlogopite shows atomically flat surfaces over large areas, with average roughness $R_{rms} = 0.26$ nm obtained by statistical analysis using Gwyddion software [114]. This result indicates that phlogopite crystals show good surface topography to be embedded in vdWHs. Furthermore, the large area of nanometer-thick phlogopite flakes makes it promising candidate for use not only as substrates in nanodevices based in LMs, but also as insulator barriers in planar tunnel junctions or as dielectrics in field-effect transistors and nanocapacitors [31,32,71]. We also extracted two height profiles in the phlogopite flake. The black and green lines in the AFM topography image indicate the profile extensions.

We can observe a step height of 0.7(3) nm in the profile extracted along the black line that corresponds to an 1L-phlogopite [31, 123], while the step in the profile extracted along the green line has a height of 3.2(3) nm, corresponding to approximately 3L-phlogopite.

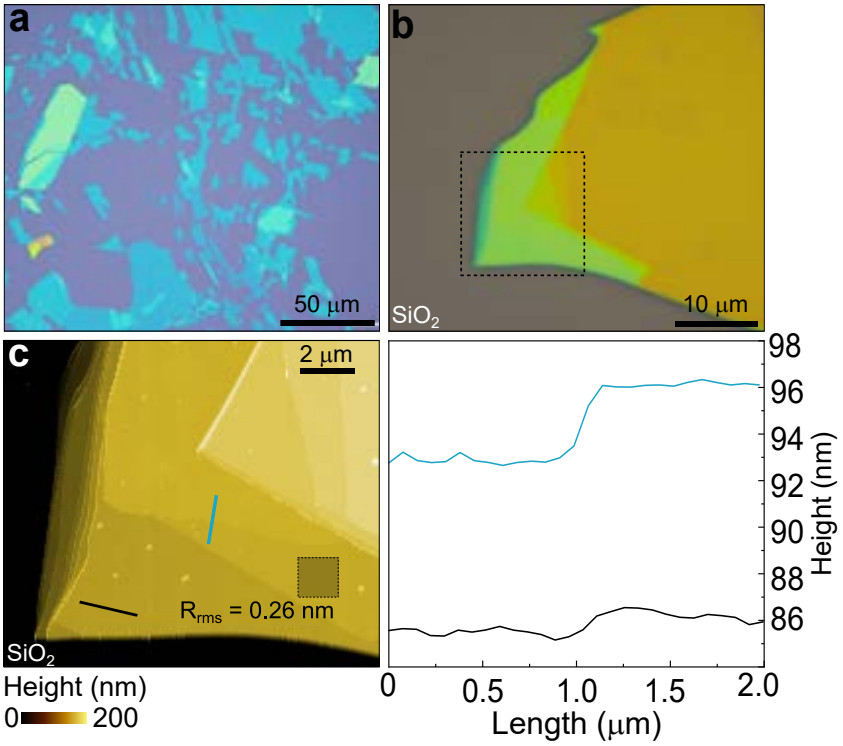

Figure 16 – Morphological characterization of mechanically exfoliated phlogopite. (a) Optical microscopy image of several phlogopite flakes exfoliated on a (300 nm) SiO_2/Si substrate. The different colors of the flakes correspond to different thicknesses. (b) Optical microscopy image of a selected *stair-like* phlogopite flake from which we acquired an (c) AFM topography image of the highlighted region. We analyzed the average surface roughness of the flake in the region delimited by the dashed square and also plotted two height profiles extracted along the black and green lines (right side (c)).

4.2 Point defects and impurities characterization

It is expected that impurities and defects can strongly affect the fundamental properties of any material, including phyllosilicates. As mentioned earlier in the section 2, iron is an abundant element in the geological formation environment of phyllosilicates [52]. Iron can be present as an inclusion or as a substitutional impurity in different sites, coordination and valence states simultaneously. Each of these configurations can change the macroscopic properties of the studied minerals in a different way. A less expressive amount of other types of substitutional impurities is also expected. Therefore, in this section we carried out a detailed analysis of the impurities present in our clinochlore and phlogopite samples. With this, it was possible to understand how impurities play a crucial role in determining some of the macroscopic properties of these minerals.

4.2.1 Clinochlore

The impurities present in clinochlore were previously identified by EDS and WDS elementary analysis. To further analyze these impurities, EPR measurements, Mössbauer spectroscopy and optical absorption in UV/Vis/NIR were performed, as well as XRF and XANES measurements using synchrotron radiation.

Fe ions can be present in the clinochlore structure in different oxidation states, Fe^{2+} and Fe^{3+}. Fe^{2+} ions with ($3d^6$) electronic configuration are a non-Kramer ions, being generally unobservable by EPR [124, 125]. However, Fe^{3+} ($3d^5$) ions with an effective electronic spin $S = 5/2$ has been extensively investigated for several minerals, where Fe^{3+} ions are commonly present [61, 65, 66, 110]. Fig. 17a shows the EPR angular dependence obtained at X-band microwave frequency and at room temperature for the bulk clinochlore sample, for rotation of the sample with the c axis perpendicular to the rotation axis. The EPR spectra reveal an anisotropic main line with effective g value varying between $g \sim 4$ and $g \sim 2$. Some unresolved anisotropic lines at lower-field are also observed. For the angular dependence of EPR spectra with the rotation axis parallel to the c axis (not shown), only a broad unresolved isotropic signal around $g \sim 4$ is observed. The EPR measurements suggest that the Fe^{3+} ions are situated in the expected octahedral sites, but distorted by a strong rhombic crystalline field, commonly reported in the literature and expected for the low-symmetric clinochlore structure [65, 66, 110, 126]. Previous works also report an isotropic EPR line at $g \sim 2$ for non-structural Fe ions [65, 126], which are not observed in our spectra, indicating that the Fe^{3+} ions present in our clinochlore sample are mainly substitutional ions in distorted octahedral sites. In addition, a broad line at $g \sim 2$ expected due to the Cr^{3+} contribution [61] is not observed in our EPR spectra, but this signal may have been suppressed by the high amount of Fe. It is important to note that each possible EPR transition is dependent of the orientation of the applied magnetic field with respect to the symmetry axes of the crystalline field [125]. The paramagnetic line broadening of our EPR measurements may be associated with the superposed contribution of paramagnetic centers differing so slightly due to the non-aligned stacking of our clinochlore lamellar structure so that their particular signals cannot be resolved [66]. Another possibility for the occurrence of line broadening in EPR spectra may be due to the exchange between the Fe ions.

Fig. 17b shows the EPR spectra at the specific orientations 180° and 90° of the angular dependence. Despite the non-sensitivity of the EDS and WDS techniques to identify the presence of Mn in the sample due to its lower content ($< 0.1\%$), the presence of Mn in the sample is evident from the EPR spectrum at 90° orientation. This identification is possible due to the fact that the observation of six well-resolved lines with the same intensity and spacing arise from the hyperfine interaction of the Mn^{2+} paramagnetic ions with the ^{55}Mn isotope with nuclear spin $I = 5/2$ and natural abundance 100%. The

EPR signal attributed to the existence of Mn impurities in the clinochlore structure is isotropically present in all orientations of the angular dependence. However, for some orientations, such as 180°, the intensity of the EPR signal associated with Fe impurities dominates the spectrum at approximately $g = 2$ and we cannot properly observe the hyperfine lines of Mn, since the intensities of EPR signals are proportional to the content of paramagnetic centers in the material volume [124].

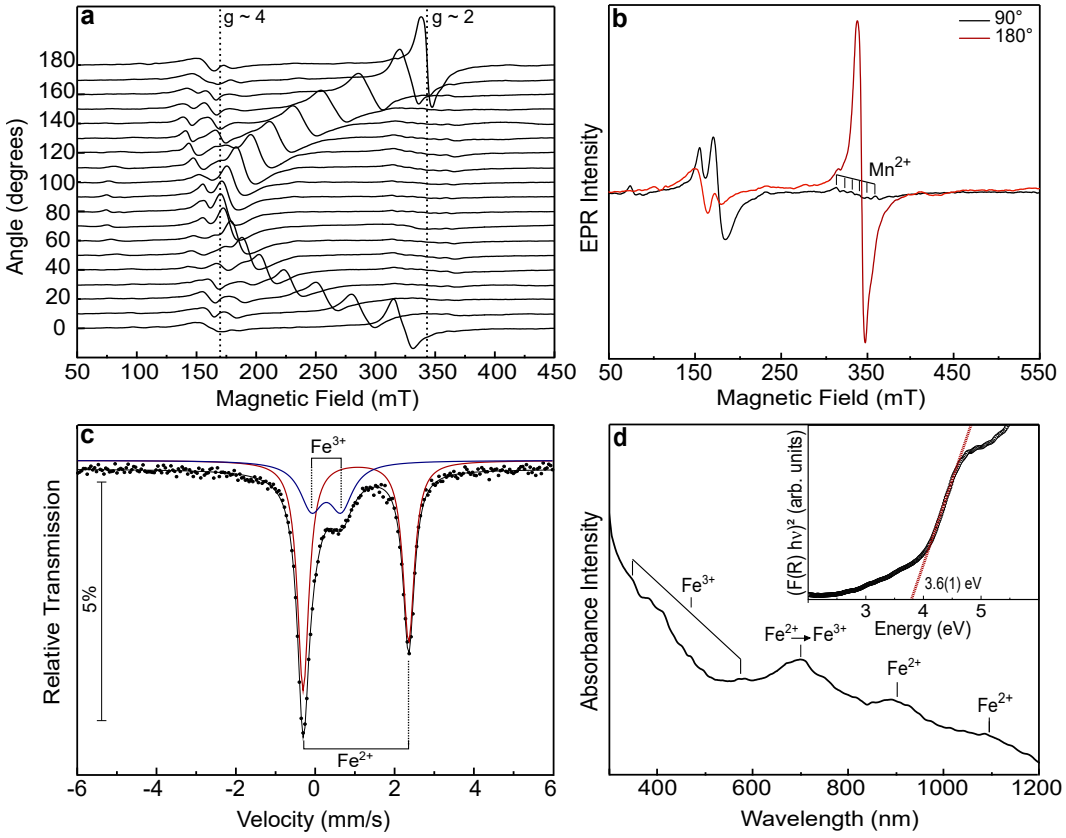

Figure 17 – Impurities in clinochlore analyzed by EPR, Mössbauer spectroscopy and optical absorption in UV/Vis/NIR. (a) The angular dependence of clinochlore EPR spectra at 9.436(1) GHz with the c axis perpendicular to the rotation axis indicate a typical dependence of Fe^{3+} ions in an orthorhombic environment. (b) The EPR spectra at the specific orientations 180° ($B \parallel c$) and 90° from the angular dependence. The presence of Mn in the sample is evident from the spectrum at the specific orientation 90° by the appearance of six well-defined lines. (c) Mössbauer spectrum of clinochlore fitted with Fe^{2+} (red line) and Fe^{3+} (blue line) doublets contributing with 69.5% and 30.5% respectively. (d) The UV/Vis/NIR absorbance spectrum of a suspended clinochlore flake confirms the presence of Fe impurities in different oxidation states. The inserted Tauc plot in shows an experimental estimation of 3.6(1) eV for the clinochlore optical bandgap energy.

Since EPR measurements are unable to detect the presence of Fe^{2+} ions, Mössbauer absorption measurements were performed. Table 3 lists the hyperfine fitting results for the isomer shift, quadrupole splitting, full width at half maximum and absorption areas of the two doublets. Fig. 17c shows the corresponding fitted Mössbauer spectrum. The major doublet (red line) is assigned as Fe^{2+} and the smaller doublet (blue line) to Fe^{3+}. The Fe^{2+} doublet exhibits intensity asymmetry of its two lines, which is due to the preferred

orientation of the microflakes relative to the Mössbauer setup. This result indicates that the direction of the electric field gradient must be perpendicular to the plane of the microflakes. From the absorption areas of the two doublets, 69.5% for Fe^{2+} and 30.5% for Fe^{3+}, we can conclude that the Fe impurities enter in the clinochlore structure preferentially in the bivalent state.

Dublet	δ (mm/s)	Δ (mm/s)	Γ (mm/s)	Área ($\pm$0.1%)
Fe^{2+}	1.13	2.65	0.35	69.5
Fe^{3+}	0.39	0.75	0.70	30.5

Table 3 – Hyperfine Mössbauer parameters adjusted for two Fe doublets, with the respective values of isometric shift (δ), quadrupole splitting (Δ), width (Γ) and area. The errors of the hyperfine parameters (δ, Δ, Γ) are estimated to be $\pm$0.01 mm/s and $\pm$0.02 mm/s for Fe^{2+} and Fe^{3+}, respectively.

From the UV/Vis/NIR absorbance spectrum of a suspended clinochlore flake (Fig. 17d), we observe different absorption bands associated with Fe impurities in both Fe^{2+} and Fe^{3+} valence states. The absorption bands observed below 600 nm are related to orbital electronic transitions of Fe^{3+} ions, while the two broad bands at around 900 nm and 1100 nm are due to the presence of Fe^{2+} ions [110]. The absorption band observed at around 700 nm in the middle of the explored spectral range was previously attributed to the charge transfer between iron ions Fe^{2+}-Fe^{3+} [110]. Absorption bands associated with Cr^{3+} ions are expected to be observed around 430 nm and 610 nm [110] and may have been suppressed by Fe absorption bands, since our WDS quantitative analysis reveal that the Fe content is much more relevant than the Cr amount. In order to experimentally determine the optical bandgap energy of the studied clinochlore sample, a Tauc plot (inserted graph in Fig. 17d) was elaborated from reflectance measurement performed in the same setup of the absorbance measurements. The bandgap energy was obtained by extrapolation of the linear behavior (red dashed line) of the Kubelka-Munk function of our experimental data [127,128]. Considering a direct bandgap for the clinochlore, we obtain an experimental bandgap energy of 3.6(1) eV.

Due to the high Fe content in the clinochlore sample studied, it was possible to analyze this impurity by various techniques, such as EPR, Mössbauer and UV/Vis/NIR absorption. However, little experimental information could be obtained for Mn and Cr impurities by the complementary techniques already discussed. The quantification obtained by WDS was capable to point out traces of Cr in the sample, but the allowed absorption bands in the visible region associated with Cr ions could not be properly identified most likely due to the domination of the Fe bands in the spectrum in Fig. 17d. EPR measurements clearly show the Mn spectral signature, confirming the presence of this impurity in the sample, but no trace of Mn was quantified by WDS analysis, indicating that the amount of Mn in the clinochlore sample is not expressive. In an attempt to clarify this discussion, XRF measurements are performed on a 500 μm x 500 μm panoramic

clinochlore area, resulting in the impurity maps shown in Fig. 18a-c with normalized intensity for each investigated metal (Fe, Mn and Cr).

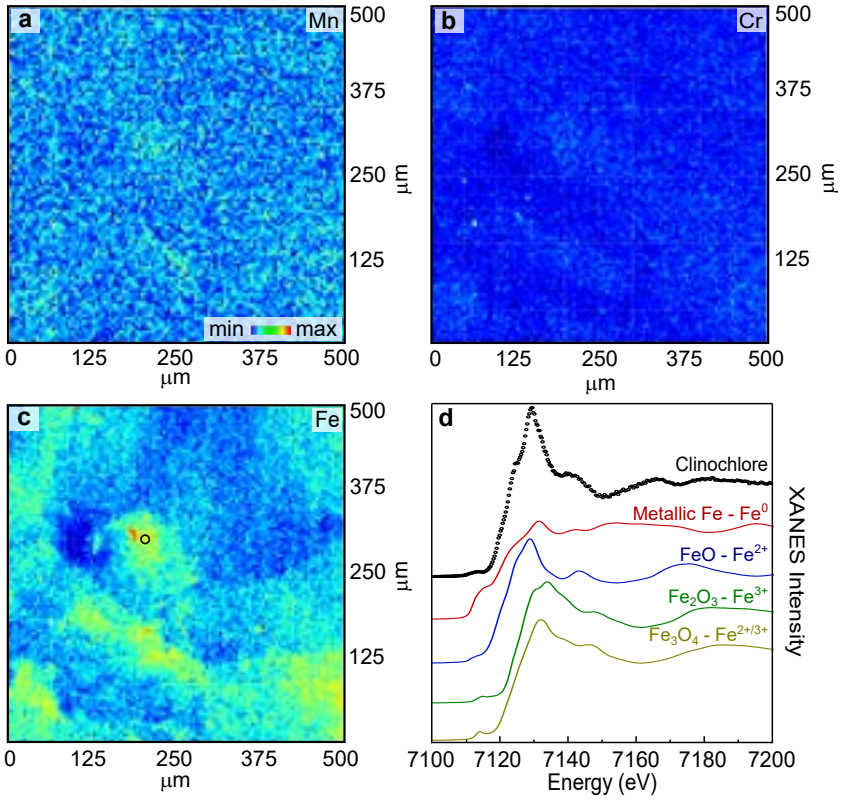

Figure 18 – Impurities in clinochlore analyzed by XRF and XANES using synchrotron radiation. Fluorescence normalized intensity hyperspectral maps acquired under 9.750 eV X-ray synchrotron excitation for the transition metal impurities (a) Mn, (b) Cr and (c) Fe present in the clinochlore flake. (d) Nanometric XANES spectrum recorded at the black circle delimited region in (c) around Fe K-edge energy in comparison with standard iron oxides presenting iron in different valency states (solid lines).

We can observe a homogeneous distribution of Mn and Cr impurities over the investigated area, suggesting that they preferentially incorporate into the clinochlore structure. On the other hand, the XRF map for Fe impurities reveals an inhomogeneous distribution over the sample area, indicating that part of the iron content in the sample forms inclusions. From the extensive analysis of the Fe impurities in our sample by the techniques previously described, it is known that the Fe ions are predominantly bivalent by Mössbauer analysis. On the other hand, EPR measurements determine that Fe^{3+} ions are present in the sample in distorted octahedral sites and the absence of an isotropic line at $g \sim 2$ excludes the possibility that trivalent Fe ions are present in the sample at non-structural sites in significant amounts. For these reasons, our results suggest that Fe inclusions in the clinochlore should preferably be constituted of Fe^{2+} ions. Exploring the possibility of iron inclusions formed mainly by bivalent ions, we performed XANES measurements in a nanometric region enclosed by the black circle in Fig. 18c. The respective XANES spectrum recorded around the Fe K-edge energy is plotted in Fig. 18d in qualitative

comparison with standard reference data of iron oxides presenting iron in different valence states. Comparatively, the experimental data is well described by the XANES spectrum of the FeO standard over the others, corroborating the idea suggested by our results that the constitution of the inclusions is dominated by bivalent Fe ions.

4.2.2 Phlogopite

Once the presence of Fe in phlogopite was identified by EDS and WDS elementary analysis, it is important to evaluate in detail how this impurity is incorporated into the material. For this, EPR measurements, Mössbauer spectroscopy and optical absorption in UV/Vis/NIR were performed, as well as XRF and XANES measurements using synchrotron radiation.

The incorporation of Fe in the phlogopite structure can occur for both Fe^{2+} and Fe^{3+} ions, being frequently present in the phlogopite structure as substitutional ions in tetrahedral and octahedral sites [129], as discussed in section 2.2. For Fe^{3+} ($3d^5$) ions with effective electronic spin $S = 5/2$, at least four orthorhombic sites have already been identified by the EPR technique in the literature [92, 129, 130]. The more commonly reported sites are octahedral. One of the octahedral sites is determined by the Fe ion surrounded by four O and two OH in *trans*-configuration, while the other octahedral site is characterized by the OH in adjacent positions. EPR spectra from the literature indicate that Fe^{3+} ions experience a strong orthorhombic crystalline field that is sufficient to distort the local symmetry of the system ranging from axial to rhombic [129]. The octahedral site with adjacent OH ions is the most rhombic, resulting in an isotropic line in the EPR spectra at approximately $g = 4.2$ for phlogopite samples [92, 129, 130]. The octahedral site with transverse OH ions presents axial symmetry [129]. Fig. 19a shows the angular dependence of the EPR spectra for the phlogopite sample at room temperature performed by rotating the sample with the c axis perpendicular to the axis of rotation. There are some broad anisotropic lines at lower-field and an approximately isotropic line at $g = 4.2$, the latter being characteristic of the most rhombic octahedral site. For the angular dependence of the EPR spectra with the rotation axis parallel to the c axis (not shown), only an unresolved isotropic line around $g = 4.2$ was observed. EPR measurements are in agreement with previous works [91, 92, 129, 130] and suggest that Fe^{3+} substitutional ions are present in octahedral sites distorted by a strong rhombic crystalline field in the phlogopite sample. However, it was not possible to conclude about the presence or not of Fe^{3+} also in tetrahedral sites. The broadening of the low-field anisotropic lines may be associated with the exchange interaction between the Fe impurities or even with the slightly different orientations of the paramagnetic centers due to stacking faults, which slightly alter the local resonance condition and contribute in a superimposed way to the broadening of lines.

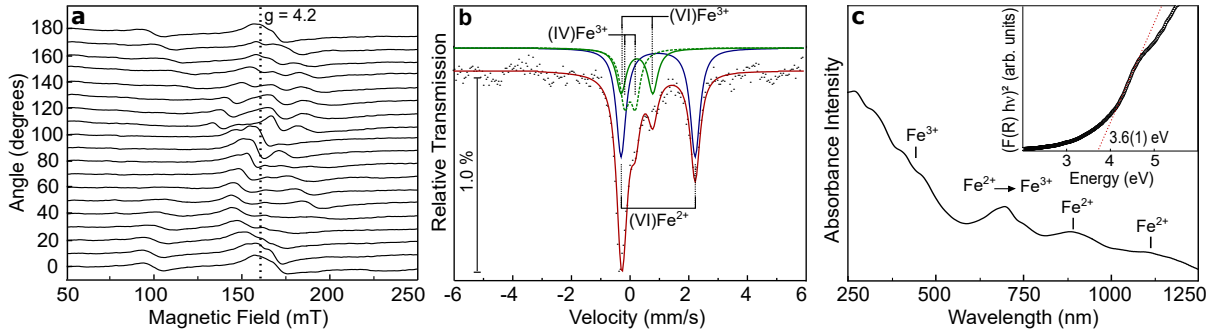

Figure 19 – Impurities in phlogopite analyzed by EPR, Mössbauer spectroscopy and optical absorption in UV/Vis/NIR. (a) The angular dependence of the EPR spectra for the phlogopite sample at 9.440(1) GHz with the c axis perpendicular to the rotation axis indicates a typical dependence of Fe^{3+} ions in an orthorhombic environment. (b) Fitted Mössbauer spectrum of phlogopite (red line) indicating the presence of Fe^{2+} ions at octahedral sites (blue line) and Fe^{3+} at octahedral (solid green line) and tetrahedral (dashed green line) sites with contributions of 53.7% and 46.3%, respectively. (c) The UV/Vis/NIR absorbance spectrum for phlogopite confirms the presence of Fe impurities in different valence states. The Tauc plot (inserted graph) shows an experimental estimation of 3.6(1) eV for the optical bandgap energy of phlogopite.

As the EPR technique is not able to evaluate the presence of Fe^{2+} ions, Mössbauer absorption measurements were performed. Table 4 lists the hyperfine-fitting results for isometric shift, quadrupole splitting, full-width at half-height, and doublet absorption areas at octahedral sites of six-coordinated (VI)Fe^{2+} and (VI)Fe^{3+} ions and the tetrahedral-site doublet of four-coordinated (IV)Fe^{3+} ion. Fig. 19b shows the measured Mössbauer spectrum and the corresponding fit (solid red line). The highest intensity doublet of the fit components (solid blue line) is assigned to (VI)Fe^{2+} ions, while the lowest intensity doublets are assigned to (VI)Fe^{3+} ions (solid green line) and (IV)Fe^{3+} ions (dashed green line), respectively of higher and lower quadrupole splitting. From the absorption areas, it is possible to quantify the relative contribution of iron ions in the phlogopite sample, such that 53.7% of the contribution is due to Fe^{2+} ions and 46.3% to Fe^{3+} ions. Thus, we can conclude that Fe impurities enter the phlogopite structure preferentially in the bivalent state in octahedral sites, while Fe^{3+} impurities can occupy both octahedral and tetrahedral sites, assuming different coordinations for trivalent ions in agreement with the literature [64, 131, 132].

Dublet	δ (mm/s)	Δ (mm/s)	Γ (mm/s)	Area
(VI)Fe^{2+}	1.11	2.52	0.35	53.7
(VI)Fe^{3+}	0.39	1.08	0.35	22.0
(IV)Fe^{3+}	0.16	0.37	0.35	24.3

Table 4 – Iron impurities in phlogopite analyzed by Mössbauer spectroscopy. Fitted Mössbauer hyperfine parameters for the Fe doublets, with the respective values of isometric shift (δ), quadrupole splitting (Δ), width (Γ) and area.

From the UV/Vis/NIR absorbance spectrum for the phlogopite sample shown in

Fig. 19c it is possible to observe different bands associated with Fe impurities in the Fe^{2+} and Fe^{3+} valence states. As with clinochlore, the absorption bands observed below 600 nm are related to the orbital electronic transitions of Fe^{3+} ions, while the two broad bands at approximately 900 and 1100 nm are due to the presence of Fe^{2+} ions [133, 134]. The absorption band observed at approximately 700 nm is attributed to charge transfer between iron ions [133, 134].

To determine the experimental optical bandgap energy of our phlogopite sample, a Tauc plot was obtained from a reflectance measurement, shown in the inserted graph on Fig. 19c. The bandgap value was obtained by extrapolating the linear behavior (dashed red line) of the Kubelka-Munk function from the experimental data [127, 128]. Considering a direct bandgap for phlogopite minerals [91], an experimental bandgap value of 3.6(1) eV was estimated for the sample, which is in agreement with previous work on natural phlogopites [135] and lower than predicted for synthetic phlogopites (7.8 eV) [136]. The presence of impurities in trioctahedral micas such as phlogopite is suggested as reason for the reductiong in bandgap energy of natural micas compared to synthetic ones [91, 136]. Iron is the main impurity responsible for the reduction of phlogopite bandgap energy [30].

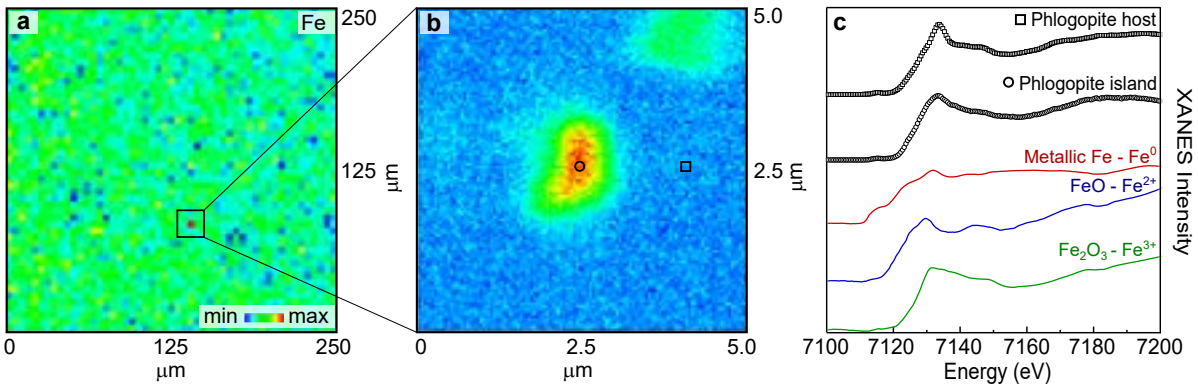

Figure 20 – Iron impurities in phlogopite analyzed by XRF and XANES using synchrotron radiation. Fluorescence normalized intensity hyperspectral maps acquired over a (a) 250 x 250 μm^2 region and over the highlighted area of (b) 5 x 5 μm^2 on phlogopite flake. The images were obtained from the selection of Fe K-alpha emission line, excited under 7.2 keV, and normalized by the intensity of the hottest pixel of each image. (c) Nanometric XANES spectra recorded at the island (black circle) and host region (black square) in (b) around Fe K-edge energy in comparison with standard iron oxides presenting iron in different valency states (solid lines).

XRF hyperspectral mapping were performed in areas of 250 x 250 μm^2 and 5 x 5 μm^2 of an exfoliated phlogopite with pixel size of 5 μm and 50 nm, respectively. The XRF impurity maps normalized for iron are shown in Fig. 20a for the panoramic area and Fig. 20b for the highlighted region. The Fe-impurity map shown in Fig. 20b was acquired at the hottest pixel region in the panoramic map. We performed XANES measurements in nanometric regions that correspond to the Fe-island and host. The respective XANES spectra recorded around the Fe K-edge energy are plotted in Fig. 18c

in qualitative comparison with standard reference data of iron oxides presenting iron in different oxidation states. Comparatively, the experimental data is well described by the XANES spectrum of the Fe_2O_3 standard over the others. This indicates a Fe^{3+} oxidation state for iron in both analyzed areas. Although Mössbauer spectroscopy analysis indicated a higher concentration of bivalent iron ions in our phlogopite sample, the XANES analysis indicate a higher contribution of trivalent iron ions. However, this difference may arise from the fact that the *mother*-sample is of natural origin and different parts of it were extracted for each measurement, which may have slightly different Fe^{2+}/Fe^{3+} contributions.

4.3 Vibrational characterization

Non-destructive accessible techniques like FTIR and Raman spectroscopies have already been extensively used over the years to investigate the vibrational properties of phyllosilicate minerals in their bulk form [110, 121, 137–141]. However, it is extremely challenging to access the vibrational assignment of isolated FL-phyllosilicate flakes via far-field analysis [1]. Due to the low amount of material and the diffraction-limited size of these conventional techniques, the experiment sensitivity is mainly reduced and the vibrational response becomes dominated by the supporting substrate.

We measured the Raman spectrum of our clinochlore and phlogopite crystals in its bulk and exfoliated forms. Fig. 21 compares the Raman features of the bulk crystals with respect to the exfoliated flakes (thicknesses larger than 100 nm) onto different substrates (SiO_2/Si and Au/Si). We chose 638 nm laser excitation to avoid luminescence of the gold substrate at shorter wavelengths. However, clinochlore showed pronounced fluorescence at this excitation wavelength. Therefore, clinochlore was measured only using 473 nm laser for bulk and exfoliated flakes onto SiO_2/Si substrate.

We can identify the Raman peaks of our measurements for bulk clinochlore and phlogopite with the vibrational modes previously reported in the literature. The Raman spectrum of our bulk clinochlore sample which is shown in Fig. 21a (green curve) is in close agreement with the theoretically calculated spectrum [142]. The spectrum features 10 strong and well-defined modes. The peaks around 1089 and 1059 cm^{-1} are attributed to anti-symmetric Si-O-Si stretching modes, while the symmetric Si-O-Si stretching appears as strong bands at 687 and 553 cm^{-1}. The peaks at 459 and 440 cm^{-1} are probably assigned to librational OH and bending Si-O-Si modes. The strong band at 353 cm^{-1} has been assigned to the bending vibration of Si-O and its intensity decreases with the Si substitution by Al. The peak at 283 cm^{-1} is probably related to movements of the T sheet, whereas the sharp peak at 203 cm^{-1} was ascribed to vibrations of the octahedrons. Finally, the peak at 125 cm^{-1} is regarded as translational Si-O-Si modes. It is worth mentioning that the two other weaker peaks observed at around 106 and 158 cm^{-1} are

related to bending Si-O and to a combination of the out-of-plane vibration of the Mg ions with librations of the OH groups in the brucite-type interlayer, respectively [35, 55, 142]. As well as for clinochlore, the spectrum acquired for our bulk phlogopite (red curve in Fig. 21b) is close to the Raman-active fundamental modes theoretically predicted [140]. The spectrum shows two characteristic peaks at 197 and 683 cm^{-1} corresponding to the vibration of the MgO_6 octahedra and $(Si,Al)O_4$ tetrahedra, respectively, besides several other modes related to extra common modes for T layers (stretching and bending Si–O–Si vibrations) and translational (Mg,Al,Fe)-O vibrations in the Oc layers. Moreover, the position and shape of some Raman modes of phlogopite are strongly affected by changes in impurity concentration. For instance, the presence of Fe ions induces a peak splitting of the Si–O–Si vibrations (700-800 cm^{-1}) and the appearance of a strong peak in the 500-550 cm^{-1} range [30].

The Raman spectra measured for the exfoliated clinochlore and phlogopite flakes are unfortunately suppressed by the background contribution, especially for the SiO_2/Si substrate. This is a problem as this substrate has a higher contrast in OM and allows for easier mapping of ultrathin flakes and MLs. In the case of phlogopite, it was possible to observe a weak Raman signal for exfoliation onto Au substrates (gray curve in Fig. 21), despite the difficulty of evaluating the entire vibrational fingerprint of FL-phyllosilicates by conventional Raman spectroscopy.

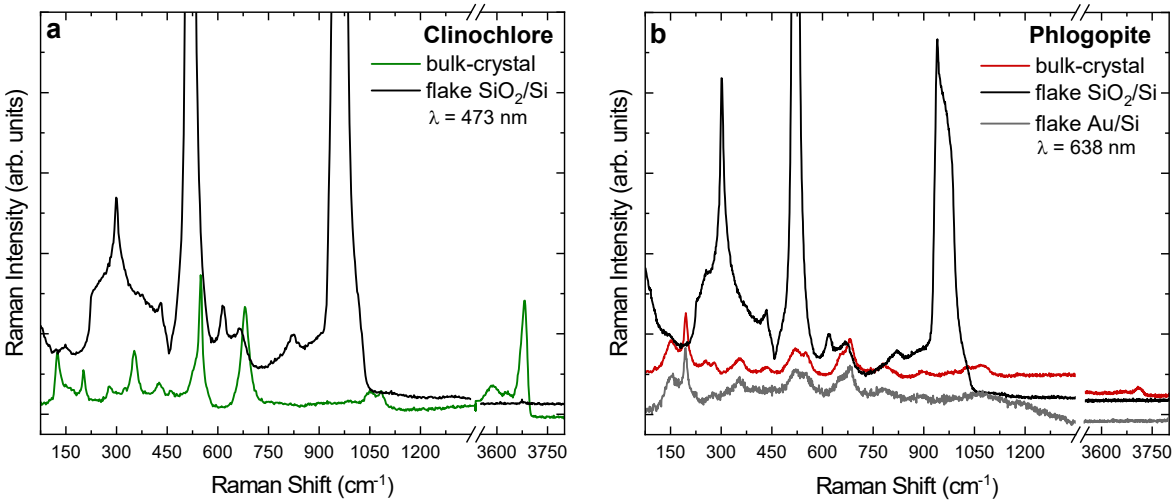

Figure 21 – Vibrational analysis of clinochlore and phlogopite by Raman spectroscopy. Raman spectra excited at 473 nm and 638 nm of the bulk-crystals (green and red curves) and exfoliated flakes onto SiO_2/Si (black curves) and Au/Si (gray curve) substrates of (a) clinochlore and (b) phlogopite.

Like Raman spectroscopy, standard micro-FTIR spectroscopy is a well-established technique in the study of natural crystals [102]. The micro-FTIR beam size using a conventional IR source can reach a lower limit of tens of micrometers and be further reduced to 3–5 µm using a synchrotron radiation source [102]. The use of synchrotron IR

radiation not only improves the spatial resolution of the technique but also allows the investigation of very low concentrations of chemical species due to minimal signal loss [103]. However, the spatial resolution of FTIR spectroscopy even using synchrotron radiation is optically limited by diffraction, which intrinsically scales with the radiation wavelength.

In this perspective, sub-diffractional analytical modalities based on near-field interactions are key tools for investigating micrometre-sized phyllosilicate flakes with a few nanometers thick. The SINS development, which combines a broadband synchrotron IR source with near-field optical microscopy, has overcome the diffraction limit of conventional optics to provide spatial resolution down to tens of nanometers in the study of atomic layered materials [143–146]. A unique feature of s-SNOM based techniques like SINS is its ability to measure complex scattering properties of the materials as detailed in section 3.2.2. Comparative studies using conventional and nano-FTIR techniques allow a direct association of FTIR absorption bands with the imaginary part (phase) of the SINS complex signal response [144]. In this way, SINS can be a decisive tool in the analysis of the infrared vibrational assignment of ultrathin phyllosilicates. We present in Fig. 22 SINS measurements on FL clinochlore and phlogopite flakes exfoliated onto Au/Si substrates to properly describe their vibrational modes at the nanoscale.

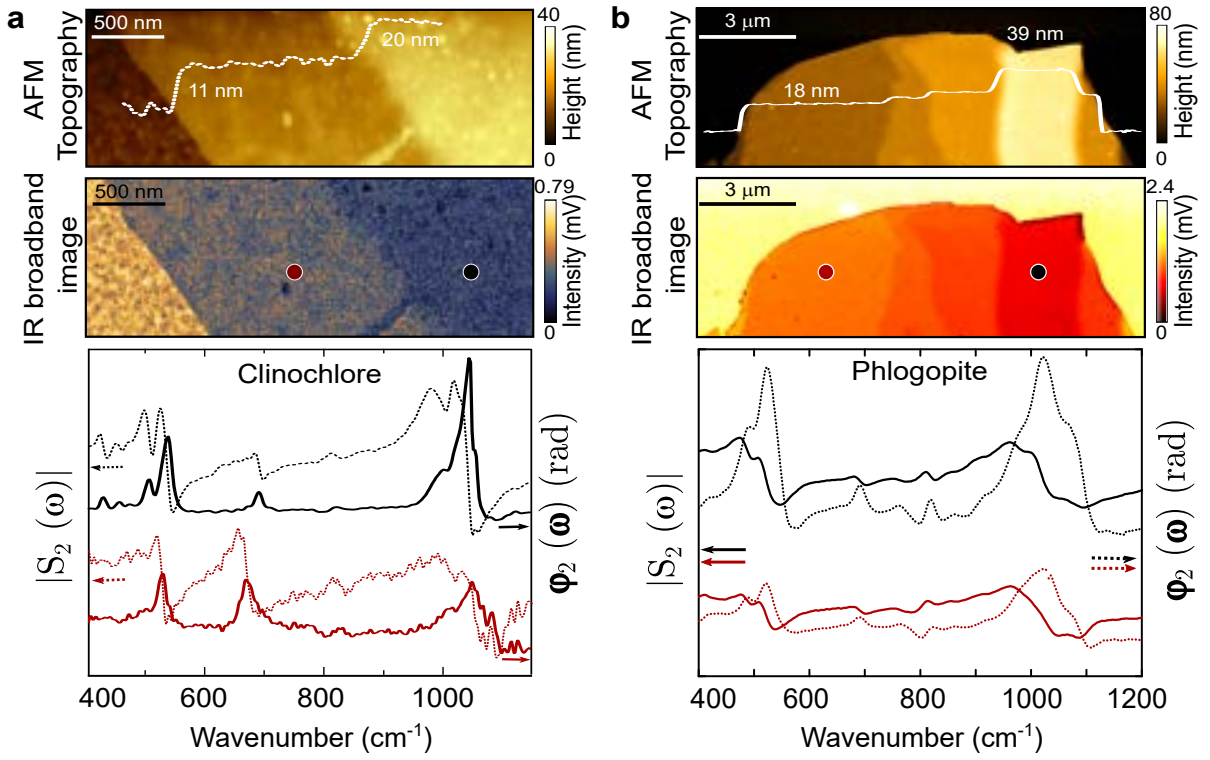

Figure 22 – Synchrotron infrared nanospectroscopy of clinochlore and phlogopite. Topography (top panel) and IR broadband images (center panel) of staircase-like exfoliated flakes of (a) clinochlore and (b) phlogopite onto Au/Si substrates in which SINS point spectra (bottom panel) were acquired at the red and black circles with different thicknesses. The continuous lines correspond to the amplitude $|S_2(\omega)|$ and the dashed lines correspond to the phase $\varphi_2(\omega)$ of the 2nd harmonic demodulation of SINS complex signals.

Phyllosilicate	Frequency (cm^{-1})	Assignment
Clinochlore	420	(Fe, Mg)-O-Si or Al-O-Si bending
	445	∥ Si–O bending
	470	metal-OH translation
	492	(Fe, Mg)-O-Si or Al-O-Si bending
	521	(Fe, Mg)-O-Si or Al-O-Si bending
	680	metal-OH libration
	811	Al–O stretching
	987	∥ Si–O stretching
	1023	∥ Si–O stretching
Phlogopite	472	∥ Si-O stretching
	508	∥ Si-O stretching
	682	Si-O-Mg stretching
	750	∥ Si/Al-O-Si stretching
	809	∥ Si/Al-O-Si stretching
	851	⊥ Si/Al-O stretching
	960	∥ Si-O stretching
	1001	∥ Si-O stretching
	1062	Si-O stretching

Table 5 – Summary of the IR-active vibrational modes of FL clinochlore and phlogopite probed by SINS. ∥ and ⊥ symbols indicate in-plane and out-of-plane vibrational modes, respectively.

Fig. 22a brings a high-resolution AFM topography image (top panel), together with the broadband near-field image (center panel) acquired with sharp optical reflectivity contrast for different numbers of stacked layers, as we can see in the AFM height profile. The bottom panel of Fig. 22a plots the SINS point spectra acquired at the red and black dot positions that correspond to 11 and 20 nm clinochlore thick regions, respectively. The measured SINS spectra unveil a strong IR activity in the frequency range from 400 to 1150 cm^{-1} that matches their micro-FTIR counterparts for bulk clinochlore [110, 137]. The Si–O in-plane stretching vibration bands have been observed at 1023 and 987 cm^{-1}, while the Si–O in-plane bending vibration has been observed at 445 cm^{-1}. Al–O stretching is associated with the weak band at 811 cm^{-1} and the two bands observed at 680 and 470 cm^{-1} are assigned to the metal-OH bond libration and translation, respectively. In the 400–550 cm^{-1} region, the IR spectra displayed three bands around 521, 492, and 420 cm^{-1}. These bands are assigned to (Fe,Mg)-O-Si or Al-O-Si bending modes [30].

Fig. 22b shows the topography and IR broadband image of a selected staircase-like phlogopite flake. We also compare the amplitude $|S_2(\omega)|$ and phase $\varphi_2(\omega)$ of the second harmonic point-spectra acquired at different phlogopite steps with 18 and 39 nm thicknesses. The spectra revealed well-resolved IR absorption bands for FL-phlogopite located approximately at 472, 508, 682, 750, 809, 851, 960, 1001 and 1062 cm^{-1}. The assessment of these IR absorption bands observed through SINS technique was done by comparing them with previous micro-FTIR literature for bulk phlogopite [121, 138–141].

The bands at 472 and 508 cm^{-1} correspond to Si-O vibrations, while the band at 682 cm^{-1} correspond to Si-O-Mg vibration. The bands at 750, 809, and 851 cm^{-1} are related to Al-O-Si stretching modes. The bands at 960, 1001 and 1062 cm^{-1} correspond to Si-O-Si in-plane stretching modes.

By comparing the SINS spectral features of FL clinochlore and phlogopite with their micro-FTIR vibrational modes reported in the literature for bulk crystals, we can conclude that phyllosilicates preserve their vibrational assignment when reduced down to a FLs. Moreover, they show a modulation of the intensity of vibrational modes according to the number of layers. This information is summarized in Table 5. However, it is important to point out that SINS can also acts as a directional probe by preferentially accessing vibrational modes oriented parallel to the electromagnetic mode of the strongly polarized near-field dipole at the SINS-tip. For phyllosilicates, this behavior was previously reported in the literature for talc [32, 63].

4.4 Discussions on the sample characterization

We start by discussing the structural and compositional aspects of clinochlore and phlogopite to elucidate which mineralogical phases and chemical variations could be present in the samples due to the fact that they are natural specimens from the geological environment of Minas Gerais - Brazil. We confirmed that the main crystalline phases of the samples are the expected phases of clinochlore and phlogopite, with a minor contribution of vermiculite (9%) and biotite (2%), respectively. We also observed a significant incorporation of iron and water in the minerals, about 7% and 6% of iron and 14% and 6% of OH/H_2O in clinochlore and phlogopite, respectively. The chemical analysis of the samples justifies the presence of minor phases in the structural analysis. Vermiculite is an direct alteration of clinochlore promoted by weathering processes in which the hydroxide layer is dehydroxylated or the Fe^{2+} ions are oxidized [147]. Biotite forms a solid-solution series with phlogopite with regard to iron content [141]. Therefore, it is expected that regions of higher iron incorporation in the phlogopite sample correspond to the biotite phase.

As we are interested in demonstrating phyllosilicates as suitable materials for nanotechnology applications, we exfoliated the samples to a FLs and performed a morphological analysis of the obtained flakes. Both clinochlore and phlogopite can be exfoliated down to a FLs presenting atomically flat surfaces over large areas, indicating that our samples have mandatory topographic characteristics to be embedded into vdWHs in the fabrication of nanodevices. However, if one intends to apply these phyllosilicates as an insulating substrate or encapsulating media, it is also necessary to probe the insulating character of the samples given by the value of their bandgap energy. We chose to evaluate

the insulating character of the samples optically. We observed an effective optical bandgap energy of 3.6 eV for both samples which is lower than the expected values for a pristine clinochlore or phlogopite samples [30, 35, 91], but still preserves their insulating character. We associate this reduction mainly to the incorporation of iron, which introduces a defect band in the middle of the bandgap of the materials [30, 35]. In this sense, for applications that require larger bandgap values, it would be necessary to perform leaching processes on the samples in order to remove iron impurities.

We also investigated the paramagnetic behavior of our samples, that arises from the incorporation of iron impurities, by the EPR technique, which is a powerful tool in the analysis of paramagnetic centers. We confirmed that Fe^{3+} is incorporated into both minerals at distorted octahedral sites. Performing a complementary analysis using the Mössbauer technique, we also demonstrated the presence of Fe^{3+} in tetrahedral sites in phlogopite and the presence of Fe^{2+} in octahedral sites in both samples. However, EPR and Mössbauer spectroscopy are volumetric techniques, and it is a challenge to use them to study phyllosilicates in their FL form. As an alternative, this thesis presents XRF and XANES techniques using synchrotron radiation as powerful tools for identifying and mapping impurities in FL phyllosilicates with nanometric resolution. A detailed analysis of the XANES spectra can also provide information about the local environment of the impurities, such as their oxidation state and coordination. With this, it was possible to probe the iron impurities in clinochlore and phlogopite in the FL form. In addition, we also observed trace impurities by XRF, such as Mn, which was only identified in the bulk clinochlore sample by EPR technique due to its high sensitivity to paramagnetic centers. It is important to emphasize that the analysis of impurities using synchrotron radiation presented in this thesis will be useful not only for characterization of impurities in phyllosilicates, but for 2D materials in general.

Finally, the use of synchrotron radiation is important not only to study the presence of impurity in phyllosilicates, but also to investigate their vibrational assignment. The presence of substitucional impurities change the vibrational modes of materials due to a relative difference in the bond lengths and effective mass. However, in the case of phyllosilicate minerals, it was demonstrated that is challenge to obtain the vibrational assignment of phyllosilicates in their FL form using conventional techniques like Raman of FTIR [1]. The reasons behind this are not clear, but certainly one of the reasons can be attributed to the low amount of material when they are in FL form. Using IR synchrotron radiation, this thesis present SINS technique based on near-field interactions as an alternative to overcome this issue. We obtained a broadband IR spectra of FL phyllosilicates, enabling the analysis of its vibrational modes. For Raman scattering analysis, tip-enhanced Raman spectroscopy could be an alternative route to explore phyllosilicate vibrational properties in future studies.

In future studies, it would also be interesting to carry out electrical measurements to directly obtain the charge mobility and dielectric breakdown of both minerals. Likewise, further measurements of magnetic susceptibility varying the temperature would also be interesting to perform in an attempt to stress out the magnetic properties of clinochlore and phlogopite that arise from iron impurities. With this, the applicability of these minerals in memory devices or as substrates that can present strong magnetic proximity effects with other 2D materials would be better pointed out.

This chapter was dedicated to analyzing the fundamental properties of clinochlore and phlogopite regarding the incorporation of impurities, presenting synchrotron techniques as robust solutions to study FL phyllosilicates. However, we also identified in our chemical analysis the incorporation of water in both minerals. The hydration properties of phyllosilicates in their FL form will be addressed separately in the next chapter.

5 Nanoconfinement of water in phyllosilicates

As discussed in section 1, phyllosilicates emerge as an abundant class of hydrous minerals with structural characteristics that act as natural nanocavities for water. They present the unique ability to absorb water by confining water molecules in the interlamellar space, being water-hybrid 2D systems of natural occurrence. However, besides its importance in several fields, the properties and behaviors of water under nanoconfined conditions are perplexing challenges for both theoretical and experimental understanding, which includes the hydration process of phyllosilicates. In the forefront of advancing our understanding of nanoconfined water in 2D systems, this section aims to elucidate how variations in the atomic structure of barely explored non-swelling phyllosilicate specimens - clinochlore and phlogopite - favors the geo-confinement of water during the mineral formation. We also discuss the environmental, thermal and mechanical stability of nanoconfined water in clinochlore (mainly) and phlogopite, suggesting the formation of 2D *ice-like* structures.

Early theoretical studies investigating the surface electrostatic potential of phyllosilicates consider each atom as a point charge [36, 37]. In this model, the talc structure corresponds to charge-neutral layer of a trioctahedral T-Oc-T phyllosilicate from which we can derive a potential that decays rapidly with distance from the mineral surface. An atomic substitution is considered a defect from which a distinct second potential of long-range interaction can be derived [37]. Phlogopite is a direct alteration of talc, in which one of the four Si^{4+} atoms in the tetrahedral layer is replaced by one Al^{3+} atom. This substitution in the T-layer changes the electronegativity of the substitutional site and localizes the negative charge on the basal O of the T-layer at the mineral surface, leading to stronger H-bonds of adsorbed H_2O molecules [37]. To recover the charge neutrality of this negatively charged structure, a cationic layer of K^+ atoms is formed between the T-Oc-T stacking. The arrangement of interlayer cations of pillared phyllosilicates such as phlogopite is determined by the atomic substitutions [78]. In micas, the hydration occurs by the formation of a cationic shell by water molecules with the hydrogens pointing towards the T-layers [148, 149]. The interlamellar water is expected to mediate the ionic diffusion in the highly confined space between the T-Oc-T stacking [79, 80]. Like phlogopite, clinochlore is also formed by T-layers with one Al substitution, but a further Al^{3+} substitution occurs in one of the three Mg^{2+} sites in the Oc-layer of the clinochlore T-Oc-T stacking. Atomic substitutions in the Oc-layer tend to localize the charge on the Al^{3+} site since Mg atomic orbitals have little tendency to interact with O orbitals to form chemical bonds [37]. Unlike talc and phlogopite, clinochlore presents an extra trioctahedral layer (*brucite-like*) formed purely by Mg as central atoms intercalating the T-Oc-T stacking. The interest in studying

the chlorite group lies in its complex structure with several atomic alterations that favor higher hydration compared to talc. Although these compounds are non-swelling specimens that contain a significant amount of water, little is known about how hydration occurs in chlorites.

Not discussing structural intercalation by water but surface hydration, a recent theoretical-experimental work investigating atomic-scale local hydration structures in clinochlore surface shows different ion adsorption behaviors on oppositely charged surfaces [6]. Regarding the water film formation on the surface of a cleaved mineral, another recent theoretical-experimental work shows that water films grow anisotropically driven by defects that capture water vapor at higher relative humidity (RH) environments (RH $>$ 30%) [76]. Both works reinforce the idea proposed by early theoretical studies [36, 37] that each atom acts as a point charge generating a surface electrostatic potential pattern that modulates how the water will interact with the phyllosilicate layer. Although the results of these most recent articles [6, 76] are limited to surface interactions, similar hydration processes may occur between clinochlore and phlogopite layers during the mineral formation and determine the confinement of water in them. Here, we intend to expand our understanding of phyllosilicate hydration beyond the water-mineral interface at the surface.

Water is a polar molecule with an electrical dipole moment associated [150]. The literature has demonstrated that the confinement of water by a 2D material can modify the overall electrical response of the material probed by electrostatic force microscopy (EFM) [151]. In this sense, EFM measurements can provide insights regarding the nanoconfinement of water between the layers of clinochlore. Within the EFM modes, the single-pass scan KPFM can acquire both topography and surface potential images simultaneously [95, 152]. Since the literature suggests that it is the surface electrostatic potential pattern in phyllosilicates that modulates the nanoconfinement of water, it would be interesting to probe the water in these minerals in its ultrathin form through the KPFM technique. Also, KPFM has already been demonstrated as a powerful tool to study mineral wettability [153]. The KPFM operation principle is based in minimizing the electrostatic interactions between the tip and the sample by applying an electric potential difference that corresponds to the local contact potential difference (CPD) [95, 97, 152]. The CPD contains local information about the surface potential and work function of the material.

Clinochlore measurements by KPFM technique have been reported in literature [83,154]. However, such experiments were performed at high RH environments (RH $>$ 30%). In high RH conditions, water films can grow on the mineral surface [77], leading to a misinterpretation of surface potential related to topography profiles. Here, we performed KPFM measurements on mechanically exfoliated clinochlore and phlogopite flakes onto a Si/SiO_2 substrate in a controlled humidity environment, avoiding surface adsorption effects on topography imaging. Fig. 23 shows selected clinochlore and phlogopite flakes observed

by optical microscopy (Fig. 23a and d, respectively) and its respective topography (Fig. 23b and e) and surface potential (Fig. 23c and f) acquired simultaneously by single-pass scan KPFM in a low RH environment (RH $< 0.5\%$) provided by a hermetic chamber with N_2 gas flux. For clinochlore, we can clearly observe that topography and surface potential images are not correlated. In fact, the surface potential reveals a striation pattern that reflects distinct electrostatic interactions between the tip and clinochlore flake which does not correspond to cleavage steps. For phlogopite, we did not observe the formation of capillaries in a striated pattern as in clinochlore. Only a higher diffuse surface potential and a few narrow channels are observed in thicker regions of the flake. The formation of capillaries in a striated pattern for clinochlore and the diffuse surface potential for phlogopite are reproducible behaviors for several flakes probed by KPFM.

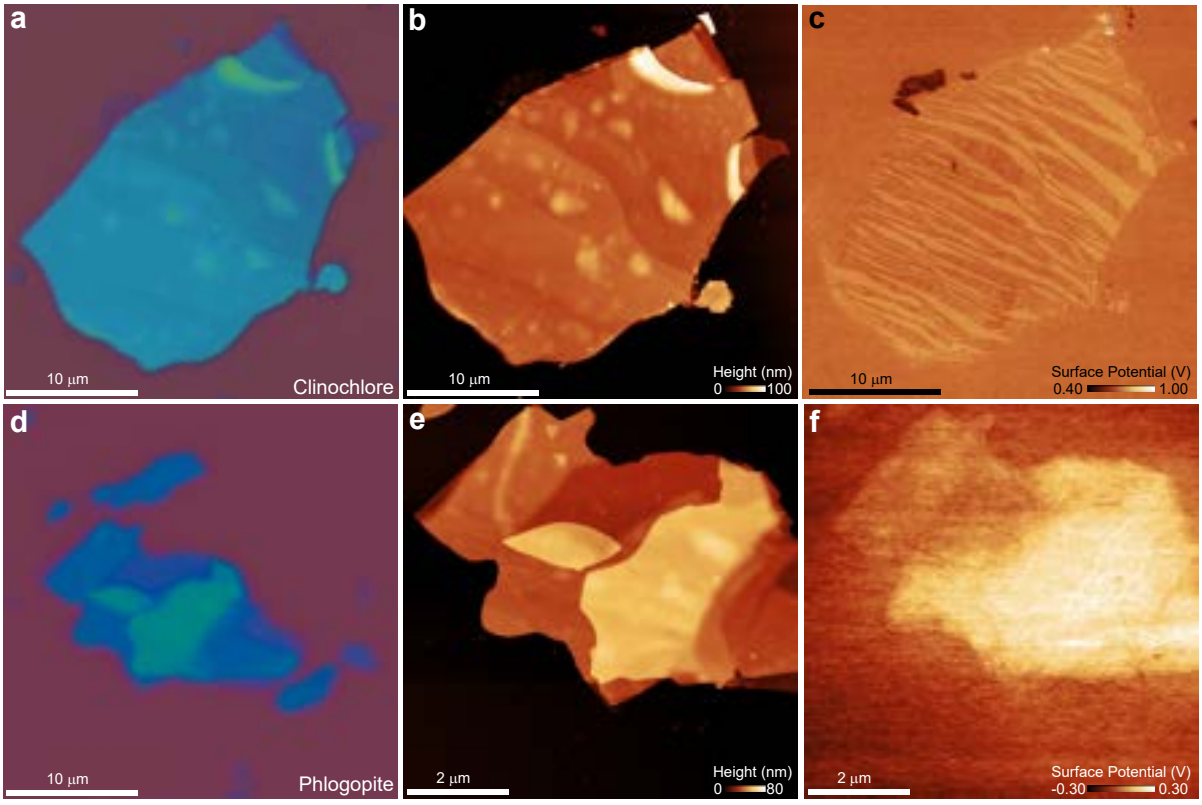

Figure 23 – Clinochlore and phlogopite surface potential. (a) Optical microscopy image of a clinochlore flake and its respective images of (b) topography and (c) surface potential acquired simultaneously by single-pass scan KPFM at $< 0.5\%$ RH. (d) Optical microscopy image of a phlogopite flake and its respective images of (e) topography and (f) surface potential acquired simultaneously by single-pass scan KPFM at $< 0.5\%$ RH.

We will focus on the formation of the well-defined capillaries in clinochlore as demonstrated in Fig. 23c to understand electrostatic interactions due to interlamellar water nanoconfinement that results in a striation pattern in the KPFM measurements. We can essentially model the tip-sample-substrate system as a capacitor in a KPFM measurement [97]. The CPD measured by the KPFM experiments corresponds to a local voltage applied between the tip and the back-electrode (grounded substrate), which act as

conductive plates of a capacitor, while the wide band gap insulating flake of clinochlore acts as the dielectric [97]. The surface potential striation pattern of clinochlore in Fig. 23c is composed of two regions, an A region (bright striations) that corresponds to a higher applied potential difference ΔV_A and a B region (dark striations) that corresponds to a lower applied potential difference ΔV_B. This indicates that the local capacitive system of region A has a smaller capacitance C_A than the capacitance C_B of region B, since the potential difference that must be applied between the plates of a capacitor is inversely proportional to the capacitance of the system to store the same amount of energy [155]. Thus, for a certain tip-sample distance, the difference between neighboring capacitive systems A and B of the same thickness consists of the difference in local dielectric properties.

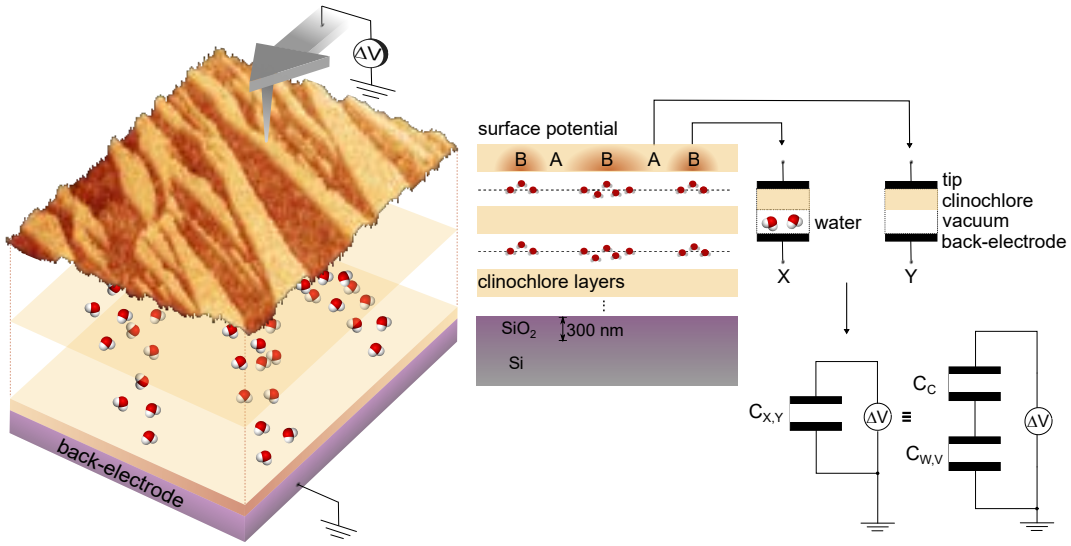

Figure 24 – Modeling the nanoconfinement of water in clinochlore according to its dielectric properties. The clinochlore flake measured by KPFM is depicted in in two different visualizations according to c-axis in which regions A and B of the striation pattern are specified. The right side shows the capacitive modeling of a system X and Y formed by the stacking of clinochlore layers intercalated and non-intercalated with water layers, respectively. The resulting capacitance of each system is a series association of individual capacitors formed only by clinochlore, water or vacuum as dielectric media.

We propose a simplified capacitive model to analyze the local dielectric properties of stacked clinochlore layers intercalated with water layers, depicted in Fig. 24. Atomic variations in the structure of clinochlore modulate the formation of interlamellar layers of water, which in turn form organized striated capillaries. Thus, variations may arise along the plane. These variations correspond to regions with water intercalating the clinochlore layers along the c-axis of stacking and other regions where there is no condensation of water molecules in the interlamellar space, consisting of empty spaces channels (or fulfilled with air). In terms of dielectric properties, the resulting capacitance of a capacitor formed by stacking two different dielectrics along the axis of the conducting plates corresponds to a series association of capacitors formed by each of the dielectrics individually [155]. Let us consider a system X as the stacking of clinochlore layers intercalated by layers

of water and a system Y where the stacking of clinochlore layers is intercalated by layers of air, which we will approximate by vacuum. The resulting capacitance C_X of the system X is $1/C_X = 1/C_C + 1/C_W$ and the resulting capacitance C_Y of the system Y is $1/C_Y = 1/C_C + 1/C_V$, where C_C, C_W, and C_V are the capacitance of individual capacitors formed by clinochlore, water, and vacuum as dielectrics, respectively. The capacitance is directly proportional to the dielectric constant of the dielectric material between the capacitor plates [155]. The dielectric constant of a material is defined as its electrical permittivity normalized by the permittivity of the vacuum. Typically, the dielectric constant of phyllosilicate minerals in its FL form lies between 2-10 [22, 53, 156], while the dielectric constant of water is around 80 (or 2 when nanoconfined [42]), such that these dielectric media are always more insulating than vacuum. This implies that $C_V < C_C$ or C_W, independent of exquisite properties of water in nanoconfined spaces that can significantly change its dielectric properties. On the other hand, mathematically $C_{X,Y}$ are necessarily inferior than the lower individual capacitance value of the association. So, $C_X < C_C$ or C_W as well as $C_Y < C_C$ or C_V. Consequently, $C_X > C_Y$, which implies in $\Delta V_Y > \Delta V_X$. Since $\Delta V_Y > \Delta V_X$ and $\Delta V_A > \Delta V_B$, our model leads us to associate the system Y with region A and the system X with region B. In other words, our model suggests that the dark striations in the surface potential striation pattern of clinochlore correspond to regions with the stacking of clinochlore layers intercalated with water layers along the c-axis, while the bright striations correspond to regions without formation of aqueous capillaries. Similar modeling can be used to understand the phlogopite surface potential probed by KPFM. Hydration of phlogopite occurs more diffusely without the formation of well-defined channels. This may be related to the fact that the hydration of micas occurs through the formation of a cationic water-shell that is, in principle, homogeneously distributed in the *ab* plane of the material. This may be the reason for the probed diffuse surface potential for phlogopite flakes. However, the dielectric response of the interlamellar water layer in micas with the presence of several cations needs to be considered carefully during the capacitive modeling in a more sophisticated approach, which is not the case for clinochlore.

The capacitive modeling for clinochlore requires the existence of nanoconfinement of water between the clinochlore layers with the formation of capillaries with the same striation pattern observed in the clinochlore surface potential image, such that hydrated capillaries correspond to the dark striations. Thus, the use of complementary imaging techniques that directly probes the water in 2D systems is mandatory. The fingerprint of water can be obtained by IR absorption since water molecule has three vibrational modes active in the IR range [49]. However, we are looking for a very small amount of water confined in a FL clinochlore flake about 50 nm thick and 30 μm wide. For this reason, we are not able to investigate this system by conventional micro-FTIR technique, in which we are limited by the diffraction limit. To access this information at the nanoscale, we can

perform chemical contrast imaging by IR s-SNOM to obtain the absorption pattern of clinochlore flake at specific frequencies. Our chemical contrast imaging must be performed at a characteristic vibrational mode of clinochlore and also of water molecule in order to observe an inversion of absorption behaviors to properly determine the clinochlore flake regions that confine water layers. We choose the most intense vibrational mode of FL clinochlore around 1050 cm^{-1} that corresponds to Si-O in plane stretching vibrations in the tetrahedral layer [35] to perform the clinochlore chemical contrast imaging. For the water contrast imaging, we choose the bending mode of water molecules around 1640 cm^{-1} in a spectral region without clinochlore vibrational modes that may overlap the water response. Fig. 25 shows the IR s-SNOM of the clinochlore flake. The topography image shown in Fig. 25a is similar to the topography images acquired by KPFM in a low humidity (LH) environment (Fig. 23b and 2b). This assures us that the s-SNOM measurements were carried out in a low adsorption regime, such that the main contribution of the absorption signal at the water bending frequency is from interlamellar water and not from water molecules possibly adsorbed on the flake surface.

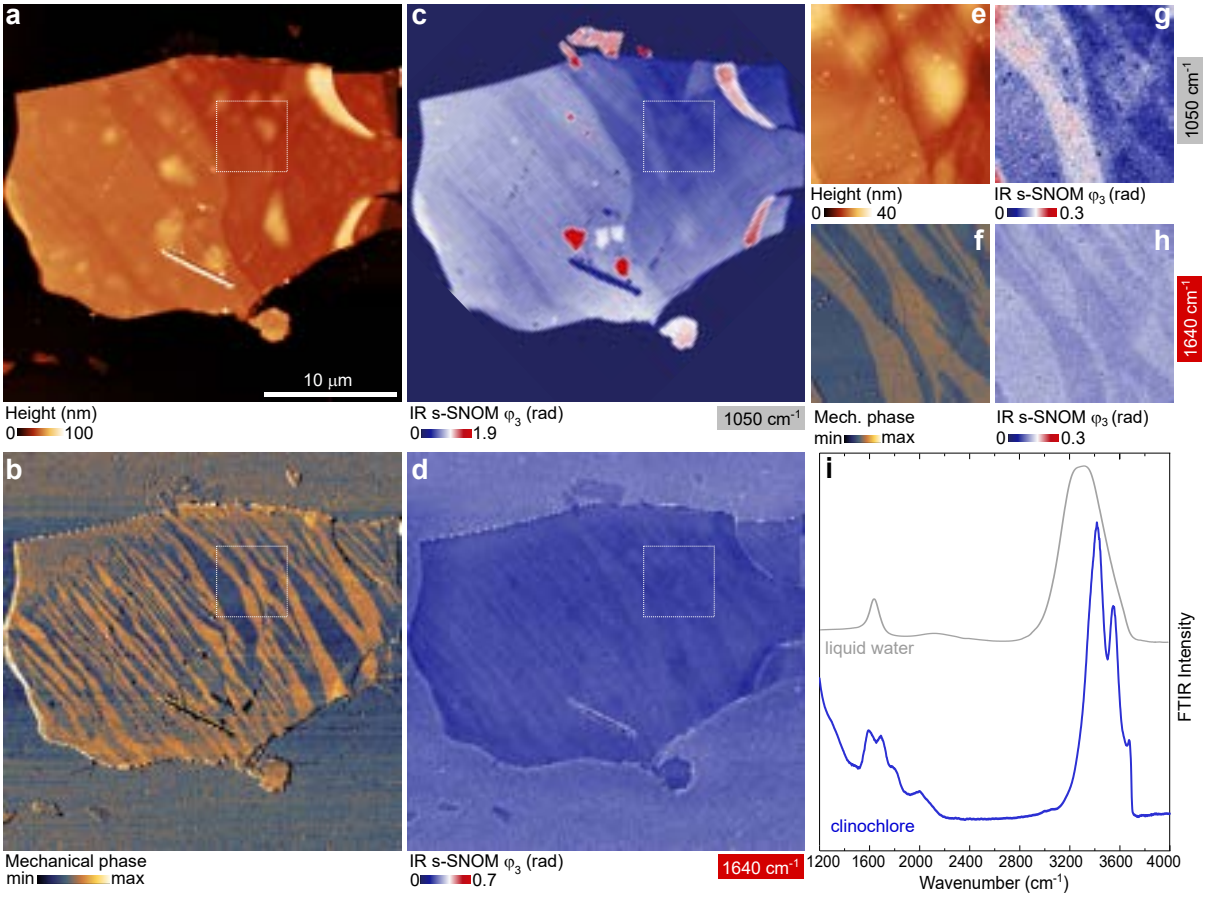

Figure 25 – Nanoconfinement of water in clinochlore. (a) Topography, (b) mechanical phase and IR s-SNOM 3rd-harmonic phase images acquired at (c) 1050 cm^{-1} and (d) 1640 cm^{-1} with their respective zoom images (e-h) from the region delimited by the white dashed square. (i) Micro-FTIR spectrum in the transmission mode of a bulk clinochlore sample (blue line) and a non-confined liquid water spectrum (grey line) for reference.

Simultaneously with the topography image, we can obtain the mechanical phase response of the material, which is related to its mechanical properties, corresponding to a convolution of changes in its composition, adhesion, friction, or viscoelasticity. The mechanical phase image of clinochlore shown in Fig. 25b reveals exactly the same striation pattern observed in the surface potential image (Fig. 23c). In general, large values of phase lags indicate that the material is locally less stiff and low phase angles correspond to materials with lower viscoelastic properties. Since our model indicates that the water confinement occurs at the dark striations in the surface potential image, and hence in the dark striations of the mechanical phase image, thus the nanoconfinement of water in clinochlore increases its local stiffness. It is well-know that water confined in nano-spaces can condensate and form distinct *ice-like* structures even at room temperature, including monolayer phases and a superionic phase with high electrical conductivity [39,41,43,51,157]. The literature reports an increase in stiffness when an integer number of water molecular layers are confined between a phyllosilicate surface and an AFM tip, suggesting a solid-like behavior for adsorbed water in this regime [38]. Other recent work reports the growth of 2D *ice-like* water on muscovite surface at high humidity (HH) by AFM [77]. They observed the formation of atomically flat water plateaus of about 0.4 nm that also appear darker in the phase image than the dry region of mica surface. We propose that the interlamellar water in phyllosilicate minerals behaves in the same way as water molecules adsorbed on their surface [77] forming *solid-like* water molecular layers. Thus, the increase in local stiffness of clinochlore flake seen in Fig. 25b may be associated with a *solid-like* ordered arrangement of water molecules confined between clinochlore layers.

The 3rd-harmonic demodulation of IR s-SNOM phase signal of the clinochlore flake at laser excitation frequencies 1050 and 1640 cm^{-1} are shown in figures Fig. 25c and Fig. 25d, respectively. We can observe three main features in Fig. 25c for the clinochlore chemical contrast image due to absorption associated with in-plane stretching of Si-O bonds in the tetrahedral layer around 1050 cm^{-1}. The first is that the absorption of the material is modulated according to the number of clinochlore layers, increasing as the flake gets thicker and, therefore, following the material topography. Second, it is possible to observe regions of high absorption. In particular, we can observe a thin flake uncoupled from the main flake that saturates the absorption and corresponds to a saturated dark region in the surface potential image (Fig. 23c). We suggest that this behavior occurs for thin dehydrated clinochlore flakes whose exposed surface is the negatively charged silicon tetrahedral layer due to atomic substitutions of clinochlore. Finally, it is also possible to observe that there is a superposition of a striation absorption pattern with the other features mentioned above. This striation pattern reproduces the surface potential pattern of Fig. 23c, such that regions of higher absorption (bright striations) in Fig. 25c correspond to regions of higher surface potential (bright striations) in Fig. 23c. This result is consistent with our proposal that regions of bright striations in the clinochlore surface potential

image (Fig. 23c) are associated with the stacking of clinochlore layers without water layers intercalation. Furthermore, the chemical contrast image of water measured by IR s-SNOM at 1640 cm^{-1} (Fig. 25d) reveals the exactly inverted striation pattern. At 1640 cm^{-1}, only the water bending vibrational mode is excited in our system. That is, the regions of higher absorption (bright striations) in Fig. 25d indicate the presence of water molecules confined in the clinochlore flake and those regions correspond to the dark striations in the surface potential image (Fig. 23c). This agrees with our model that associates the dark striations of clinochlore surface potential with the stacking of clinochlore layers intercalated by water layers. Figs. 25e-h show zoom images of topography, mechanical phase, IR absorption at 1050 cm^{-1} and 1640 cm^{-1}, respectively, from which we can observe details of morphology and mechanical properties of the clinochlore flake in comparison with the absorption striation pattern for the nanoconfined water in the material.

We also performed micro-FTIR measurements in transmittance mode on a clinochlore sample in its bulk form (blue line Fig. 25i). We compared the spectrum of clinochlore in the water absorption region (between 1200 and 4000 cm^{-1}) with the expected spectrum of "free" water in liquid form (gray line). We can observe that the absorption spectrum of liquid water presents an absorption band at around 1640 cm^{-1} that corresponds to the bending mode of water molecules and another band at around 3400 cm^{-1} that corresponds to a convolution of the symmetric and antisymmetric stretching modes. We also observe a broad band around 2000 cm^{-1} due to overtone of bending and librational modes (low-frequency modes below 1000 cm^{-1} that arises from intermolecular interactions and most closely reflects the water structure [158]). However, the confinement of water molecules in the clinochlore as interlamellar water or through hydroxyl groups incorporated in its atomic structure changes the water IR absorption to a *solid-like* spectrum, shifting and splitting the absorption bands. We can observe that the bending mode splits into three main bands around 1590, 1695 and 1805 cm^{-1}. In the case of bending motions, ice is known to have a broader spectrum than liquid water due to the distribution of its ordered hydrogen bonding environment, while liquid water possess a weaker hydrogen bonding environment, and therefore a narrower band at around 1640 cm^{-1} [159]. In the spectral region for stretching modes of OH groups, the absorption band for clinochlore shifts towards high-frequencies and splits into three bands around 3415, 3550 and 3675 cm^{-1}. Higher overall frequencies are related to more restricted vibrational motions [160], which implies more hydrogen bonds for water nanoconfined in clinochlore than for free water. In fact, under high pressure conditions, a recent theoretical work suggests the formation of an *ice-like* hexagonal closest-packing water monolayer stably intercalated in phyllosilicates [51]. The simulations indicated significantly low diffusion coefficients for water intercalated in T-Oc-T trioctahedral phyllosilicates that correspond to water molecules with a higher order of hydrogen bonding, causing it to be trapped in the same site for long periods. This result reinforces the possibility that water molecules confined in

clinochlore may form a 2D *ice-like* ordered arrangement in the interlamellar space.

5.1 Environment stability

The hermetic chamber with N_2 gas flux in which the microscope is placed during measurements enables the acquisition of topography and surface potential images by KPFM in RH controlled environment. We performed KPFM measurements shown in Fig. 26 in LH ($< 0.5\%$ RH) and HH environments ($> 30\%$ RH) for clinochlore and phlogopite. For clinochlore (Figs. 26a-d), we observe the preservation of the same features for both surface potential images acquired in LH and HH environment, noting only a reduction in the overall relative surface potential voltage range. However, we notice that the topography acquired in the HH environment presents a superposition with the striation pattern revealed by the surface potential image. This superposition indicates that the adsorption in the HH environment is the result of surface electrostatic interactions, replicating a higher adsorption on the regions where the surface potential is higher. This behavior will be further explored later. For phlogopite (Figs. 26e-h), the topography images remain reproducible in both LH and HH environments. This reproducibility indicates that the adsorption on the phlogopite surface occurs homogeneously. However, the surface potential changes dramatically. It is important to emphasize that the surface potential probed by KPFM is a relative measure and generates a relative contrast. In LH, adsorption is almost completely avoided, so the surface potential image contrast is due only to dielectric differences in the flake itself. Since there is no formation of well-defined aqueous channels in phlogopite and its hydration occurs in smaller amounts and homogeneously (following the literature results that suggest the formation of a cationic shell by water molecules [148]), the potential contrast surface of phlogopite can reveal other dielectric differences. We can observe that, in the case of this flake, the higher surface potential signals correspond to a diffuse pattern superposed with the bubble regions, which result in a dielectric difference because they are most filled with air. Bubbles are common among exfoliated phyllosilicates and may be related to the mechanical exfoliation process. They have heights of up to tens of nanometers with diameters that reach micrometric sizes, while the lateral size of the capillary channels is in the order of hundreds of nanometers, reaching micrometers only for the wider channels. The bubbles are not filled mostly by water because they do not result in high absorption at the water bending mode frequency shown in Fig. 25d for clinochlore. The lack of absorption contrast for the bubbles suggests that, even though the bubbles may have some water content in their interior, the hydrophilic character of the bubbles is lower than in the regions where water condenses forming capillaries, In turn, capillary regions may be related to the high hydrophilic character of surfaces that expose tetrahedral layers [37]. In HH, the interpretation that surface adsorption in phlogopite occurs following the flake hydration by water intercalation remains consistent. A homogeneous contrast

between the surface of the phlogopite flake and the substrate is observed, indicating a homogeneous adsorption on the entire surface of the flake, different from the adsorption that occurs on the substrate. This is expected because the negative charge of the T-layer at the mineral surface leads to stronger H-bonds of adsorbed H_2O molecules [37]. This adsorption behavior of phlogopite reduces its local surface potential similarly to that described in the capacitive model for clinochlore to explain the dark striations.

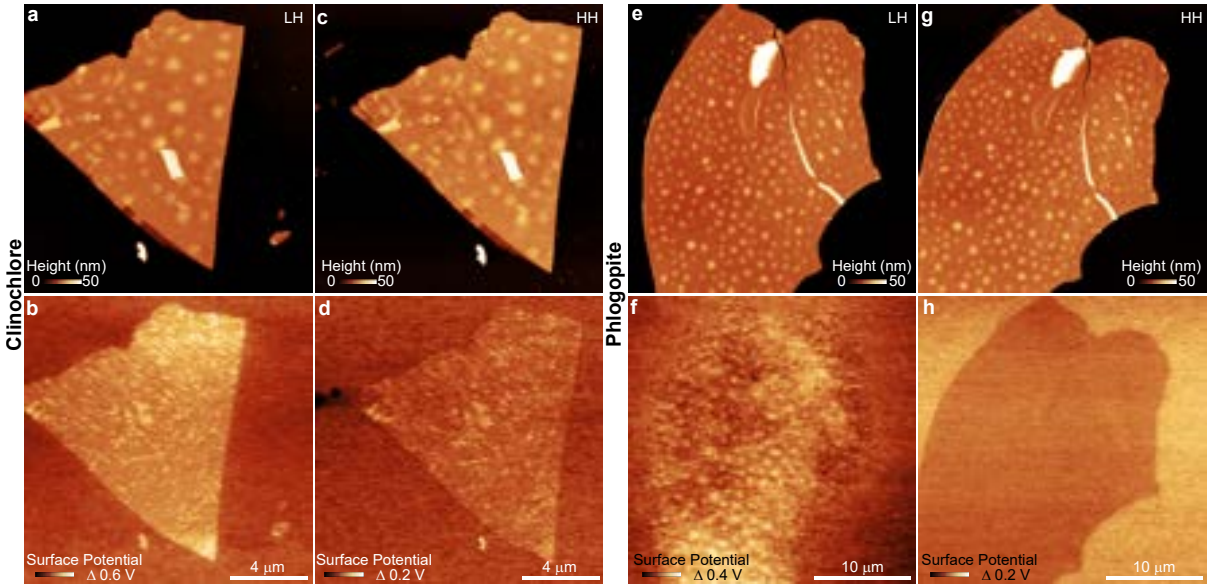

Figure 26 – Influence of environment RH on topography and surface potential of clinochlore and phlogopite probed by KPFM. (a) Topography and (b) surface potential images of a clinochlore flake exfoliated onto a Si/SiO_2 (300 nm) substrate in a LH ($< 0.5\%$ RH) and (c) and (d) in HH environment ($> 30\%$ RH), respectively. (e) Topography and (f) surface potential images of a phlogopite flake also exfoliated onto a Si/SiO_2 (300 nm) substrate in a LH ($< 0.5\%$ RH) and (g) and (h) in HH environment ($> 30\%$ RH), respectively.

We will further stress the adsorption behavior of ions and water molecules on the clinochlore surface to understand in detail the replication of the surface potential in the topography image. Fig. 27a shows the topography image of a clinochlore flake measured by KPFM as freshly exfoliated in a HH environment. The striation pattern observed in Fig. 23c is superimposed with the topography features. A subsequent topography image was acquired by KPFM in LH environment after 3 hours in N_2 gas flux atmosphere (Fig. 27b). We can observe the correct clinochlore topography, without the superposition of the striation pattern due to adsorption effects. Increasing again the environment RH by leaving the hermetic chamber open for 30 minutes without N_2 flux, the striation pattern is reproduced again in the topography image (Fig. 27c). This procedure indicates that the correct topography of clinochlore needs to be acquired in LH environments to avoid adsorption effects. Furthermore, we can observe that adsorption at clinochlore surface is not a homogeneous effect, but it is driven by electrostatic interactions. The growth of water films and ionic adsorption at clinochlore surface is modulated by its surface potential.

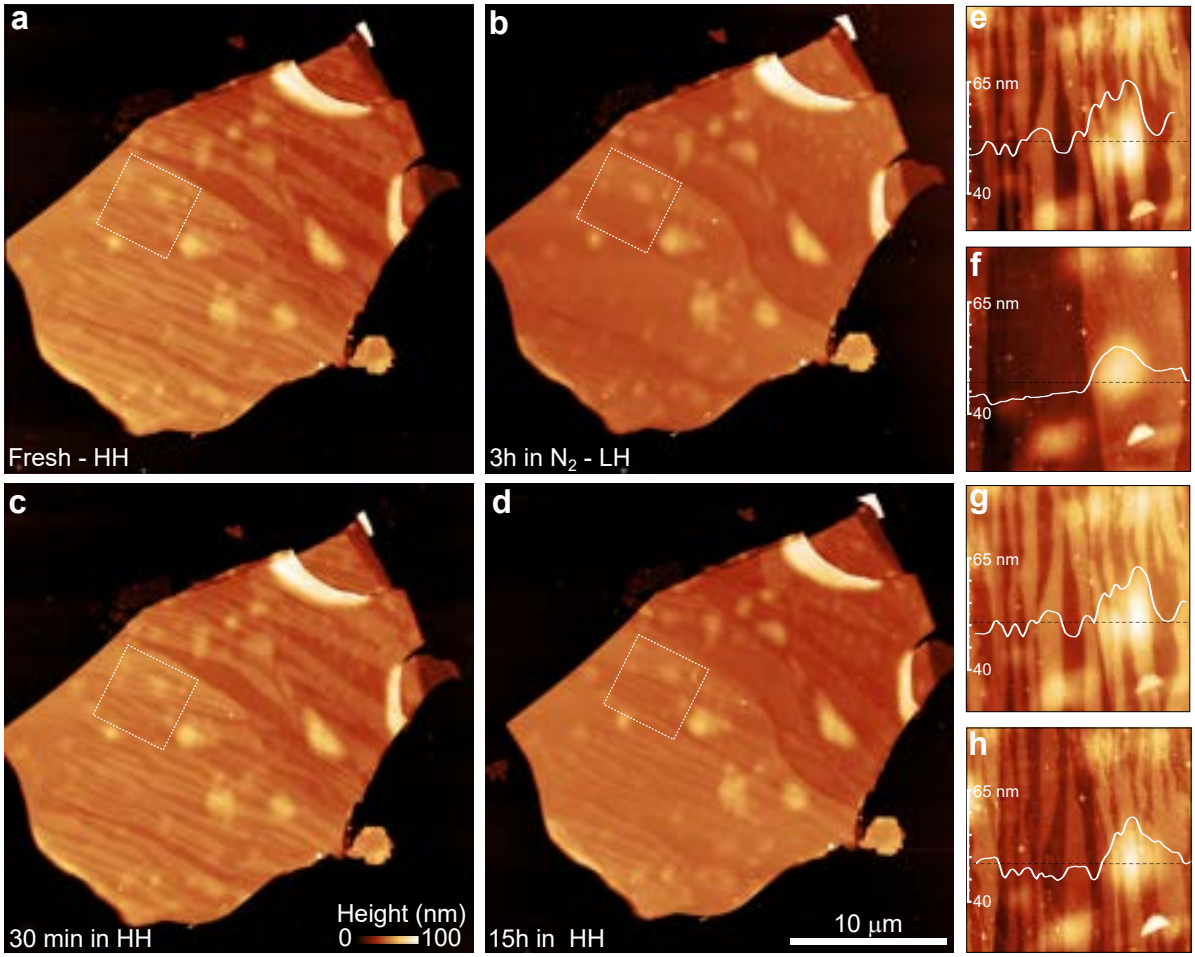

Figure 27 – Influence of RH on clinochlore topography. Topography images of a clinochlore flake (a) freshly exfoliated onto a Si/SiO_2 (300 nm) substrate in a HH environment ($> 30\%$ RH) and (b) after 3h in LH environment ($< 0.5\%$ RH) with N_2 gas flow. Sequentially, the flake was left in a HH environment. The topography images were acquired after (c) 30 min and (d) 15h of exposure, revealing two different adsorption regimes. The height profiles shown in (e-h) were extracted along the dashed black line at each topography zoom rotated 63 degrees clockwise of the region delimited by the white dashed square in (a-d) respectively.

We can also observe a second surface hydration state by maintaining the clinochlore flake in a HH environment for 15 hours (Fig. 27d). In this second hydration regime, the adsorption stabilizes in an inverted striation pattern – the higher adsorption in the second regime occurs where the low adsorption occurs in the first hydration regime of Fig. 27a and Fig. 27c. In fact, the behavior of two-phase adsorption regimes of water on phyllosilicates as a function of RH and environment exposure time has already been reported for mica surfaces [161, 162]. In micas, the formation of 2D adsorption islands occurs with geometrical shapes in angular epitaxial relation with the underlaying mica lattice [77, 161, 162], suggesting a solid character. It is particularly interesting to point out that this epitaxial condensation of water molecules at mica-interface exhibits low dielectric constant [161, 162], since water has an anomalously low dielectric constant

when nanoconfined [42] and may also form *ice-like* structures [43–45]. The details of adsorption effects on clinochlore topography for each case can be observed by the height profile extracted in the same line position from each topography image (Figs. 27e-h). It is important to note that the KPFM surface potential images acquired simultaneously with topography images shown in Fig. 27 did not change during all processes. This indicates that the variations in RH can only favor interactions of adsorption at the clinochlore surface, not affecting the arrangement and amount of water confined in the mineral.

5.2 Thermal stability

In order to study the thermal stability of nanoconfined water in clinochlore and phlogopite, thermal treatments were carried out using a hot plate in ambient conditions. All KPFM measurements presented in this section were performed in LH environment. First, the clinochlore and phlogopite flakes were exfoliated onto a Si/SiO_2 (300 nm) substrate. The corresponding topography and surface potential images were acquired by KPFM. Both samples were then submitted to annealing at 150℃ for 3h. After the annealing, the topography and surface potential images were again acquired by KPFM. A second annealing at 300℃ for 3h was sequentially performed and the respective topography and surface potential images were also acquired by KPFM. Thermal treatments at higher temperatures were not performed to avoid the dehydroxylation that starts to occur around 500℃ in phyllosilicates [163]. Keeping the annealing temperature below 500℃ ensures that the treatment is only accessing the interlamellar water, not OH groups of octahedral layers.

Fig. 28 shows the topography and surface potential images of clinochlore acquired before and after the two sequential annealings. After the first annealing, we can observe that the clinochlore flake starts to recrystallize due to the disappearance of the folds in the topography image, despite the appearance of small bubbles. However, the surface potential becomes diffused due to the melting of the aqueous channels. After the second annealing, the clinochlore topography is much flatter, without wrinkles and with less relief of bubbles. The surface potential contrast begins to invert, as the interlamellar water is being removed from the flake.

The annealing effects on phlogopite were similar to those of clinochlore. Fig. 29 shows the topography and surface potential images of phlogopite acquired before and after the two sequential annealings. After the first annealing, we can also observe a recrystallization of the phlogopite flake by the topography image that becomes more effective after the second annealing. As in clinochlore, the surface potential of phlogopite also becomes diffuse as compared to the substrate after the first treatment, which begins to invert after the second treatment. It is interesting to note that, for both phlogopite and

clinochlore, the inversion process of the surface potential contrast occurs from the flake edges towards the interior. This behavior suggests that the innermost interlamellar water evaporates with more difficulty than water closer to the edges.

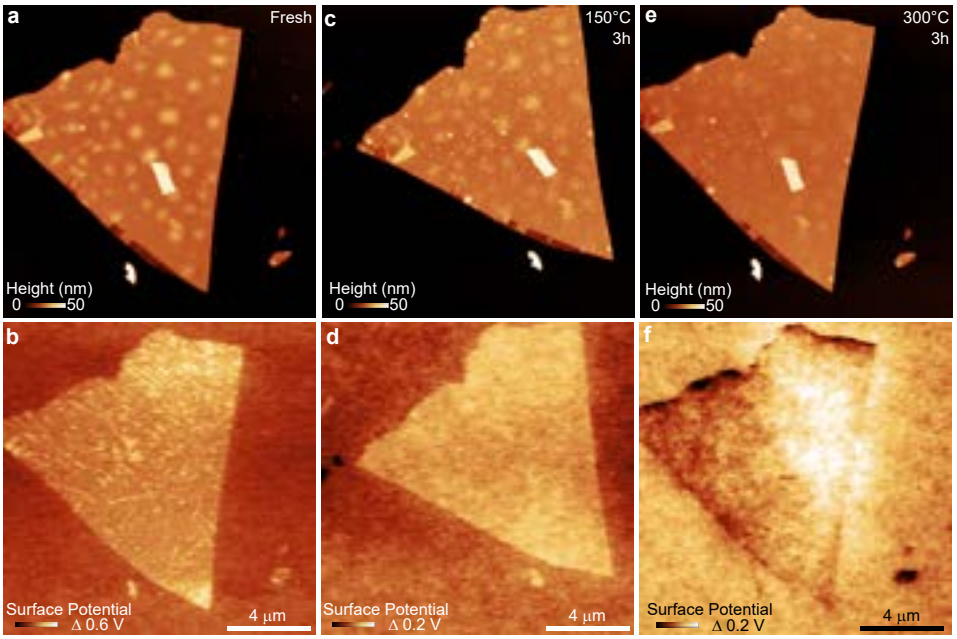

Figure 28 – Thermal stability of nanoconfined water in clinochlore. (a) Topography and (b) surface potential images of a clinochlore flake freshly exfoliated onto a Si/SiO_2 (300 nm) substrate in a LH environment (< 0.5% RH). (c,e) Topography and (d,f) surface potential images of the same flake after 3h of annealing at 150°C and 300°C, respectively.

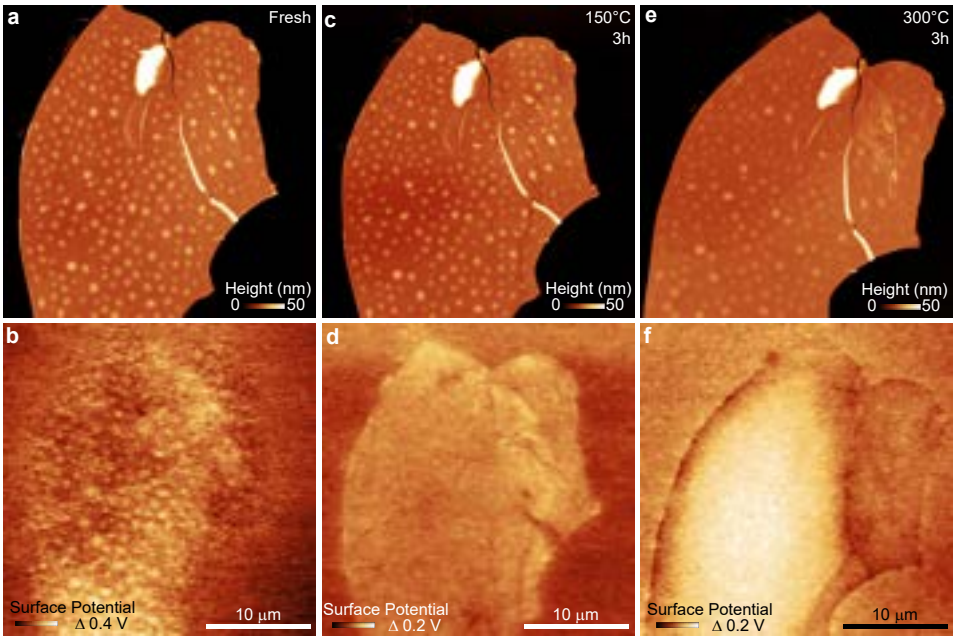

Figure 29 – Thermal stability of nanoconfined water in phlogopite. (a) Topography and (b) surface potential images of a phlogopite flake freshly exfoliated onto a Si/SiO_2 (300 nm) substrate in a LH environment (< 0.5% RH). (c,e) Topography and (d,f) surface potential images of the same flake after 3h of annealing at 150°C and 300°C, respectively.

In summary, the nanoconfined water in clinochlore and phlogopite is not stable to the increase in temperature of the flake. Since nanoconfined water determines the fundamental properties of these systems, such as dielectric and mechanical properties, thermal treatments act as a simple route capable of modifying such properties. Heat treatments also proved to be excellent in making the topography of the flakesmore uniform.

5.3 Hydration

Since interlamellar water can be removed by thermal treatments, it is important to understand whether the mineral can be rehydrated and how this process occurs. The focus of this section will be on the particular case of clinochlore in order to understand the formation of aqueous channels in a striation pattern. Assuming that it is the distribution of electrostatic charge in each layer that modulates how water will confine in the interlamellar space of clinochlore, it is expected that the rehydration process will occur following the capillary pattern before dehydration. However, the annealing process used to remove the interlamellar water also gives thermal mobility to the substitutional atoms and, consequently, it can modify the electrostatic charge distribution locally. For this reason, a complete reproduction of the aqueous capillaries in the rehydration process is not expected.

Three rehydration processes will be presented. In all of them, thermal treatments were first performed to melt the interlamellar water in clinochlore and, eventually, evaporate it. Then, the samples were submitted to rehydration processes by immersion in water under different conditions. All KPFM measurements presented in this section were performed in LH environment.

Fig. 30 shows a sequence of four KPFM measurements starting from a fresh exfoliated flake in which two annealing processes were performed at 150℃, one for 1h and the second for 3h. We can observe in the surface potential images that maintaining the temperature and varying the annealing time is also an effective route to melt the aqueous channels and start the evaporation of the interlamellar water. This is revealed by the inversion of contrast in the surface potential images after the second treatment. After that, the flake was rehydrated. This first hydration process consisted of immersing the sample in successive water droplets of 0.5, 1, and 5 μL. The drying process of each droplet lasted a few minutes (less than 3 minutes) and was carried out with the sample heated to 150℃ in ambient atmosphere. Impressively, after the hydration procedure, the surface potential image clearly reveals the formation of capillaries that follow the same contrast and striated pattern as the fresh exfoliated flake. This is a clear demonstration that the clinochlore acts as a natural nanocavity for water confinement in 2D systems, allowing both dehydration and rehydration of its capillaries. In addition, this behavior reinforces the theoretical model that the atomic structure of the material itself determines how the

confinement of interlamellar water will occur. From the topography images, we did not observe significant changes beyond the expected uniformity of the flake surface by thermal treatments. The flake also maintained its thickness (about 43 nm).

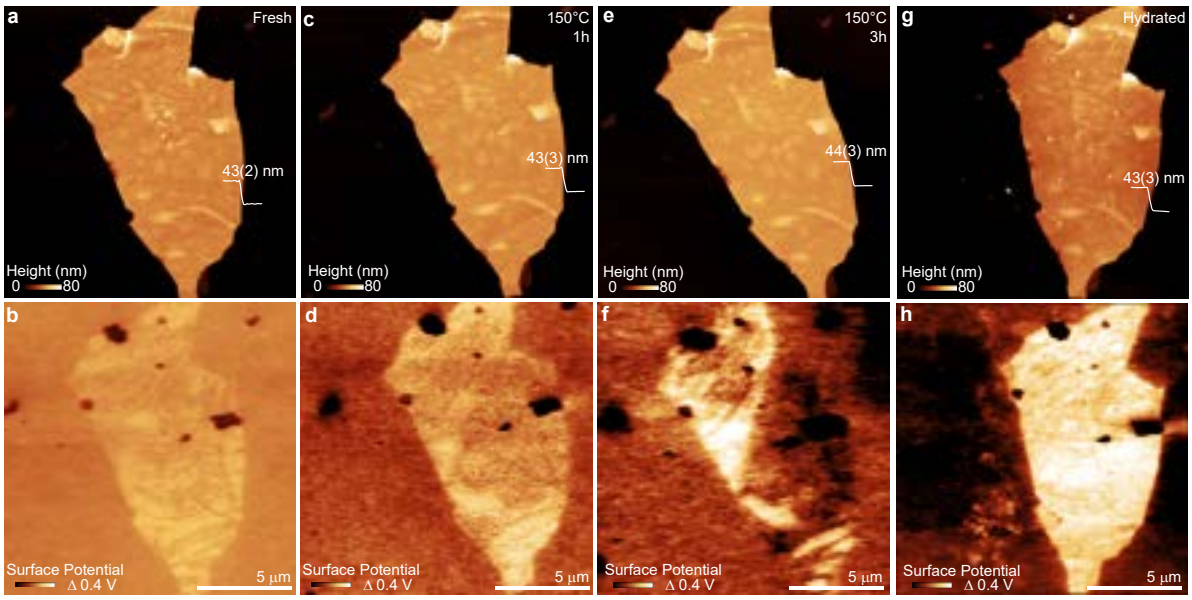

Figure 30 – Rehydration process of clinochlore by immersion of heated sample in water droplets. (a) Topography and (b) surface potential images of a clinochlore flake freshly exfoliated onto a Si/SiO_2 (300 nm) substrate in a LH environment (< 0.5% RH). (c,e) Topography and (d,f) surface potential images of the same flake after 1h and 3h of annealing at 150°C, respectively. (g) Topography and (h) surface potential images of the same flake after the rehydration process by immersion in water droplets of 0.5, 1 and 5μL that dried fast by heating the sample to 150°C.

To the second rehydration process depicted in the KPFM measurements of Fig. 31, an annealing was first performed at 150°C for 1h30. Then, the sample was immersed in two successive water droplets of 10 μL. The water droplets were left to evaporate naturally with the sample kept at room temperature but in a N_2 atmosphere. From the surface potential images, we can observe a contrast inversion after the annealing. However, after the hydration process, we observed the formation of clusters and not the formation of well-defined capillaries following the striation pattern of fresh exfoliated flake. We also observed that the flake topography did not change during the procedure.

The third rehydration process was performed in order to stress the thermal treatments parameters and hydration conditions. After an annealing at 350°C for 5h, the clinochlore was immersed in 1.5 mL of liquid water at 150°C which completely evaporated in 30-40 minutes at ambient conditions. Fig. 32 shows the topography and surface potential images acquired for the fresh exfoliated flake, after the annealing and after the third hydration process. Although the topography remains the same at each step of the procedure, the surface potential changes significantly. After annealing, the flake appears to be completely dry, presenting a dark contrast to the substrate. After the hydration

procedure, the flake recovers its higher diffuse surface potential contrast in relation to the substrate, in addition to presenting a partial formation of capillaries in the same direction as those of the fresh exfoliated flake.

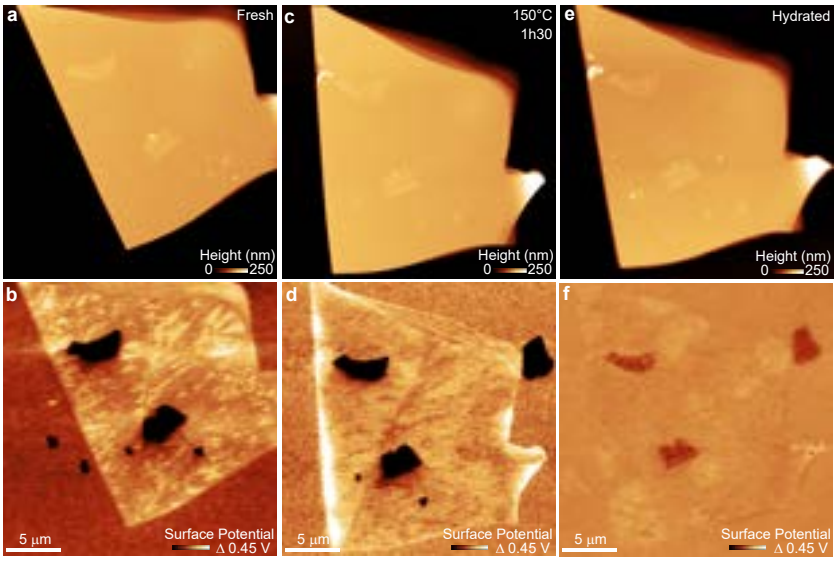

Figure 31 – Rehydration process of clinochlore by immersion in water droplets at room temperature and N_2 atmosphere. (a) Topography and (b) surface potential images of a clinochlore flake freshly exfoliated onto a Si/SiO_2 (300 nm) substrate in a LH environment ($< 0.5\%$ RH). (c) Topography and (d) surface potential images of the same flake after 1h30 of annealing at 150℃. (e) Topography and (f) surface potential images of the same flake after the rehydration process by immersion in water droplets of 10μL that dried naturally by keeping the sample at room temperature in N_2 atmosphere.

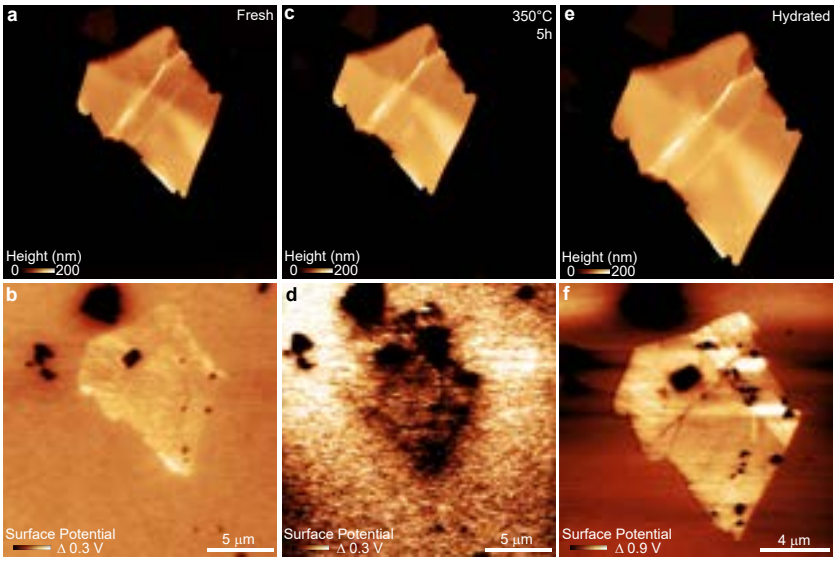

Figure 32 – Rehydration process of clinochlore by immersion in 1.5 mL of liquid water at 150℃. (a) Topography and (b) surface potential images of a clinochlore flake freshly exfoliated onto a Si/SiO_2 (300 nm) substrate in a LH environment ($< 0.5\%$ RH). (c) Topography and (d) surface potential images of the same flake after 5h of annealing at 350℃. (e) Topography and (f) surface potential images of the same flake after the rehydration process by immersion in 1.5 mL of liquid water at 150℃ which evaporated in approximately 30 minutes.

The seminal results of this thesis indicate that the most promising way to rehydrate the clinochlore with the formation of aqueous channels is by sequentially combining temperature and water action in ambient atmosphere, avoiding extreme parameters and conditions. It is noteworthy that this procedure somewhat mimics the geological environment in which the phyllosilicates are formed by hydrothermal alterations, which may explain why this route seems to be the most appropriate.

5.4 Mechanical stability

We demonstrated that the interlamellar water in non-swelling phyllosilicates, in particular in clinochlore, is stable to variations in environmental RH, but can be accessed through thermal treatments. Furthermore, it was shown that it is possible to rehydrate clinochlore with the reproduction of its aqueous channels. However, the methods applied so far to manipulate the interlamellar water are not able to act only in a specific region of interest of the sample. To achieve a controlled local manipulation of the confined water at nanoscale, AFM in contact mode was used to mechanically manipulate a small region of interest by applying pressure. The idea is to squeeze out the interlamellar water from the scanned area under application of force with the AFM-tip to press one layer against the other subsequent layer. This section describes and discusses the experiments of mechanical nanomanipulation of interlamelar water in clinochlore at LH depicted in Fig. 33.

First, the topography and surface potential images (Figs. 33a,b) of a specific region of a fresh exfoliated clinochlore flake were acquired by single-scan KPFM. A delimited area by the white square of 2 x 2 μm^2 was chosen to perform an AFM scanning in contact mode with application of 1 μN of force. After this first step of mechanical nanomanipulation, the topography and surface potential of the same region was acquired by KPFM (Figs. 33c,d). It was observed from the surface potential images that only the aqueous channels at the bottom edges of the manipulated area were drained. The application of force below 1 μN was not able to drain the aqueous channels in this area. A second step of nanomanipulation was performed with the application of 1.5 μN of force in the same area. Again, the topography and surface potential images (Fig. 33e,f) were acquired by KPFM. From the surface potential images, it was observed that practically all aqueous channels in the nanomanipulation area were drained. The mechanical nanomanipulation method demonstrated here is capable of successfully draining aqueous channels of up to hundreds of nanometers (about 400 nm) in flakes with thicknesses of up to 20 nm by applying 1.5 μN of force. Larger channels are more difficult to be nanomanipulated by this method, as well as thicker flake regions. Forces above 2 μN were unfeasible to explore because they required extra adjustments in the AFM detection system. Extra adjustments would make the nanomanipulation method more complex and less accessible, which is not the intention. Recently, a molecular dynamics simulation study revealed an outflow

behavior for confined water in a silica nanotube similar to that of solid metal nanowires under uniaxial tension [164]. They associated this aqueous *solid-like* extrusion behavior to the strong cohesion of water molecules, with hydrogen-bonding networks and dipole alignments. The results presented in this thesis also suggest a *solid-like* behavior or large viscosity for water nanoconfined in clinochlore. Thus, it is possible that the outflow of nanoconfined water in clinochlore during the mechanical nanomanipulation experiments is similar to that of a solid or a fluid with large viscosity.

It is important to emphasize that the contact mode scan modified the clinochlore surface potential, but did not change the topography features of the analyzed area, as we can observe in the topography images. The only noticeable change in the topography images is a small accumulation of material on the edges of the nanomanipulation area that follows the scanning direction (from left to right, top to bottom), which does not result in a new contrast in the surface potential image. This is due to the fact that the surface of the clinochlore flake is inevitably polished during contact scanning.

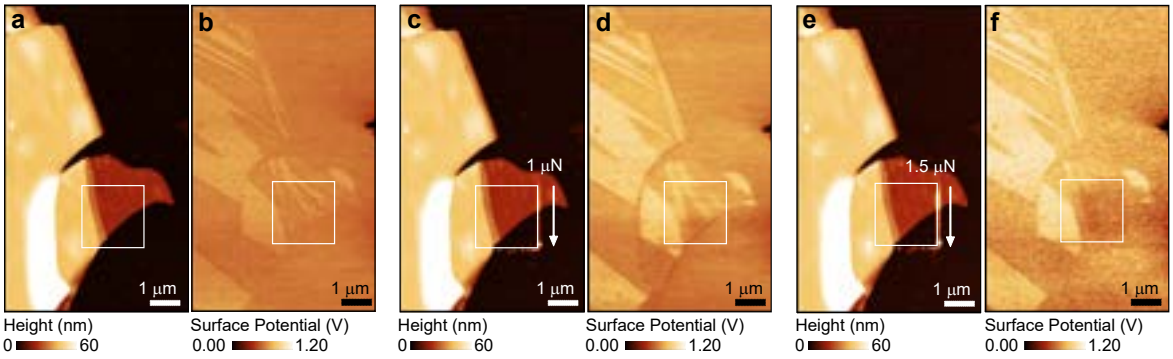

Figure 33 – Mechanical nanomanipulation experiments. (a) Topography and (b) surface potential images of clinochlore at LH before local force application of 1 μN by AFM in contact mode in the region delimited by the white square. KPFM (c) topography and (d) surface potential images of the same area after nanomanipulation. KPFM (e) topography and (f) surface potential images of the same area after a second nanomanipulation with force application of 1.5 μN.

As unique result, we demonstrated a controlled method to modify the electrostatic interaction of the clinochlore surface by mechanical nanomanipulation of its interlamellar water. This procedure allows the multifunctionalization of the clinochlore surface for several applications such as catalysis, sensing, microfluidic devices, and patterning of biomolecules in 2D systems.

5.5 Discussions on the nanoconfinement of water in phyllosilicates

We start by discussing how variations in the atomic structure of barely explored non-swelling phyllosilicate specimens - clinochlore and phlogopite - favors the geo-confinement

of water during the mineral formation. The hydration of micas, such as phlogopite, is better understood in the literature due to studies on swelling specimens of micas [52], in which the hydration occurs through the formation of a hydration shell of water molecules around the interlayer cation. For clinochlore, we observed that the mineral is capable of incorporating more water molecules than phlogopite with the formation of aqueous capillaries in a striated pattern, which may be associated with its more complex structure according to theoretical studies in the literature [37, 165]. However, clinochlore hydration is not a well-established process in the literature. The literature indicates that the mineral may present mesocleavages, exposing sometimes the negatively charged tetrahedral layer, sometimes the positively charged hydroxide layer [6,83]. They make this appointment based on the fact that a height step of about 0.4 nm is observed in the clinochlore topography images, which corresponds to the height of hydroxide layer. With the interpretation that the height step of 0.4 nm is due to the exposure of a mesocleaved hydroxide layer, the literature concludes that it is the mesocleavage difference that generates the surface potential contrast in clinochlore [83], such that distinct water adsorption behaviors on the mineral surface are observed depending on the surface termination [6]. However, the measurements were performed at high humidity environments, in which the same height is expected for an *ice-like* layer of water molecules adsorbed on the surface of phyllosilicates [77]. This makes the correspondence of the surface potential contrast in clinochlore with the occurrence of mesocleavages quite ambiguous. We performed KPFM experiments at low humidity and as a function of relative humidity to elucidate the ambiguity of this interpretation. We showed that the surface potential contrast in clinochlore, in fact, comes mainly from the mineral hydration with the formation of capillaries in a striated pattern, *i.e*, the presence of nanoconfined water in the mineral.

However, what has not yet been pointed out is whether the confinement of water in clinochlore depends on the existence of mesocleavages exposing alternated surfaces with different charges that drive different conformation of water molecules. To clarify this point, it would be necessary to investigate whether mesocleavages actually occurs by performing high-resolution KPFM measurements in a very low humidity environment or even in vacuum. One possibility would be to try to perform quantitative KPFM measurements at this stage. Once this is done, it would also be important to chemically determine which surfaces are exposed when clinochlore is exfoliated. For this, it would be necessary to perform chemical contrast nanoimaging measurements by IR s-SNOM, also in a controlled humidity environment, at frequencies specifically associated only with vibrational modes of the hydroxide layer and only with vibrational modes of the tetrahedral layer in the same sample measured previously by KPFM. Although the origin of aqueous channels in clinochlore is still unclear, as well as whether there is mesocleavage for clinochlore, the formation and stability of aqueous channels is well addressed in this thesis.

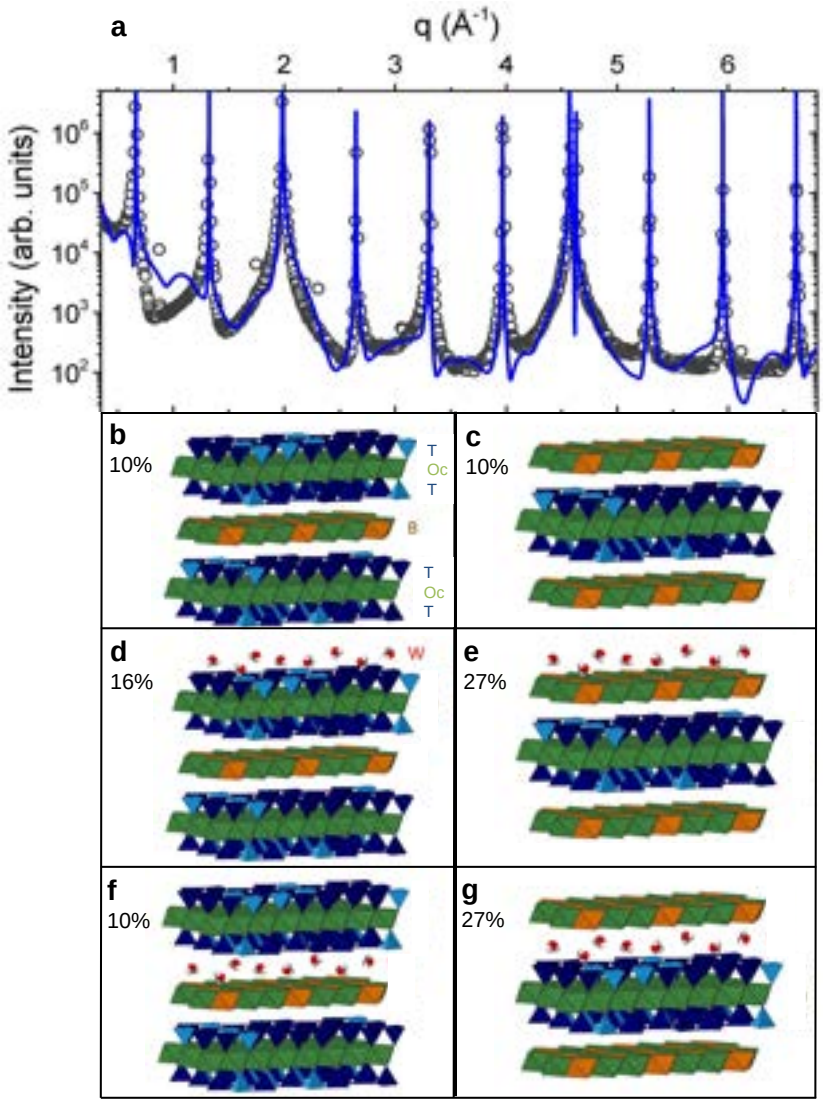

Figure 34 – Crystal truncation rod analysis of clinochlore. (a) X-ray diffractogram of 00l crystal truncation rod (CTR) of clinochlore. The black circles are the experimental data and the blue line represents the total contribution for CTR of each (b)-(g) clinochlore truncations in which the presence of interlamellar water along the stack is mandatory to accurately reproduce the experimental data.

This thesis goes a step further in the attempt to elucidate how clinochlore favors the geo-confinement of water through the formation of aqueous channels and its properties. We propose a simplified capacitive model for the interpretation of KPFM measurements that is in agreement with the IR s-SNOM measurements and captures the main aspects of the physical system. To endorse our model, it is desirable to show structural evidence of the presence of interlamellar water confined between the clinochlore layers. This is currently under investigation. We performed crystal truncation rod (CTR) analysis using X-ray synchrotron radiation to perform 00l diffraction measurements in clinochlore, as shown in Fig. 34. Our preliminary analysis demonstrates that the correct fit of Bragg peak asymmetries due to truncation of the crystal is only accurately reproduced when we consider the presence of water adsorbed at surface and confined in the interlamellar space

of the clinochlore structure along the *c*-axis. Nevertheless, it is important to keep in mind that both KPFM and IR s-SNOM techniques are based on the penetration of electric and optical fields into the material. Therefore, they are also capable of penetrating into our clinochlore sample several nanometers from the surface, beyond its first layer.

The results of this thesis also suggest that an *ice-like* structure may occur for the nanoconfined water in clinochlore. Regarding the stability of the interlamellar water, we observed that it is stable with respect to RH variations, but it can be modified through thermal treatments. Furthermore, we demonstrated that it is possible to rehydrate clinochlore with the reproduction of its aqueous channels after sample dehydration. This indicates that the thermal treatments performed here were not able to close (or create) aqueous channels by thermal expansion or crystalline reorganization. Otherwise, rehydration would not happen following the same capillary pattern. Regarding the adsorption of water on the clinochlore surface, we observed that there are two possible distinct regimes of adsorption on the clinochlore surface with the variation of RH and the time of exposure of the surface to ambient conditions. However, it was not possible to determine which type of adsorption occurs in each regime. As a unique result, this thesis demonstrates a controlled method to modify the electrostatic interaction of the clinochlore surface by mechanical nanomanipulation of its interlamellar water using AFM in contact mode. These nanocapillary studies are of high importance in nanofluidic devices in which water is the media of ionic transport that can be controlled by applying a gate voltage to the capillary walls, taking advantage of the high insulating character of phyllosilicate minerals as confining media [39, 80].

This thesis also leaves interesting open questions to be addressed in the future. To name a few of them, it would be important to perform IR s-SNOM measurements on phlogopite as well. In this way, it would be possible to support a capacitive model capable of correctly describing the diffuse contrast of its surface potential. Furthermore, supporting theoretical investigations are needed to understand the dynamics of dehydration and hydration of phyllosilicate minerals capable of confining layers of water in the interlamellar space. To elucidate the possible formation of ice in the interlamellar space, absorption measurements at the THz frequency could be performed to obtain the low-frequency signature of water molecules that are related to librational modes and hydrogen bonds. Another relevant issue is to investigate whether clinochlore can be rehydrated forming its aqueous channels, but with other functionalized fluids than water. About the nanomanipulation experiments, they could still be carried out with the application of a potential difference between the tip and the sample to perform electrically driven water outflows. It would be interesting to investigate if the mechanical nanomanipulation method can also create aqueous channels. These are some of the possibilities for which this thesis opens doors, from the understanding of the fundamental properties of phyllosilicates and its role on Earth's crust hydration by confining water molecules to several applications in 2D nanotechnologies.

6 Conclusion

This thesis covers the lack of studies on phyllosilicate specimens from the chlorite and triocatahedral mica groups through the characterization of clinochlore and phlogopite from bulk to their few-layer form using several experimental techniques. Notably, this thesis also presents a pioneering investigation on nanoconfined water between the layers of non-swelling phyllosilicates in their few-layer forms using advanced nanoprobe techniques.

As clinochlore and phlogopite are naturally abundant minerals, the presence of impurities is common. In this thesis, the impurities present in these minerals were identified, quantified and analyzed. It was demonstrated that the incorporation of manganese and chromium impurities occurs homogeneously in clinochlore, while iron ions can form inclusions. Although iron is present in clinochlore in both Fe^{2+} and Fe^{3+} oxidation states, the Fe^{2+} content is more than twice the Fe^{3+} content and the inclusions are attributed mostly to Fe^{2+} segregation. For phlogopite, iron is also the main impurity, but there is a balanced proportion of Fe^{2+} and Fe^{3+} ions. This is due to the fact that Fe^{3+} ions can also occupy tetrahedral sites in phlogopite in addition to octahedral ones, which does not occur for clinochlore.

The analyzes showed that iron impurities are mainly responsible for determining the paramagnetic and optical properties of clinochlore and phlogopite. In particular, we noticed a reduction of the effective optical bandgap to 3.6 eV due to the presence of iron impurities, but which did not compromise the insulating character of the samples. It was demonstrated that standard mechanical exfoliation technique can easily obtain few-layer flakes of clinochlore and phlogopite with atomically flat surfaces over large areas (thousands of μm^2). Thus, we show that clinochlore and phlogopite have mandatory topographical and insulating characteristics to be embedded into vdWHs in the fabrication of nanodevices.

Still regarding their few-layer characterization, we discussed the limitations of using EPR and Mössbauer spectroscopy to obtain local information about impurities in FL phyllosilicates as well as micro-FTIR and Raman spectroscopy to assess the vibrational modes of both minerals in their ultrathin limit. As an alternative, this thesis presents XRF and XANES techniques using synchrotron radiation as powerful tools for identifying and mapping impurities in FL phyllosilicates with nanometric resolution. We also demonstrated that sub-diffractional analytical techniques based on near-field interactions, such as SINS, are powerful tools in the vibrational analysis of few-layer phyllosilicates. It is important to emphasize that the study of phyllosilicates using synchrotron radiation presented in this thesis will be useful not only for mineral characterizations, but for any 2D materials.

This thesis presents clinochlore and phlogopite not only as promising low-cost

nanomaterials for applications as insulators in the fabrication of nanodevices, but also as hydrated minerals that can be explored at the frontiers of nanotechnology. In geophysics, hydrated minerals act as natural nanocavities for transporting water on Earth, but the properties of water in nanoconfined environments can be quite exotic and little is known about them. Theoretical studies suggest that the electrostatic charge distribution due to the presence of substitutional ions in the structure of phyllosilicates modulates how water confines between its layers. In this sense, clinochlore can incorporate a higher amount of interlamellar water than phlogopite due to its more complex atomic structure without swelling. In fact, the elementary analysis of this work demonstrated that clinochlore has a higher water-related content than phlogopite. Different hydration patterns were also observed for both minerals. The confinement of water in clinochlore is characterized by the formation of striated aqueous channels, while the hydration of phlogopite has a diffuse pattern. In micas, the hydration occurs by the formation of a cationic shell by water molecules, so the hydration occurs homogeneously. However, the hydration mechanisms in clinochlore are still not well described and the origin of the aqueous channels is not established. The literature associates the origin of the surface potential contrast in clinochlore with mesocleavages, exposing sometimes the negatively charged tetrahedral layer, sometimes the positively charged hydroxide layer of 0.4 nm height which is also expected for an water layer adsorbed on the mineral surface in high humidity environments. This thesis elucidates the ambiguity of this interpretation by showing that the contrast in clinochlore surface potential actually comes mainly from the presence of water in the mineral through measurements carried out in low humidity conditions.

In summary, understanding the hydration of clinochlore with the formation of *ice-like* structures for nanoconfined water will allow us to delineate its capillary and surface properties for future 2D nanotechnology applications exploring sensing, filtering, and patterning of bio-molecules in combination with its insulating capacity. In addition, the results of this work can also give insights for understanding of fundamental geological processes associated with water coming from the Earth's interior, such as plate tectonics that have been operational over 4.4 billion years shaping our planet as matrix of life.

Bibliography

[1] Oliveira, Raphaela de, Alisson R Cadore, Raul O Freitas, and Ingrid D Barcelos: *Review on infrared nanospectroscopy of natural 2D phyllosilicates.* JOSA A, 40:C157, 2023. https://doi.org/10.1364/JOSAA.482518. 11, 27, 46, 65, 70

[2] Vasić, Borislav, Radoš Gajić, Ivana Milošević, Žarko Medić, Marina Blagojev, Marko Opačić, Aleksandar Kremenović, and Dejan Lazić: *Natural two-dimensional pyrophyllite: Nanoscale lubricant, electrical insulator and easily-machinable material.* Applied Surface Science, 608:155114, 2023. https://doi.org/10.1016/j.apsusc.2022.155114. 11, 26, 27

[3] Matković, Aleksandar, Lukas Ludescher, Oleg E Peil, Apoorva Sharma, Kevin P Gradwohl, Markus Kratzer, Maik Zimmermann, Jakob Genser, Daniel Knez, Evelin Fisslthaler, *et al.*: *Iron-rich talc as air-stable platform for magnetic two-dimensional materials.* npj 2D Mater. Appl., 5:94, 2021. https://doi.org/10.1038/s41699-021-00276-3. 12, 28, 30, 31

[4] Mohrmann, Jens, Kenji Watanabe, Takashi Taniguchi, and Romain Danneau: *Persistent hysteresis in graphene-mica van der Waals heterostructures.* Nanotechnology, 26:015202, 2014. https://doi.org/10.1088/0957-4484/26/1/015202. 12, 31

[5] Shim, J., C. H. Lui, T. Y. Ko, Y. Yu, P. Kim, T. F. Heinz, and S. Ryu: *Water-Gated Charge Doping of Graphene Induced by Mica Substrates.* Nano Lett., 12:648–654, 2012. https://doi.org/10.1021/nl2034317. 12, 31, 32

[6] Umeda, Kenichi, Lidija Zivanovic, Kei Kobayashi, Juha Ritala, Hiroaki Kominami, Peter Spijker, Adam S Foster, and Hirofumi Yamada: *Atomic-resolution three-dimensional hydration structures on a heterogeneously charged surface.* Nature Commun., 8:2111, 2017. https://doi.org/10.1038/s41467-017-01896-4. 12, 32, 73, 90

[7] Chen, Xinzhong, Debo Hu, Ryan Mescall, Guanjun You, DN Basov, Qing Dai, and Mengkun Liu: *Modern scattering-type scanning near-field optical microscopy for advanced material research.* Adv. Mater., 31:1804774, 2019. https://doi.org/10.1002/adma.201804774. 13, 47

[8] Ocelic, Nenad, Andreas Huber, and Rainer Hillenbrand: *Pseudoheterodyne detection for background-free near-field spectroscopy.* Appl. Phys. Lett., 89, 2006. https://doi.org/10.1063/1.2348781. 14, 49, 50, 51

[9] Van Vliet, Krystyn J, Ju Li, Ting Zhu, Sidney Yip, and Subra Suresh: *Quantifying the early stages of plasticity through nanoscale experiments and simulations*. Phys. Rev. B, 67:104105, 2003. https://doi.org/10.1021/acsphotonics.9b01533. 14, 50

[10] Fu, Lin, Zhenyu Wang, Om Parkash Dhankher, and Baoshan Xing: *Nanotechnology as a new sustainable approach for controlling crop diseases and increasing agricultural production*. J. Exp. Bot., 71:507–519, 2019. https://doi.org/10.1093/jxb/erz314. 21

[11] Zhao, Huaping and Yong Lei: *3D nanostructures for the next generation of high-performance nanodevices for electrochemical energy conversion and storage*. Adv. Energy Mater., 10:2001460, 2020. https://doi.org/10.1002/aenm.202001460. 21

[12] Sur, Srija, Aishwarya Rathore, Vivek Dave, Kakarla Raghava Reddy, Raghuraj Singh Chouhan, and Veera Sadhu: *Recent developments in functionalized polymer nanoparticles for efficient drug delivery system*. Nano-Struct. Nano-Objects, 20:100397, 2019. https://doi.org/10.1016/j.nanoso.2019.100397. 21

[13] Nandanapalli, Koteeswara Reddy, Devika Mudusu, and Sungwon Lee: *Functionalization of graphene layers and advancements in device applications*. Carbon, 152:954, 2019. https://doi.org/10.1016/j.carbon.2019.06.081. 21

[14] Nejati, Kazem, Mehdi Dadashpour, Tohid Gharibi, Hassan Mellatyar, and Abolfazl Akbarzadeh: *Biomedical applications of functionalized gold nanoparticles: a review*. Journal of Cluster Science, 33:1, 2022. https://doi.org/10.1007/s10876-020-01955-9. 21

[15] Illarionov, Y.Y., T. Knobloch, M. Jech, M. Lanza, D. Akinwande, M.I. Vexler, T. Mueller, M.C. Lemme, G. Fiori, F. Schwierz, and T. Grasser: *Insulators for 2D nanoelectronics: the gap to bridge*. Nat. Commun., 11:3385, 2020. https://doi.org/10.1038/s41467-020-16640-8. 21

[16] Novoselov, K.S., A.K. Geim, S. V. Morozov, D. Jiang, Y. Zhang, S. V. Dubonos, I. V. Grigorieva, and A.A. Firsov: *Electric Field Effect in Atomically Thin Carbon Films*. Science, 80:306, 2004. https://doi.org/10.1126/science.1102896. 21

[17] Cui, Xu, Gwan Hyoung Lee, Young Duck Kim, Ghidewon Arefe, Pinshane Y. Huang, Chul Ho Lee, Daniel A. Chenet, Xian Zhang, Lei Wang, Fan Ye, Filippo Pizzocchero, Bjarke S. Jessen, Kenji Watanabe, Takashi Taniguchi, David A. Muller, Tony Low, Philip Kim, and James Hone: *Multi-terminal transport measurements of MoS2 using a van der Waals heterostructure device platform*. Nat. Nanotechnol., 10:534–540, 2015. https://doi.org/10.1038/nnano.2015.70. 21

[18] Zhang, K., Y. Feng, F. Wang, Z. Yang, and J. Wang: *Two dimensional hexagonal boron nitride (2D-hBN): synthesis, properties and applications.* J. Mater. Chem. C., 5:11992–12022, 2017. https://doi.org/10.1039/C7TC04300G. 21, 54, 56

[19] Wang, Q.H., K. Kalantar-Zadeh, A. Kis, J.N. Coleman, and M.S. Strano: *Electronics and optoelectronics of two-dimensional transition metal dichalcogenides.* Nat. Nanotechnol., 7:699–712, 2012. https://doi.org/10.1038/nnano.2012.193. 21

[20] Wang, Joel I Jan, Yafang Yang, Yu An Chen, Kenji Watanabe, Takashi Taniguchi, Hugh O. H. Churchill, and Pablo Jarillo-Herrero: *Electronic Transport of Encapsulated Graphene and WSe2 Devices Fabricated by Pick-up of Prepatterned hBN.* Nano Lett., 13:1898–1903, 2015. https://doi.org/10.1021/nl504750f. 21

[21] Castellanos-Gomez, Andres: *Why all the fuss about 2D semiconductors?* Nat. Photon., 10:202–204, 2016. https://doi.org/10.1038/nphoton.2016.53. 21

[22] Frisenda, Riccardo, Yue Niu, Patricia Gant, Manuel Muñoz, and Andres Castellanos-Gomez: *Naturally occurring van der Waals materials.* npj 2D Mater. Appl., 4:38, 2020. https://doi.org/10.1038/s41699-020-00172-2. 22, 26, 30, 33, 36, 52, 76

[23] Barcelos, Ingrid D, Raphaela de Oliveira, Gabriel R Schleder, Matheus J S Matos Matos, Raphael Longuinhos, Jenaina Ribeiro-Soares, Ana Paula M Barboza, Mariana C Prado, Elisangela S. Pinto, Yara Galvao Gobato, Helio Chacham, Bernardo R A Neves, and Alisson R Cadore: *Phyllosilicates as earth-abundant layered materials for electronics and optoelectronics: Prospects and challenges in their ultrathin limit.* J. Appl. Phys., 134:000000, 2023. https://doi.org/10.1063/5.0161736. 22

[24] Konta, Jiří: *Phyllosilicates in the sediment-forming processes: weathering, erosion, transportation, and deposition.* Acta Geodyn. et Geomater., 6:13, 2009. 22, 24, 26

[25] Fossum, Jon Otto: *Physical phenomena in clays.* Phys. A: Stat. Mech. Appl., 270:270, 1999. https://doi.org/10.1016/S0378-4371(99)00124-7. 22

[26] Vasić, Borislav, Caterina Czibula, Markus Kratzer, Bernardo RA Neves, Aleksandar Matković, and Christian Teichert: *Two-dimensional talc as a van der Waals material for solid lubrication at the nanoscale.* Nanotechnol., 32:265701, 2021. https://doi.org/10.1088/1361-6528/abeffe. 22, 26

[27] Rehman, Waheed Ur, Amin Ur Rehman, Qazi Muhammad Sharif, and Asma Yamin: *Exfoliation characteristics of Swat vermiculite clay and its application in the preparation of lightweight composite panels.* Constr Build Mater., 366:130200, 2023. https://doi.org/10.1016/j.conbuildmat.2022.130200. 22

[28] Ito, Akihiko and Rota Wagai: *Global distribution of clay-size minerals on land surface for biogeochemical and climatological studies.* Sci. data, 4:1, 2017. https://doi.org/10.1038/sdata.2017.103. 24

[29] Tsuchiya, Jun and Elizabeth C Thompson: *The role of hydrogen bonds in hydrous minerals stable at lower mantle pressure conditions.* Prog. Earth Planet. Sci., 9:63, 2022. https://doi.org/10.1186/s40645-022-00521-3. 24

[30] Cadore, Alisson R, Raphaela de Oliveira, Raphael Longuinhos, Verônica de C Teixeira, Danilo A Nagaoka, Vinicius T Alvarenga, Jenaina Ribeiro-Soares, Kenji Watanabe, Takashi Taniguchi, Roberto M Paniago, *et al.*: *Exploring the structural and optoelectronic properties of natural insulating phlogopite in van der Waals heterostructures.* 2D Mater., 9:035007, 2022. https://doi.org/10.1088/2053-1583/ac6cf4. 24, 28, 29, 52, 64, 66, 68, 70

[31] Castellanos-Gomez, Andres, Magdalena Wojtaszek, Nikolaos Tombros, Nicolás Agraït, Bart J van Wees, and Gabino Rubio-Bollinger: *Atomically thin mica flakes and their application as ultrathin insulating substrates for graphene.* Small, 7:2491–2497, 2011. https://doi.org/10.1002/smll.201100733. 24, 31, 56, 57

[32] Barcelos, Ingrid D, Alisson R Cadore, Ananias B Alencar, Francisco CB Maia, Edrian Mania, Rafael F Oliveira, Carlos CB Bufon, Angelo Malachias, Raul O Freitas, Roberto L Moreira, *et al.*: *Infrared fingerprints of natural 2D talc and plasmon–phonon coupling in graphene–talc heterostructures.* ACS Photonics, 5:1912, 2018. https://doi.org/10.1021/acsphotonics.7b01017. 24, 30, 56, 69

[33] Gadelha, Andreij C, Thiago L Vasconcelos, Luiz G Cançado, and Ado Jorio: *Nano-optical Imaging of In-Plane Homojunctions in Graphene and MoS2 van der Waals Heterostructures on Talc and SiO2.* J. Phys. Chem. Lett., 12:762, 2021. https://10.1021/acs.jpclett.1c01804. 24

[34] Nutting, Darren, Gabriela A Prando, Marion Severijnen, Ingrid D Barcelos, Shi Guo, Peter CM Christianen, Uli Zeitler, Yara Galvão Gobato, and Freddie Withers: *Electrical and optical properties of transition metal dichalcogenides on talc dielectrics.* Nanoscale, 13(37):15853, 2021. https://doi.org/10.1039/D1NR04723J. 24

[35] Oliveira, Raphaela de, Luis AG Guallichico, Eduardo Policarpo, Alisson R Cadore, Raul O Freitas, Francisco MC da Silva, Verônica de C Teixeira, Roberto M Paniago, Helio Chacham, Matheus JS Matos, *et al.*: *High throughput investigation of an emergent and naturally abundant 2D material: Clinochlore.* Appl. Surf. Sci., 599:153959, 2022. https://doi.org/10.1016/j.apsusc.2022.153959. 24, 28, 29, 33, 52, 66, 70, 77

[36] Bleam, W. F. and R. Hoffmann: *Isomorphous Substitution in Phyllosilicates as an Electronegativity Perturbation: Its Effect on Bonding and Charge Distribution.* Inorg. Chem., 27:3180–3186, 1988. https://doi.org/10.1021/ic00291a027. 24, 26, 72, 73

[37] Bleam, W. F.: *The Nature of Cation-Substitutions Sites in Phyllosilicates.* Clays and Clay Miner., 38:527–536, 1990. https://doi.org/10.1346/CCMN.1990.0380510. 24, 26, 28, 72, 73, 80, 81, 90

[38] Khan, Shah H, George Matei, Shivprasad Patil, and Peter M Hoffmann: *Dynamic solidification in nanoconfined water films.* Phys. Rev. Lett., 105(10):106101, 2010. https://doi.org/10.1103/PhysRevLett.105.106101. 24, 78

[39] Radha, B, Ali Esfandiar, FC Wang, AP Rooney, K Gopinadhan, Ashok Keerthi, Artem Mishchenko, Amritha Janardanan, Peter Blake, Laura Fumagalli, *et al.*: *Molecular transport through capillaries made with atomic-scale precision.* Nature, 538:222, 2016. https://doi.org/10.1038/nature19363. 24, 78, 92

[40] Secchi, Eleonora, Sophie Marbach, Antoine Niguès, Derek Stein, Alessandro Siria, and Lydéric Bocquet: *Massive radius-dependent flow slippage in carbon nanotubes.* Nature, 537:210, 2016. https://doi.org/10.1038/nature19315. 24

[41] Neek-Amal, Mehdi, Francois M Peeters, Irina V Grigorieva, and Andre K Geim: *Commensurability effects in viscosity of nanoconfined water.* ACS nano, 10:3685, 2016. https://doi.org/0.1021/acsnano.6b00187. 24, 78

[42] Fumagalli, Laura, Ali Esfandiar, Rene Fabregas, Sheng Hu, Pablo Ares, Amritha Janardanan, Qian Yang, Boya Radha, Takashi Taniguchi, Kenji Watanabe, *et al.*: *Anomalously low dielectric constant of confined water.* Science, 360:1339, 2018. https://doi.org/10.1126/science.aat4191. 24, 76, 83

[43] Shin, Dongha, Jonggeun Hwang, and Wonho Jhe: *Ice-VII-like molecular structure of ambient water nanomeniscus.* Nat. Commun., 10:286, 2019. https://doi.org/10.1038/s41467-019-08292-0. 24, 78, 83

[44] Algara-Siller, G, O Lehtinen, FC Wang, Rahul Raveendran Nair, U Kaiser, HA Wu, Andre K Geim, and Irina V Grigorieva: *Square ice in graphene nanocapillaries.* Nature, 519:443, 2015. https://doi.org/10.1038/nature14295. 24, 83

[45] Kapil, Venkat, Christoph Schran, Andrea Zen, Ji Chen, Chris J Pickard, and Angelos Michaelides: *The first-principles phase diagram of monolayer nanoconfined water.* Nature, 609:512, 2022. https://doi.org/10.1038/s41586-022-05036-x. 24, 83

[46] Ohtani, Eiji: *Hydration and dehydration in Earth's interior.* Annu. Rev. Earth Planet. Sci., 49:253, 2021. https://doi.org/10.1146/annurev-earth-080320-062509. 24

[47] Panero, Wendy R and Razvan Caracas: *Stability and solid solutions of hydrous alumino-silicates in the Earth's mantle.* Minerals, 10:330, 2020. https://doi.org/10.3390/min10040330. 24

[48] Cavailhes, Thibault, Roger Soliva, Pierre Labaume, Christopher Wibberley, Jean Pierre Sizun, Claude Gout, Delphine Charpentier, Alain Chauvet, Bruno Scalabrino, and Martine Buatier: *Phyllosilicates formation in faults rocks: Implications for dormant fault-sealing potential and fault strength in the upper crust.* Geophys. Res. Lett., 40:4272, 2013. https://doi.org/10.1002/grl.50829. 24

[49] Wang, Gaofeng, Lingyu Ran, Jie Xu, Yuanyuan Wang, Lingya Ma, Runliang Zhu, Jingming Wei, Hongping He, Yunfei Xi, and Jianxi Zhu: *Technical development of characterization methods provides insights into clay mineral-water interactions: a comprehensive review.* Appl. Clay Sci., 206:106088, 2021. https://doi.org/10.1016/j.clay.2021.106088. 24, 76

[50] Ehlmann, Bethany L, John F Mustard, Scott L Murchie, Jean Pierre Bibring, Alain Meunier, Abigail A Fraeman, and Yves Langevin: *Subsurface water and clay mineral formation during the early history of Mars.* Nature, 479:53, 2011. https://doi.org/10.1038/nature10582. 24

[51] Chen, Meng, Huijun Zhou, Runliang Zhu, Xiancai Lu, and Hongping He: *Closest-packing water monolayer stably intercalated in phyllosilicate minerals under high pressure.* Langmuir, 36:618, 2019. https://doi.org/10.1021/acs.langmuir.9b03394. 24, 78, 79

[52] Løvoll, G, B Sandnes, Y Méheust, KJ Måløy, JO Fossum, GJ Da Silva, MSP Mundim, R Droppa Jr, and D Miranda Fonseca: *Dynamics of water intercalation fronts in a nano-layered synthetic silicate: A synchrotron X-ray scattering study.* Physica B Condens., 370:90, 2005. https://doi.org/10.1016/j.physb.2005.09.026. 24, 28, 57, 90

[53] Alencar, A. B., A. P. M. Barboza, B. S. Archanjo, H. Chacham, and B. R. A. Neves: *Experimental and theoretical investigations of monolayer and few-layer talc.* 2D Mater., 2:15004, 2015. https://doi.org/10.1088/2053-1583/2/1/015004. 26, 30, 76

[54] Jia, Feifei and Shaoxian Song: *Preparation of monolayer muscovite through exfoliation of natural muscovite.* RSC Adv., 5:52882, 2015. https://doi.org/10.1039/c5ra07749d. 26

[55] Wang, Alian, John J. Freeman, and Bradley L. Jolliff: *Understanding the Raman spectral features of phyllosilicates.* J. Raman Spectrosc., 46:829–845, 2015. https://doi.org/10.1002/jrs.4680. 26, 28, 66

[56] Howie, RA, Jack Zussman, and W Deer: *An introduction to the rock-forming minerals*. Longman London, UK, 1992. https://doi.org/10.1180/DHZ. 26, 34

[57] Santos, Joyce CC, Ana Paula M Barboza, Matheus JS Matos, Ingrid D Barcelos, Thales FD Fernandes, Edmar Avellar Soares, Roberto L Moreira, and Bernardo RA Neves: *Exfoliation and characterization of a two-dimensional serpentine-based material*. Nanotechnol., 30:445705, 2019. https://doi.org/10.1088/1361-6528/ab3732. 26

[58] Li, Xiaoguang, Qinfu Liu, Hongfei Cheng, Shuai Zhang, and Ray L Frost: *Mechanism of kaolinite sheets curling via the intercalation and delamination process*. J. Colloid Interface Sci., 444:74, 2015. https://doi.org/10.1016/j.jcis.2014.12.039. 26

[59] Ndlovu, Bulelwa, Saeed Farrokhpay, and Dee Bradshaw: *The effect of phyllosilicate minerals on mineral processing industry*. Int. J. Miner. Process., 125:149, 2013. https://doi.org/10.1016/j.minpro.2013.09.011. 28

[60] Pollak, H and JG Stevens: *Phyllosilicates: a Mössbauer evaluation*. Hyperfine Interact., 29:1153, 1986. https://doi.org/10.1007/BF02399439. 28

[61] Mosser, C, S Petit, and Michèle Mestdagh: *ESR and IR evidence for chromium in kaolinites*. Clay Miner., 28:353, 1993. https://doi.org/10.1180/claymin.1993.028.3.02. 28, 58

[62] Khan, Muhammad Zubair, Oleg E. Peil, Apoorva Sharma, Oleksandr Selyshchev, Sergio Valencia, Florian Kronast, Maik Zimmermann, Muhammad Awais Aslam, Johann G. Raith, Christian Teichert, Dietrich R. T. Zahn, Georgeta Salvan, and Aleksandar Matković: *Probing Magnetic Ordering in Air Stable Iron-Rich Van der Waals Minerals*. Adv. Phys. Res., page 2300070, 2023. https://doi.org/10.1002/apxr.202300070. 28, 30

[63] Longuinhos, Raphael, Alisson R Cadore, Hans A Bechtel, Christiano JS De Matos, Raul O Freitas, Jenaina Ribeiro-Soares, and Ingrid D Barcelos: *Raman and far-infrared synchrotron nanospectroscopy of layered crystalline talc: vibrational properties, interlayer coupling, and symmetry crossover*. J. Phys. Chem. C ., 127:5876, 2023. https://doi.org/10.1021/acs.jpcc.3c00017. 28, 69

[64] Rancourt, DG, MZ Dang, and Andre E Lalonde: *Mössbauer spectroscopy of tetrahedral Fe3+ in trioctahedral micas*. Am. Min., 77:34, 1992. 28, 35, 36, 63

[65] Bensimon, Y, B Deroide, F Dijoux, and M Martineau: *Nature and thermal stability of paramagnetic defects in natural clay: a study by electron spin resonance*. J. Phys. Chem. Solids, 61:1623, 2000. https://doi.org/10.1016/S0022-3697(00)00048-2. 28, 29, 58

[66] Rager, H and H Schneider: *EPR study of Fe (super 3+) centers in cristobalite and tridymite.* Am. Min., 71:105, 1986. 28, 29, 58

[67] Halenius, U., H. Annersten, and K. Langer: *Spectroscopic studies on natural chloritoids.* Phys. Chem. Minerals, 7:117–123, 1981. https://doi.org/10.1007/BF00308227. 30, 34

[68] Grave, E. De, R. Vanleerberghe, L. Verdonck, and G. De Geyter: *Mössbauer and infrared spectroscopic studies of Belgian chloritoids.* Phys Chem Minerals, 11:85–94, 1984. https://doi.org/10.1007/BF00308010. 30, 34

[69] Borradaile, Graham J and Tomasz Werner: *Magnetic anisotropy of some phyllosilicates.* Tectonophysics, 235:223, 1994. https://doi.org/10.1016/0040-1951(94)90196-1. 30

[70] T. Smith, J. L. Rosenholtz andD.: *The dielectric constant of mineral powders.* Am. Mineral. J. Earth Planet. Mater., 21:115–120, 1936. 30

[71] Mania, E, A B Alencar, A R Cadore, B R Carvalho, K Watanabe, T Taniguchi, B R A Neves, H Chacham, and L C Campos: *Spontaneous doping on high quality talc-graphene-hBN van der Waals heterostructures.* 2D Mater., 4:031008, 2017. https://doi.org/10.1088/2053-1583/aa76f4. 30, 56

[72] Dols-Perez, A., X. Sisquella, L. Fumagalli, and G. Gomila: *Optical visualization of ultrathin mica flakes on semitransparent gold substrates.* Nanoscale Res. Lett., 8:305, 2013. http://dx.doi.org/10.1186/1556-276X-8-305. 31

[73] Castellanos-Gomez, A., M. Poot, A. Amor-Amorós, G. A. Steele, H. S. J. van der Zant, N. Agraït, and G. Rubio-Bollinger: *Mechanical properties of freely suspended atomically thin dielectric layers of mica.* Nano Res., 5:550–557, 2012. https://doi.org/10.1007/s12274-012-0240-3. 31

[74] He, K. T., J. D. Wood, G. P. Doidge, E. Pop, and J. W. Lyding: *Scanning Tunneling Microscopy Study and Nanomanipulation of Graphene-Coated Water on Mica.* Nano Lett., 12:2665–2672, 2012. https://doi.org/10.1021/nl202613t. 31

[75] Xu, K., P. Cao, and J. R. Heath: *Graphene visualizes the first water adlayers on mica at ambient conditions.* Science, 329:1188–1191, 2010. https://doi.org/10.1126/science.1192907. 31

[76] Yalcin, Sibel Ebru, Benjamin A Legg, Merve Yeşilbaş, Nikhil S Malvankar, and Jean François Boily: *Direct observation of anisotropic growth of water films on minerals driven by defects and surface tension.* Sci. Adv., 6:eaaz9708, 2020. https://doi.org/10.1126/sciadv.aaz9708. 32, 73

[77] Hong, Yue, Deliang Zhang, Zhiliang Gao, Yuge Zhang, Qiang Li, and Mingdong Dong: *Constructing two-dimensional interfacial ice-like water at room temperature for nanotribology.* Nano Res., 2023. https://doi.org/10.1007/s12274-023-5485-5. 32, 73, 78, 82, 90

[78] Franceschi, Giada, Pavel Kocán, Andrea Conti, Sebastian Brandstetter, Jan Balajka, Igor Sokolović, Markus Valtiner, Florian Mittendorfer, Michael Schmid, Martin Setvín, *et al.*: *Resolving the intrinsic short-range ordering of K+ ions on cleaved muscovite mica.* Nature Commun., 14:208, 2023. https://doi.org/10.1038/s41467-023-35872-y. 32, 72

[79] Zou, Yi Chao, Lucas Mogg, Nick Clark, Cihan Bacaksiz, Slavisa Milovanovic, Vishnu Sreepal, Guang Ping Hao, Yi Chi Wang, David G Hopkinson, Roman Gorbachev, *et al.*: *Ion exchange in atomically thin clays and micas.* Nature materials, 20:1677, 2021. 32, 72

[80] Mogg, Lucas, G P Hao, S Zhang, Cihan Bacaksiz, Y C Zou, SJ Haigh, FM Peeters, AK Geim, and M Lozada-Hidalgo: *Atomically thin micas as proton-conducting membranes.* Nature Nanotechnol., 14:962, 2019. https://doi.org/10.1038/s41565-019-0536-5. 32, 72, 92

[81] Ulian, G., D. Moro, and G. Valdrè: *First principle investigation of the mechanical properties of natural layered nanocomposite: Clinochlore as a model system for heterodesmic structures.* Compos. Struct., 202:551–558, 2018. https://doi.org/10.1016/j.compstruct.2018.02.089. 33, 34

[82] Moro, D., G. Ulian, and G. Valdrè: *Nanoscale cross-correlated AFM, Kelvin probe, elastic modulus and quantum mechanics investigation of clay mineral surfaces: The case of chlorite.* Appl. Clay Sci., 131:175–18, 2016. https://doi.org/10.1016/j.clay.2015.11.023. 34

[83] Moro, D., G. Ulian, and G. Valdrè: *3D meso-nanostructures in cleaved and nanolithographed Mg-Al-hydroxysilicate (clinochlore): Topology, crystal-chemistry, and surface properties.* Appl. Clay Sci., 169:74–80, 2019. https://doi.org/10.1016/j.clay.2018.12.020. 34, 73, 90

[84] Valdrè, G.: *Natural nanoscale surface potential of clinochlore and its ability to align nucleotides and drive DNA conformational change.* Eur. J. Mineral., 19:309–319, 2007. https://doi.org/10.1127/0935-1221/2007/0019-1732. 34

[85] Quaranta, E., E. Mesto, M. Lacalamita, C. Malitesta, E. Mazzotta, E. Scelsi, and E. Schingaro: *Using a natural chlorite as catalyst in chemical recycling of waste plastics: Hydrolytic depolymerization of poly-[bisphenol A carbonate] promoted by clinochlore.*

Waste Manag., 120:642–649, 2021. https://doi.org/10.1016/j.wasman.2020.10.031. 34

[86] Mehdikhani, A., M. Gholinejad, A. Zamani, and J. M. Sansano: *Application of imidazole modified clinochlore for adsorption of ibuprofen residues from polluted water: preparation, characterization, kinetic and thermodynamic studies.* J. Iran. Chem. Soc., 19:109–120, 2021. https://doi.org/10.1007/s13738-021-02292-y. 34

[87] Hazen, R. M. and C. W. Burnham: *The Crystal Structures of One-Layer Phlogopite and Annite.* Am. Min., 58:889–900, 1973. 34

[88] Kaur, S., S. Singh, L. Singh, and S. P. Lochab: *Effect of gamma irradiation on opto-structural, dielectric, and thermoluminescence properties of natural phlogopite mica.* J. Appl. Phys., 114:093503, 2013. https://doi.org/10.1063/1.4819904. 34

[89] Yoder, H.S. and H.P. Eugster: *Phlogopite synthesis and stability range.* Geochimica et Cosmochimica Acta, 6:157–185, 1954. https://doi.org/10.1016/0016-7037(54)90049-6. 34

[90] Kuwahara, Y.: *Comparison of the surface structure of the tetrahedral sheets of muscovite and phlogopite by AFM.* Phys. Chem. Miner., 28:1–8, 2001. https://doi.org/10.1007/s002690000126. 35

[91] Timón, V., C. S. Praveen, E. Escamilla-Roa, and M. Valant: *Hybrid density functional based study on the band structure of trioctahedral mica and its dependence on the variation of Fe2+ content.* J. Mol. Graph. Model., 44:2013, 129-135. https://doi.org/10.1016/j.jmgm.2013.05.005. 35, 62, 64, 70

[92] Kemp, R C: *Orthorhombic iron centres in muscovite and phlogopite micas.* J. Phys. C: Solid State Phys., 5:792, 1972. https://doi.org/10.1088/0022-3719/5/7/511. 35, 62

[93] Brand, R.: *Normos Mossbauer fitting program Userś Guide.* Wissel, 1995. 38

[94] Wang, Xipeng, Simón Ramírez-Hinestrosa, Jure Dobnikar, and Daan Frenkel: *The Lennard-Jones potential: when (not) to use it.* Phys. Chem. Chem. Phys., 22:10624, 2020. https://doi.org/10.1039/C9CP05445F. 40

[95] Ziegler, Dominik: *Techniques to quantify local electric potentials and eliminate electrostatic artifacts in atomic force microscopy.* PhD thesis, ETH Zurich, 2009. https://doi.org/10.3929/ethz-a-005836152. 41, 42, 43, 44, 45, 73

[96] Nonnenmacher, Manuel, MP o'Boyle, and H Kumar Wickramasinghe: *Kelvin probe force microscopy.* Appl. Phys. Lett., 58:2921, 1991. https://doi.org/10.1063/1.105227. 42

[97] Sadeghi, Ali, Alexis Baratoff, S Alireza Ghasemi, Stefan Goedecker, Thilo Glatzel, Shigeki Kawai, and Ernst Meyer: *Multiscale approach for simulations of Kelvin probe force microscopy with atomic resolution.* Phys. Rev. B, 86:075407, 2012. https://doi.org/10.1103/PhysRevB.86.075407. 43, 73, 74, 75

[98] Cadena, Maria J, Ronald G Reifenberger, and Arvind Raman: *High resolution subsurface imaging using resonance-enhanced detection in 2nd-harmonic KPFM.* Nanotechnology, 29:405702, 2018. https://doi.org/10.1088/1361-6528/aacfdc. 43

[99] Garrett, Joseph L and Jeremy N Munday: *Fast, high-resolution surface potential measurements in air with heterodyne Kelvin probe force microscopy.* Nanotechnology, 27:245705, 2016. https://doi.org/10.1088/0957-4484/27/24/245705. 45

[100] Centrone, Andrea: *Infrared imaging and spectroscopy beyond the diffraction limit.* Annu. Rev. Anal. Chem., 8:101, 2015. https://doi.org/10.1146/annurev-anchem-071114-040435. 46, 47, 49

[101] Huth, Florian: *Nano-FTIR-Nanoscale Infrared Near-Field Spectroscopy.* PhD thesis, University of the Basque Country, 2015. 47, 48, 49, 50, 51

[102] Della Ventura, G, F Bellatreccia, A Marcelli, M Cestelli Guidi, M Piccinini, A Cavallo, and M Piochi: *Application of micro-FTIR imaging in the Earth sciences.* Anal. Bioanal. Chem., 397:2039, 2010. https://doi.org/10.3390%2Fijms161226227. 48, 66

[103] Nieuwoudt, Michél K, Mark P Simpson, Mark Tobin, and Ljiljana Puskar: *Synchrotron FTIR microscopy of synthetic and natural CO2–H2O fluid inclusions.* Vib. Spectrosc., 75:136, 2014. https://doi.org/10.1016/j.vibspec.2014.08.003. 48, 67

[104] Lee, Hyeongwoo, Dong Yun Lee, Min Gu Kang, Yeonjeong Koo, Taehyun Kim, and Kyoung Duck Park: *Tip-enhanced photoluminescence nano-spectroscopy and nano-imaging.* Nanophotonics, 9:3089, 2020. https://doi.org/10.1515/nanoph-2020-0079. 49

[105] Ocelic, Nenad: *Quantitative near-field phonon-polariton spectroscopy.* PhD thesis, Technische Universität München, 2007. 49, 51

[106] Vicentini, Edoardo, Wiwat Nuansing, Iris Niehues, Iban Amenabar, Alexander M Bittner, Rainer Hillenbrand, and Martin Schnell: *Pseudoheterodyne interferometry for multicolor near-field imaging.* Opt. Express, 31:22308, 2023. https://doi.org/10.1364/OE.492213. 51

[107] Lutterotti, L., D. Chateigner, S. Ferrari, and J. Ricote: *Texture, residual stress and structural analysis of thin films using a combined X-ray analysis.* Thin Solid Films, 450:34–41, 2004. https://doi.org/10.1016/j.tsf.2003.10.150. 52, 55

[108] T.L. Phillips, J.K. Loveless, S.W. Bailey: *Cr3+ coordination in chlorites: a structural study of ten chromian chlorites.* Am. Mineral., 65:112–122, 1980. 52, 53

[109] Calle, C. De La, H. Pezerat, and M. Gasperin: *PROBLÈMES D'ORDRE-DÉSORDRE DANS LES VERMICULITES STRUCTURE DU MINÉRAL CALCIQUE HYDRATÉ A 2 COUCHES.* Le J. Phys. Colloq., 38:C7–128–C7–133, 1977. https://doi.org/10.1051/jphyscol:1977725. 52, 53

[110] Gopal, N. O., K. V. Narasimhulu, and J. Lakshmana Rao: *Optical absorption, EPR, infrared and Raman spectral studies of clinochlore mineral.* J. Phys. Chem. Solids., 65:1887–1893, 2004. https://doi.org/10.1016/j.jpcs.2004.07.003. 53, 58, 60, 65, 68

[111] Puebla, Sergio, Hai Li, Hua Zhang, and Andres Castellanos-Gomez: *Apparent colors of 2D materials.* Adv. Photonics Res., 3:2100221, 2022. https://doi.org/10.1002/adpr.202100221. 54

[112] Sousa, Samuel M, Helane LO Morais, Joyce CC Santos, Ana Paula M Barboza, Bernardo RA Neves, Elisângela S Pinto, and Mariana C Prado: *Liquid phase exfoliation of talc: effect of the medium on flake size and shape.* Beilstein J. Nanotechnol., 14:68, 2023. https://doi.org/10.3762/bjnano.14.8. 54

[113] Santos, Joyce CC, Mariana C Prado, Helane LO Morais, Samuel M Sousa, Elisangela Silva-Pinto, Luiz G Cançado, and Bernardo RA Neves: *Topological vectors as a fingerprinting system for 2D-material flake distributions.* npj 2D Mater. Appl., 5:51, 2021. https://doi.org/10.1038/s41699-021-00234-z. 54

[114] Nečas, David and Petr Klapetek: *Gwyddion: an open-source software for SPM data analysis.* Cent. Eur. J. Phys., 10:181, 2012. https://doi.org/10.2478/s11534-011-0096-2. 55, 56

[115] Low, Chong Guan, Qing Zhang, Yufeng Hao, and Rodney S Ruoff: *Graphene field effect transistors with mica as gate dielectric layers.* Small, 10:4213, 2014. 55

[116] Zou, Xiao, Jingping Xu, Lu Liu, Hongjiu Wang, and Wing Man Tang: *Long-term stability of multilayer MoS2 transistors with mica gate dielectric.* Nanotechnology, 31:185202, 2020. https://doi.org/10.1088/1361-6528/ab6ab2. 55

[117] Wang, Lei, I Meric, PY Huang, Q Gao, Y Gao, H Tran, T Taniguchi, Kenji Watanabe, LM Campos, DA Muller, *et al.*: *One-dimensional electrical contact to a two-dimensional material.* Science, 342:614, 2013. https://doi.org/10.1126/science.1244358. 55

[118] Hendricks, Sterling B and Merrill E Jefferson: *Polymorphism of the micas with optical measurements.* Am. Min., 24:729, 1939. 55

[119] Brigatti, Maria Franca and Paolo Davoli: *Crystal-structure refinements of 1M plutonic biotites.* Am. Min., 75:305, 1990. 55

[120] Silva, A. de A. S. da, J. A. Sampaio, A. B. da Luz, S. C. A. França, and C. M. Ronconi: *Modeling Controlled Potassium Release from Phlogopite in Solution: Exploring the Viability of using Crushed Phlogopitite Rock as an Alternative Potassium Source in Brazilian Soil.* J. Braz. Chem. Soc., 24:1366–72, 2013. https://doi.org/10.5935/0103-5053.20130173. 55

[121] Clemens, J D, S Circone, A Navrotsky, P F McMillan, B K Smith, and V J Wall: *Phlogopite: High temperature solution calorimetry, thermodynamic properties, Al-Si and stacking disorder, and phase equilibria.* Geochim. Cosmochim. Acta, 51:2569–78, 1987. https://doi.org/10.1016/0016-7037(87)90307-3. 55, 65, 68

[122] Brigatti, Maria Franca, Luca Medici, Emilio Saccani, and Carmela Vaccaro: *Crystal chemistry and petrologic significance of Fe (super 3+)-rich phlogopite from the Tapira carbonatite complex, Brazil.* Am. Min., 81:913, 1996. https://doi.org/10.2138/am-1996-7-814. 55

[123] Islam, Mohammad Razzakul and Masahiko Tomitori: *Evaluation of the discrete thickness of exfoliated artificially synthesized mica nanosheets on silicon substrates: Toward characterization of the tunneling current through the nanosheets.* Appl. Surf. Sci., 532:147388, 2020. http://dx.doi.org/10.1016/j.apsusc.2020.147388. 57

[124] Abragam, A. and B. Bleaney: *Electron Paramagnetic Resonance of Transition Ions.* Clarendon Press, Oxford, 1970. 58, 59

[125] Hall, P. L.: *The application of electron spin resonance spectroscopy to studies of clay minerals: I. Isomorphous substitutions and external surface properties.* Clay Miner., 15:321–335, 1980. https://doi.org/10.1180/claymin.1980.015.4.01. 58

[126] Schosseler, P.M.: *Transition Metals in Llano Vermiculite Samples: an EPR Study.* Clays Clay Miner., 44:470–478, 1996. https://doi.org/10.1346/CCMN.1996.0440404. 58

[127] Kubelka, P. and F. Munk: *An article on optics of paint layers.* Zeitschrift Für Phys., 12:259–274., 1931. 60, 64

[128] Makula, P., M. Pacia, and W. Macyk: *How To Correctly Determine the Band Gap Energy of Modified Semiconductor Photocatalysts Based on UV–Vis Spectra.* J. Phys. Chem. Lett., 9:6814–6817, 2018. https://doi.org/10.1021/acs.jpclett.8b02892. 60, 64

[129] Olivier, D., J. C. Vedrine, and H. Pézerat: *Application de la résonance paramagnétique électronique à la localisation du Fe3+ dans les smectites.* Bull. du Groupe français des argiles, 27:153–65, 1975. https://doi.org/10.3406/argil.1975.1243. 62

[130] Kemp, R. C.: *Orthorhombic iron centres in muscovite and phlogopite micas.* J. Phys. C Solid State Phys., 4:L11–3, 1971. http://dx.doi.org/10.1088/0022-3719/4/1/020. 62

[131] Hogarth, D. D., F. F. Brown, and A. M. Pritchard: *Biabsorption, Mossbauer spectra, and chemical investigation of five phlogopite samples from quebec.* Canad. Mineral., 10:710–722, 1970. 63

[132] Dyar, M. D. and R. G. Burns: *Mössbauer spectral study of ferruginous one-layer trioctahedral micas.* Am. Min., 71:955–965, 1986. 63

[133] Dyar, M. D.: *Optical and Mossbauer Spectroscopy of Iron in Micas.* Rev. Mineral. Geochemistry, 46:313–49, 2002. https://doi.org/10.2138/rmg.2002.46.06. 64

[134] Faye, G. H.: *The optical absorption spectra of iron in six-coordinate sites in chlorite, biotite, phlogopite and vivianite; some aspects of pleochroism in the sheet silicates.* Can. Mineral., 9:403–25, 1968. 64

[135] Procópio, A. M. S., E. J. C. Ferreira, L. G. Oliveira, M. de Barros, M. R. de Freitas, M. C. da Silva, and F. Moura Filho: *Characterization of phlogopite for processing porous ceramic filters using the replica method.* Cerâmica, 66:433–9, 2020. https://doi.org/10.1590/0366-69132020663803007. 64

[136] Davidson, A. T. and A. F. Vickers: *The optical properties of mica in the vacuum ultraviolet.* J. Phys. C: Solid State Phys., 5:879–87, 1972. https://doi.org/10.1088/0022-3719/5/8/014. 64

[137] Yang, M., M. Ye, H. Han, G. Ren, L. Han, and Z. Zhang: *Near-Infrared Spectroscopic Study of Chlorite Minerals.* J. Spectrosc., 2018:1–11, 2018. https://doi.org/10.1155/2018/6958260. 65, 68

[138] Jenkins, D. M.: *Empirical study of the infrared lattice vibrations (1100-350 cm-1) of phlogopite.* Phys. Chem. Miner., 16:408–14, 1989. https://doi.org/10.1007/BF00199563. 65, 68

[139] Sontevska, V., G. Jovanovski, and P. Makreski: *Minerals from Macedonia. Part XIX. Vibrational spectroscopy as identificational tool for some sheet silicate minerals.* J. Mol. Struct., 834–836:318–327, 2007. https://doi.org/10.1016/j.molstruc.2006.10.026. 65, 68

[140] McKeown, David A, Michael I Bell, and Edgar S Etz: *Raman spectra and vibrational analysis of the trioctahedral mica phlogopite.* Am. Min., 84:970, 1999. https://doi.org/10.2138/am-1999-5-634. 65, 66, 68

[141] Vlasovo, Y. V. and Y. I. Dolomanova: *IR spectra and chemical crystallography of minerals of the phlogopitebiotite group.* Int. Geol. Rev., 24:227–32, 1982. https://doi.org/10.1080/00206818209452396. 65, 68, 69

[142] Ulian, Gianfranco, Daniele Moro, and Giovanni Valdrè: *Infrared and Raman spectroscopic features of clinochlore Mg6Si4O10 (OH) 8: A density functional theory contribution.* Appl. Clay Sci., 197:105779, 2020. http://dx.doi.org/10.1016/j.clay.2020.105779. 65, 66

[143] Freitas, Raul O, Christoph Deneke, Francisco CB Maia, Helton G Medeiros, Thierry Moreno, Paul Dumas, Yves Petroff, and Harry Westfahl: *Low-aberration beamline optics for synchrotron infrared nanospectroscopy.* Opt. Express, 26:11238, 2018. https://doi.org/10.1364/OE.26.011238. 67

[144] Lu, Yi Hsien, Jonathan M Larson, Artem Baskin, Xiao Zhao, Paul D Ashby, David Prendergast, Hans A Bechtel, Robert Kostecki, and Miquel Salmeron: *Infrared nanospectroscopy at the graphene–electrolyte interface.* Nano Lett., 19:5388, 2019. https://doi.org/10.1021/acs.nanolett.9b01897. 67

[145] Bechtel, Hans A, Samuel C Johnson, Omar Khatib, Eric A Muller, and Markus B Raschke: *Synchrotron infrared nano-spectroscopy and-imaging.* Surf. Sci. Rep., 75:100493, 2020. https://doi.org/10.1016/j.surfrep.2020.100493. 67

[146] Hermann, Peter, Arne Hoehl, Georg Ulrich, Claudia Fleischmann, Antje Hermelink, Bernd Kästner, Piotr Patoka, Andrea Hornemann, Burkhard Beckhoff, Eckart Rühl,

et al.: *Characterization of semiconductor materials using synchrotron radiation-based near-field infrared microscopy and nano-FTIR spectroscopy.* Opt. express, 22(15):17948, 2014. https://doi.org/10.1364/OE.22.017948. 67

[147] Ross, GJ: *Experimental alteration of chlorites into vermiculites by chemical oxidation.* Nature, 255:133, 1975. https://doi.org/10.1038/255133a0. 69

[148] Ferrage, Eric: *Investigation of the interlayer organization of water and ions in smectite from the combined use of diffraction experiments and molecular simulations. A review of methodology, applications, and perspectives.* Clays Clay Miner., 64:348, 2016. https://doi.org/10.1346/CCMN.2016.0640401. 72, 80

[149] Odelius, M, MARCO Bernasconi, and M Parrinello: *Two dimensional ice adsorbed on mica surface.* Phys. Rev. Lett., 78:2855, 1997. https://doi.org/10.1103/PhysRevLett.78.2855. 72

[150] Gregory, JK, DC Clary, K Liu, MG Brown, and RJ Saykally: *The water dipole moment in water clusters.* Science, 275:814, 1997. https://doi.org/10.1126/science.275.5301.814. 73

[151] Oliveira, CK, MJS Matos, H Chacham, BRA Neves, *et al.*: *Anomalous response of supported few-layer hexagonal boron nitride to DC electric fields: a confined water effect?* Nanotechnology, 23:175703, 2012. http://dx.doi.org/10.1088/0957-4484/23/17/175703. 73

[152] Li, Guangyong, Bin Mao, Fei Lan, and Liming Liu: *Practical aspects of single-pass scan Kelvin probe force microscopy.* Rev. Sci. Instrum., 83:113701, 2012. https://doi.org/10.1063/1.4761922. 73

[153] Walker, Sarah M, Maria C Marcano, Sooyeon Kim, Sandra D Taylor, and Udo Becker: *Understanding calcite wettability alteration through surface potential measurements and molecular simulations.* J. Phys. Chem. C, 121:28017, 2017. https://doi.org/10.1021/acs.jpcc.7b09565. 73

[154] Valdrè, Giovanni, Daniele Malferrari, and Maria Franca Brigatti: *Crystallographic features and cleavage nanomorphology of chlinochlore: specific applications.* Clays Clay Miner., 57:183, 2009. https://doi.org/10.1346/CCMN.2009.0570205. 73

[155] Grove, TT, MF Masters, and RE Miers: *Determining dielectric constants using a parallel plate capacitor.* Am. J. Phys., 73:52, 2005. https://doi.org/10.1119/1.1794757. 75, 76

[156] Kaur, Sukhnandan, Surinder Singh, and Lakhwant Singh: *Effect of oxygen ion irradiation on dielectric, structural, chemical and thermoluminescence properties of*

natural muscovite mica. Appl. Radiat. Isot., 121:116, 2017. https://doi.org/10.1016/j.apradiso.2016.12.053. 76

[157] Yang, Qian, PZ Sun, Laura Fumagalli, YV Stebunov, SJ Haigh, ZW Zhou, IV Grigorieva, FC Wang, and AK Geim: *Capillary condensation under atomic-scale confinement*. Nature, 588:250, 2020. https://doi.org/10.1038/s41586-020-2978-1. 78

[158] Silvestrelli, Pier Luigi, M Bernasconi, and Michele Parrinello: *Ab initio infrared spectrum of liquid water*. Chem. Phys. Lett., 277:478, 1997. https://doi.org/10.1016/S0009-2614(97)00930-5. 79

[159] Yeşilbaş, Merve: *Thin water and ice films on minerals: a molecular level study*. PhD thesis, Umeå University, 2018. 79

[160] Ockwig, Nathan W, Jeffery A Greathouse, Justin S Durkin, Randall T Cygan, Luke L Daemen, and Tina M Nenoff: *Nanoconfined water in magnesium-rich 2: 1 phyllosilicates*. J. Am. Chem. Soc., 131:8155, 2009. https://doi.org/10.1021/ja900812m. 79

[161] Hu, J, DF Ogletree, M Salmeron, *et al.*: *The structure of molecularly thin films of water on mica in humid environments*. Surf. Sci., 344:221, 1995. https://doi.org/10.1016/0039-6028(95)00858-6. 82

[162] Hu, Jun, X D Xiao, DF Ogletree, and M Salmeron: *Imaging the condensation and evaporation of molecularly thin films of water with nanometer resolution*. Science, 268:267, 1995. https://doi.org/10.1126/science.268.5208.267. 82

[163] Villieras, F, J Yvon, JM Cases, P De Donato, F Lhote, and R Baeza: *Development of microporosity in clinochlore upon heating*. Clays Clay Miner., 42:679, 1994. https://doi.org/10.1346/CCMN.1994.0420604. 83

[164] Gao, Yuan, Mingzhe Li, Haozhe Zhang, Yue Zhang, Weiyi Lu, and Baoxing Xu: *Anomalous solid-like necking of confined water outflow in hydrophobic nanopores*. Matter, 5:266, 2022. https://doi.org/10.1016/j.matt.2021.11.023. 89

[165] Bleam, W. F., G. J. Welhouse, and M. A. Janowiak: *The Surface Coulomb Energy And Proton Coulomb Potentials Of Pyrophyllite 010, 110, 100, and 130 EDGES*. Clays Clay Miner., 41:305–316, 1993. https://doi.org/10.1346/CCMN.1993.0410305. 90

ANNEX A – Published Articles

- *High throughput investigation of an emergent and naturally abundant 2D material: Clinochlore*

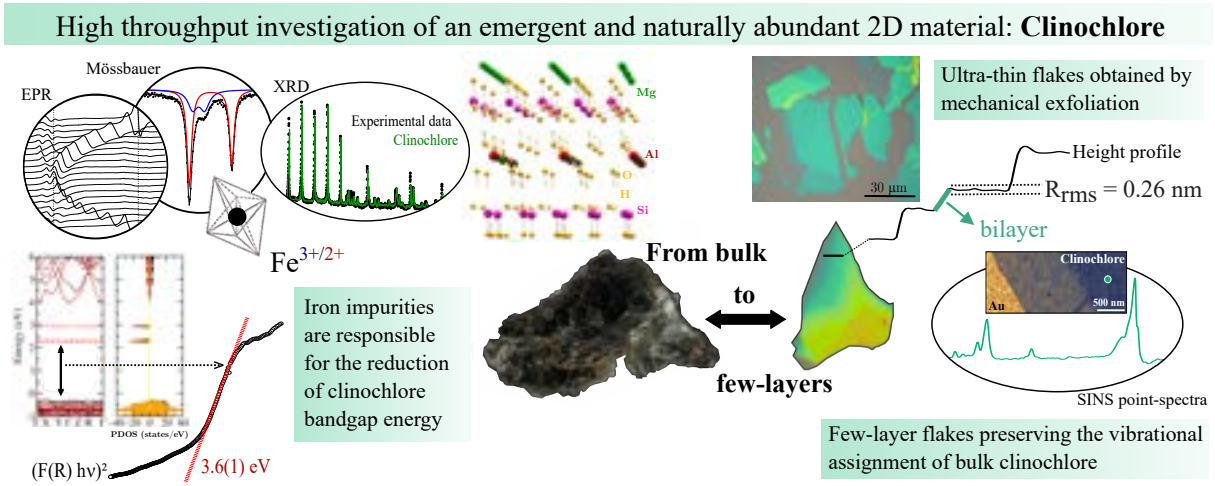

Raphaela de Oliveira, Luis A.G. Guallichico, Eduardo Policarpo, Alisson R. Cadore, Raul O. Freitas, Francisco M.C. da Silva, Verônica de C. Teixeira, Roberto M. Paniago, Helio Chacham, Matheus J.S. Matos, Angelo Malachias, Klaus Krambroc and Ingrid D. Barcelos.

Applied Surface Science **599**, 153959 (2022).

`https://doi.org/10.1016/j.apsusc.2022.153959`

Abstract: Phyllosilicate minerals, which form a class of naturally occurring layered materials (LMs), have been recently considered as a low-cost source of two-dimensional (2D) materials. Clinochlore [Mg5Al(AlSi3)O10(OH)8] is one of the most abundant phyllosilicate minerals in nature, exhibiting the capability to be mechanically exfoliated down to a few layers. An important characteristic of clinochlore is the natural occurrence of defects and impurities which can strongly affect their optoelectronic properties, possibly in technologically interesting ways. In the present work, we carry out a thorough investigation of the clinochlore structure on both bulk and 2D exfoliated forms, discussing its optical features and the influence of the insertion of impurities on its macroscopic properties. Several experimental techniques are employed, followed by theoretical first-principles calculations considering several types of naturally-ocurring transition metal impurities in the mineral lattice and their effect on electronic and optical properties. We demonstrate the existence of requirements concerning surface quality and insulating properties of clinochlore that

are mandatory for its suitable application in nanoelectronic devices. The results presented in this work provide important informations for clinochlore potential applications and establish a basis for further works that intend to optimize its properties to relevant 2D technological applications through defect engineering.

- *Exploring the structural and optoelectronic properties of natural insulating phlogopite in van der Waals heterostructures*

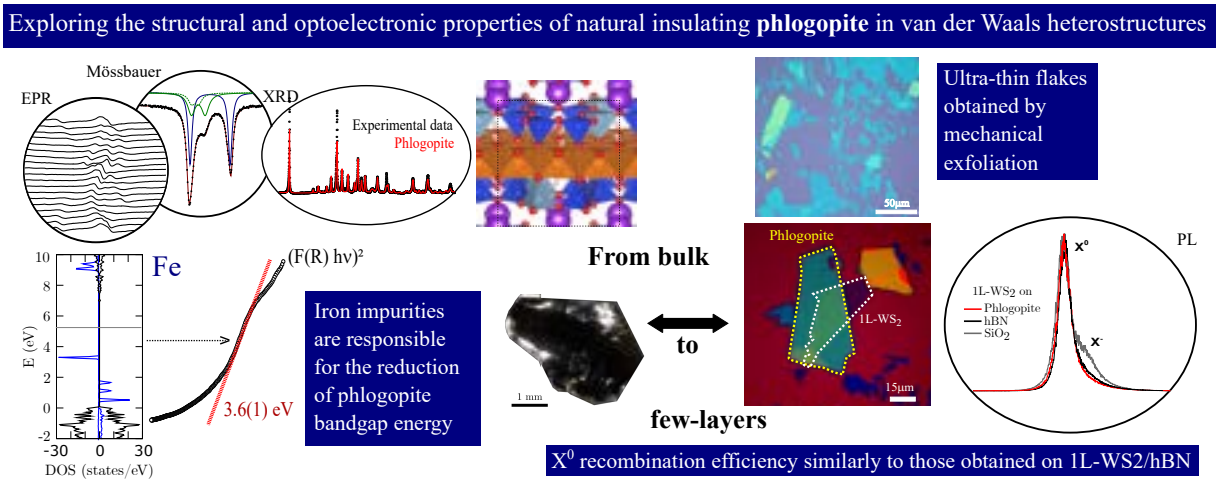

Alisson R Cadore, **Raphaela de Oliveira**, Raphael Longuinhos, Verônica de C Teixeira, Danilo A Nagaoka, Vinicius T Alvarenga, Jenaina Ribeiro-Soares, Kenji Watanabe, Takashi Taniguchi, Roberto M Paniago, Angelo Malachias, Klaus Krambrock, Ingrid D Barcelos and Christiano J S de Matos.

2D Materials **9**, 035007 (2022).

`https://doi.org/10.1088/2053-1583/ac6cf4`

Abstract: Naturally occurring van der Waals crystals have brought unprecedented interest to nanomaterial researchers in recent years. So far, more than 1800 layered materials (LMs) have been identified but only a few insulating and naturally occurring LMs were deeply investigated. Phyllosilicate minerals, which are a class of natural and abundant LMs, have been recently considered as a low-cost source of insulating nanomaterials. Within this family an almost barely explored material emerges: phlogopite (KMg3(AlSi3)O10(OH)2). Here we carry out a high throughput characterization of this LM by employing several experimental techniques, corroborating the major findings with first-principles calculations. We show that monolayers (1L) and few-layers of this material are air and temperature stable, as well as easily obtained by the standard mechanical exfoliation technique, have an atomically flat surface, and lower bandgap than its bulk counterpart, an unusual trend

in LMs. We also systematically study the basic properties of ultrathin phlogopite and demonstrate that natural phlogopite presents iron impurities in its crystal lattice, which decreases its bandgap from about 7 eV to 3.6 eV. Finally, we combine phlogopite crystals with 1L-WS2 in ultrathin van der Waals heterostructures and present a photoluminescence study, revealing a significant enhancement on the 1L-WS2 optical quality (i.e. higher recombination efficiency through neutral excitons) similarly to that obtained on 1L-WS2/hexagonal boron nitride heterostructures. Our proof-of-concept study shows that phlogopite should be regarded as a good and promising candidate for LM-based applications as a low-cost layered nanomaterial.

- *Review on infrared nanospectroscopy of natural 2D phyllosilicates*

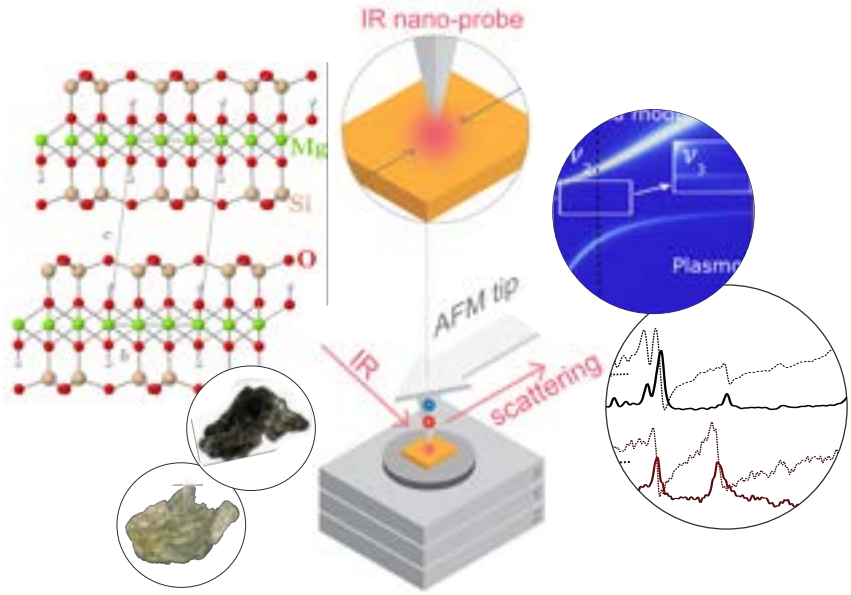

Raphaela de Oliveira, Alisson R. Cadore, Raul O. Freitas and Ingrid D. Barcelos.

Journal of the Optical Society of America **40**, C157-C168 (2023).

https://doi.org/10.1364/JOSAA.482518

Abstract: Phyllosilicates have emerged as a promising class of large bandgap lamellar insulators. Their applications have been explored from the fabrication of graphene-based devices to 2D heterostructures based on transition metal dichalcogenides with enhanced optical and polaritonics properties. In this review, we provide an overview of the use of infrared (IR) scattering-type scanning near-field optical microscopy (s-SNOM) for studying nano-optics and local chemistry of a variety of 2D natural phyllosilicates. Finally, we bring a brief update on applications that combine natural lamellar minerals into multifunctional nanophotonic devices driven by electrical control.

- *Phyllosilicates as earth-abundant layered materials for electronics and optoelectronics: Prospects and challenges in their ultrathin limit*

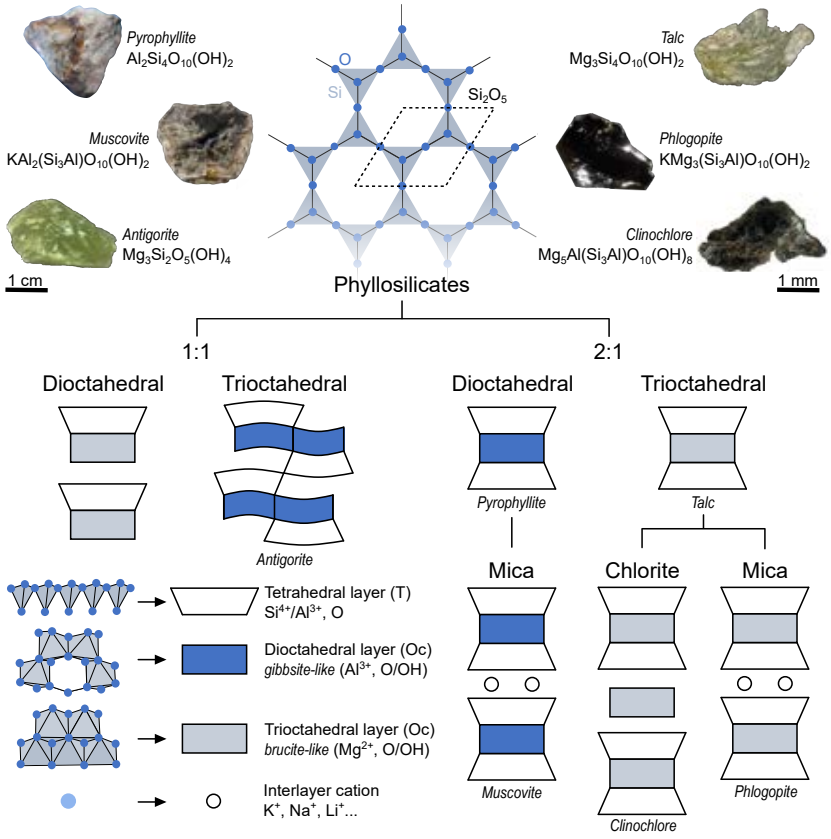

Ingrid D. Barcelos, **Raphaela de Oliveira**, Gabriel R. Schleder, Matheus J. S. Matos, Raphael Longuinhos, Jenaina Ribeiro-Soares, Ana Paula M. Barboza, Mariana C. Prado, Elisângela S. Pinto, Yara Galvão Gobato, Hélio Chacham, Bernardo R. A. Neves and Alisson R. Cadore.

Journal of Applied Physics **134**, 000000 (2023).

`https://doi.org/10.1063/5.0161736`

Abstract: Phyllosilicate minerals are an emerging class of naturally occurring layered insulators with large bandgap energy that have gained attention from the scientific community. This class of lamellar materials has been recently explored at the ultrathin two-dimensional level due to their specific mechanical, electrical, magnetic, and optoelectronic properties, which are crucial for engineering novel devices (including hetero-structures). Due to these properties, phyllosilicate minerals can be considered promising low-cost nanomaterials for future applications. In this Perspective article, we will present relevant features of these materials for their use in potential 2D-based electronic and optoelectronic applications, also discussing some of the major challenges in working with them.